Simulation on Electron Optics and Basic Examinations for the Development of a Solid Xenon Particle Detector

Master Thesis

for the attainment of the academic degree
Master of Science (M. Sc.)

submitted by

Michael Wagenpfeil

22nd September, 2014

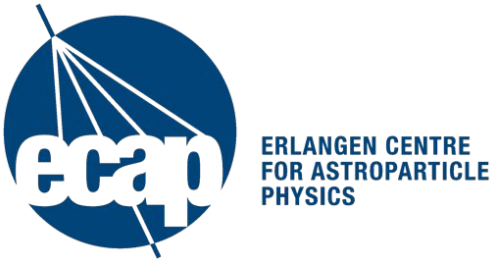

performed at
Erlangen Centre for Astroparticle Physics
Friedrich-Alexander-Universität Erlangen-Nürnberg
under the supervision of M.Sc. Mykhaylo Filipenko and Prof. Dr. Gisela Anton

Contents

1. Introduction

The discovery of the electron in 1895 marked the begin of *modern physics* and in the following decades, new ideas and technical innovations were developed to attack this new research field. Along this progress, the combination of theoretical knowledge and sophisticated technical skills in designing experiments proved to be essential to establish new models of the subatomic world. When the examination of radioactivity initiated the new field of *nuclear physics*, Italian physicist Corbino expressed this point in one famous speech in 1929 in the following way [1]:

> One can therefore conclude that while great progress in experimental physics in its ordinary domain is unlikely, many possibilities are open in attacking the atomic nucleus. [...] To participate in the general movement, [...] it is indispensable for experimentalists to have a sure grasp of the results of theoretical physics, and also to have increasingly large experimental means. Attempting to do experimental physics without working knowledge of the results of theoretical physics and without ample laboratory means is like trying to win a contemporary battle without airplanes and guns.

This quote identifies the two relevant columns necessary for the development of modern physics: A sound theoretical knowledge and efficient laboratory facilities. Both proved to be the foundation of many breakthroughs made after Corbinos speech e.g. the discovery of the neutron, the positron and the pion. In the 1950s, nuclear physics gradually developed to particle physics. This process involved new demanding experimental facilities as accelerators and cyclotrons and the required setups as well as the scientific working groups grew in size and complexity. With the digital revolution, computers appeared in all fields of physics establishing a third column. From then on, simulation methods of physical events provided completely new capacities and caused a significant acceleration of research progress.

Nowadays, the demands on experimental setups are more sophisticated than ever. The Standard Model (SM) of particle physics is the youngest universal physical model and one of the most successful theories in physics. However, the experimental proof for its last piece – the discovery of the Higgs boson – took more than 40 years of effort and required accelerators and detectors of unforeseen complexness. At the same time, the observation of CP-violation processes, dark matter and neutrino oscillation initiated a new field: The *physics beyond the Standard Model*.

To approach this field, new experimental approaches have to be created to cope with the new requirements. Since non-SM processes are supposed to be suppressed strongly, corresponding events are very rare. As a result, the evaluation of non-SM events require long observation times and large efforts have to be made considering the enormous influence of background. A possible way to proof the laws of physics beyond the SM is the neutrinoless double beta decay ($\beta\beta0\nu$-decay) which also is the motivation for the framework of this thesis. The evidence of this hypothetical decay would involve lepton-number violating particle reactions, which is forbidden in the SM [2]. This is why this decay often is referred to as the *Holy Grail* of today's particle physics (see [3], sec. 6.8). The basic theoretical knowledge of the $\beta\beta0\nu$-decay is explained in chapter 2.

There are several theoretical approaches to describe the $\beta\beta0\nu$-decay which are mainly based on different assumptions about non-SM processes. Many experimental groups try to attack this decay as for example Heidelberg-Moscow, GERDA, COBRA, KamLAND-Zen or EXO by exploiting a wide range of experimental designs and different $\beta\beta$-isotopes (see [2], chap. 6). In 2006, the Heidelberg-Moscow experiment claimed to have observed a positive evidence for the $\beta\beta0\nu$-decay in ^{76}Ge [4]. This claim initiated a plethora of sceptical comments and statements regarding the presented claim (e.g. [5]). At present the existence of the $\beta\beta0\nu$-decay is as arguable as before. Only upper limits for the half-life of $\beta\beta0\nu$-isotopes and the effective neutrino mass could be determined so far. For example, the most stringent limit of the $\beta\beta0\nu$ half-life of ^{136}Xe is $T^{0\nu}_{1/2} > 3.4 \times 10^{25}$ yr (90% C.L.) determined by combined data of the KamLAND-Zen and EXO-200 collaborations [6].

In this thesis, a new detector concept for $\beta\beta0\nu$-searches is presented using solid xenon as sensor material and the intrinsic $\beta\beta$-isotope ^{136}Xe as decay nucleus. Secondary electrons from the ongoing interaction are supposed to be extracted from the solid by electric fields and projected onto a pixelated detector. The goal of this concept is to achieve particle tracking of the $\beta\beta0\nu$-track. This might be a promising way to cope with the low event-rate and the large background-rate, which is the major challenge in $\beta\beta0\nu$-searches [7], [8]. The physics of condensed rare gases have been examined thoroughly in the 1980s providing profound data and observations of the properties of rare gas solids (e.g. [9], [10], [11], [12]). Chapter 3 presents an overview of this conceptual framework and the properties of solid xenon regarding its usage as particle detector.

Due to the low $\beta\beta0\nu$-rate, a large mass of the decaying isotope is necessary. Chapter 4 presents simulations of an electron optical system designed to read out a large-scaled rare gas solid with only one pixelated detector. This might be an important step towards future $\beta\beta0\nu$-tracking experiments which is why the main focus of this work is about electron optics. Finally, chapter 5 presents the first experiments of growing rare gas solids in a vacuum chamber.

2. Motivation and Theory

Contents

This chapter presents the basic theoretical background along with the motivation behind the development of solid rare gas detectors for particle physics. Section 2.1 explains the neutrinoless double beta decay as well as the experimental requirements for its examination and the theoretical consequences if its existence is proven. Section 2.2 summarises the detection process of fast incident particles in a sensor material.

2.1. Neutrinoless Double Beta Decays

2.1.1. The Double Beta Decay

The double beta decay (or $\beta\beta$-decay) is a nuclear transition of two protons decaying simultaneously into two neutrons under the emission of two electrons and two electron-antineutrinos. The double beta nucleus with proton number Z decays to a nucleus with $Z + 2$ and the same mass number A. Figure 2.1 illustrates the corresponding Feynman-diagram and equation 2.2 shows the transition reaction.[1]

[1] The reaction is illustrated on the hadronic level. In fact, each beta decay is associated with a subnuclear transition of an up-quark to a down-quark.

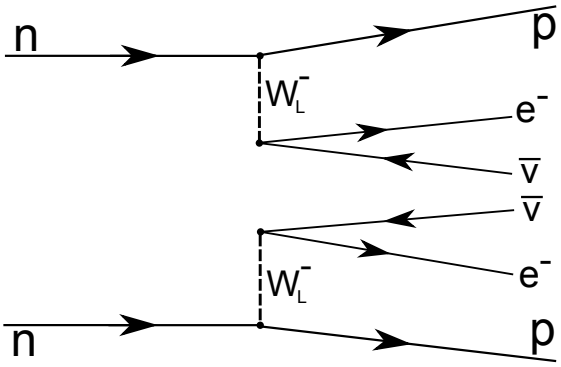

Figure 2.1: A Feynman diagram of the $\beta\beta$-decay at the hadronic level. Two neutrons convert to two protons under the emission of two W^--bosons which decay to two electrons and two anti-neutrinos afterwards. The two neutrons are uncorrelated but decay simultaneously (see [2] p. 17).

$$2\ n \longrightarrow 2\ p + 2\ e^- + 2\ \bar{\nu}_e \quad . \tag{2.1}$$

Today, 35 nuclides are known that undergo $\beta\beta$-decays [2]. In the case of all these isotopes, the ground state of the neighboured isotope with $Z+1$ has a higher energy level whereas the ground state of the isotope with $Z+2$ has a lower energy compared to the primary nucleus (see figure 2.2a). In this case, a single beta decay is energetically forbidden whereas the $\beta\beta$-nucleus may undergo a double beta transition by tunnelling the higher energy state of the neighbour isotope quantum mechanically and decaying directly to the isotope with $Z+2$. Another possibility to regard $\beta\beta$-decays is the Bethe-Weizsäcker mass formula. This formula contains the so-called pairing term, which generate different nuclear masses depending on whether the neutron number N and Z of the nucleus are odd or even. Disregarding mixed nuclei, the formula gives a parabolic correlation between the nuclear mass and Z if A is kept constant as it is the case in all kinds of β-decays. Due to the pairing term $\delta_{A,Z}$ however, two mass parabolas occur, which are shifted in mass with $2 \times \delta_{A,Z}$ as it is shown in figure 2.2b. All $\beta\beta$-isotopes are even/even-nuclei. In a single beta decay, Z is increased by one and N is reduced by one so that the new isotope is an odd/odd-nucleus. In the mass parabola picture, the decay corresponds to a transition from the even/even- to the odd/odd-parabola. If there is an increase in mass, the transition is forbidden. However, if the next even/even-nucleus has a lower mass, this decay is possible although less likely due to the Z-increment of two.

The double beta decay is consistent with the Standard Model. Due to the necessity to tunnel the higher energy state of the neighboured isotopes, this nuclear transition is energetically suppressed and very rare. A theoretical description is delivered by the second-order perturbation theory within the Fermi theory. Hence, the transition rate is proportional to G_F^4 (which is the Fermi constant) and the $\beta\beta$-half-life is very high. Typical half-life values of $\beta\beta$-isotopes are in a range between some 10^{18} up to 10^{24} yr (see [2], tab. II and [3], tab. 6.7). The biggest

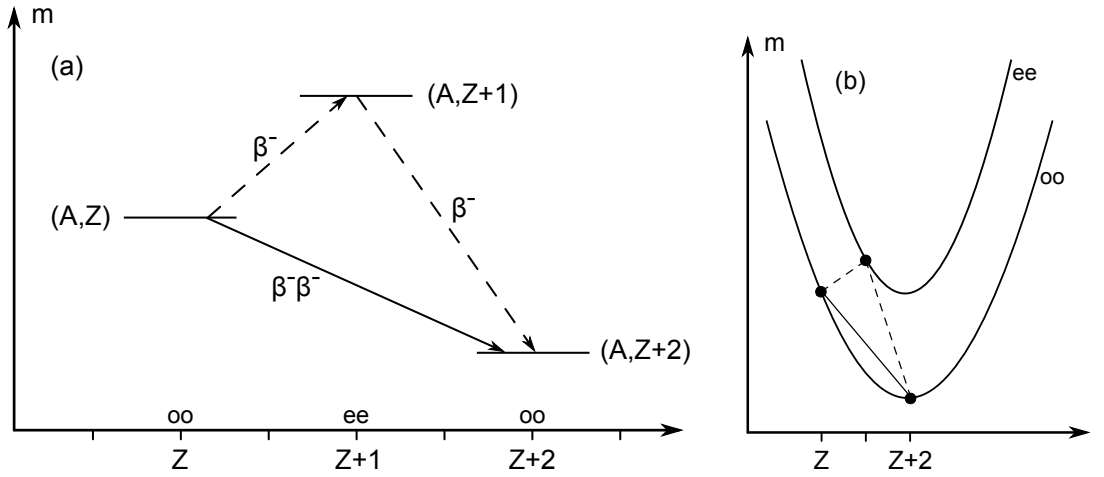

Figure 2.2.: (a) A scheme of the energetic levels in the case of a $\beta\beta$-nucleus with proton and neutron number Z and N and mass number $A = Z + N$. Both Z and N of the $\beta\beta$-nucleus and the final nucleus are even. The ground state of the isotope between lies energetically higher than that of the even/even-nuclei so that a single beta-decay is forbidden (dotted lines). **(b)** Scheme of the Weizsäcker mass parabolas for even/even- and odd/odd- nuclei with constant A. The $\beta\beta$-decay takes a jump of 2 in Z on the same parabola. These figures are redrawn from [3], fig. 6.41.

challenge for the observation of the $\beta\beta$-decay is the enormous contribution of background events. Huge efforts have to be made to pick out the few $\beta\beta$-events out of the sea of similar – mostly single beta – transitions. Additionally, a large mass of the $\beta\beta$-isotope is required to detect enough $\beta\beta0\nu$-events in a given time interval. This is also why it took physicists more than fifty years between the theoretical prediction of the $\beta\beta$-decay in 1935 and its first direct observation in 1987 (cp. [3], p. 302).

Regarding current experiments, the most important $\beta\beta$-isotopes are ^{76}Ge, ^{116}Ca, ^{130}Te and ^{136}Xe. The latter is supposed to be used as decaying material in future within the experimental framework of this work. All in all, there are more than 20 individual experimental projects worldwide working with $\beta\beta$-isotopes [2].

2.1.2. The Neutrinoless Double Beta Decay

The neutrinoless double beta decay or $\beta\beta0\nu$-decay is a modification of the $\beta\beta$-decay explained above. Here, the same transition of a nucleus with Z to a nucleus with $Z + 2$ and constant A takes place as shown in figure 2.1 but no neutrinos are emitted. The corresponding Feynman-diagram is presented in figure 2.3 and the transition reaction can be written as:

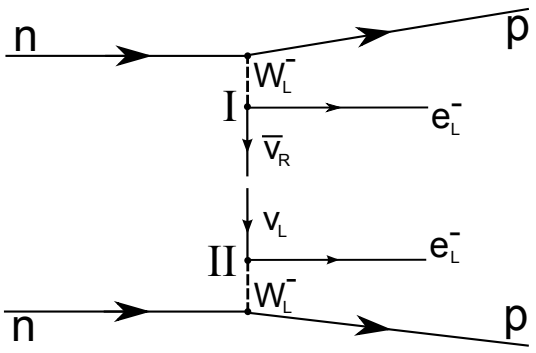

Figure 2.3: A Feynman diagram of the $\beta\beta0\nu$-decay at the hadronic level. Two neutrons again convert to two protons under emission of two W^--bosons. Due to a neutrino-antineutrino-transition, only electrons are emitted. This transition only is possible, if the neutrino is a Majorana particle and there is a conversion of the different neutrino helicities.

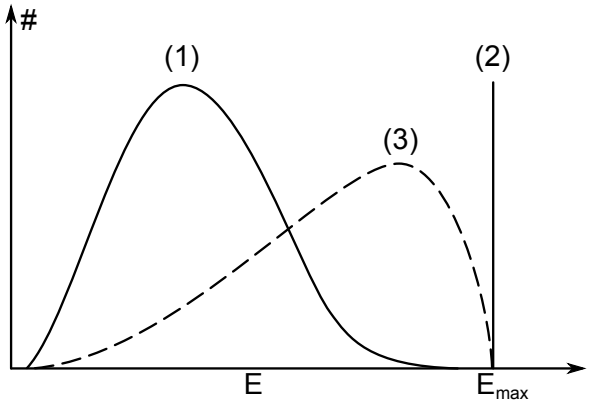

Figure 2.4: Energy distribution of several $\beta\beta$-modes. Spectrum (1) shows a $\beta\beta$-decay energy distribution with four leptons in the final state. Spectrum (2) is the sharp peak in the case of a $\beta\beta0\nu$-decay. Spectrum (3) corresponds to a $\beta\beta0\nu$-decay with addition Majoron in the final state. This figure is redrawn from [3], fig. 6.40.

$$2\ n \longrightarrow 2\ p + 2\ e^- \quad . \tag{2.2}$$

First suggested in 1939, this decay is purely hypothetically and still not confirmed in particle physics experiments [3]. According to theoretical models, the half-life of the neutrinoless $\beta\beta$-modes is even larger than that of the neutrino-accompanied decay [2]. Therefore, the background problem is an even bigger challenge in $\beta\beta0\nu$-studies than it already is in $\beta\beta$-observations. Furthermore, the dominant $\beta\beta2\nu$ transitions are a part of the background signal in $\beta\beta0\nu$-searches. Figure 2.4 shows the continuous distribution of the $\beta\beta$-decay (1) and the one of the neutrinoless mode (3). Here, phase space considerations dictate that the electron energy has to be a sharp value of half the total decay energy $Q = E_{max}$ for each lepton. The nuclear recoil is negligible due to the large difference in mass compared to the electrons. The energetic criteria is the best experimental approach to distinguish both decay modes. However, due to the extremely low half-life of the $\beta\beta0\nu$-decay compared to the $\beta\beta$-mode, the $\beta\beta0\nu$ energy distribution is manifested in a very small peak at $E = Q$ and hard to recognise in the $\beta\beta$-background. This is one of the main challenges in $\beta\beta0\nu$-searches.

The reason for the extremely low $\beta\beta0\nu$-rate is the violation of the Standard Model since the lepton number is not conserved in $\beta\beta0\nu$-transitions ($|\Delta L| = 2$). Furthermore, some kind of neutrino-antineutrino-transition has to exist, so that the two antineutrinos in figure 2.3 are allowed interact directly. This is also forbidden in the SM as explained below. The half-life of $\beta\beta0\nu$-nuclides can be calculated by the following formula [2]:

$$\left(T_{1/2}^{0\nu}\right)^{-1} = G^{0\nu}(Q, Z) \ \left|M^{0\nu}\right|^2 \ m_{\beta\beta}^2 \quad , \tag{2.3}$$

where $G^{0\nu}$ is the phase space factor that depends on Q and Z, $M^{0\nu}$ is the nuclear mixing matrix element, which has to be calculated from a complex theoretical approach, and $m_{\beta\beta}$ is the effective neutrino mass of the neutrino-antineutrino-transition. The half-life is very long due to the SM-violating character of $\beta\beta0\nu$-transitions, which are strongly suppressed by nature.

2.1.3. Consequences for Physics related to the $\beta\beta0\nu$-Decay

In $\beta\beta0\nu$-decays, two neutrons decay to two protons under emission of two W-bosons as interaction particles of the weak force. Figure 2.3 shows that in the $\beta\beta0\nu$-diagram, both weak vertices are connected by a combined neutrino propagator which means that no antineutrinos are emitted. The upper vertex still emits an antineutrino whereas the lower vertex requires a neutrino to conserve the lepton number. This is realised by a inversion of the lower neutrino propagator in the $\beta\beta0\nu$-diagram compared the $\beta\beta$-diagram in figure 2.1. This implies a conversion of the antineutrino into a neutrino, which is not emitted but absorbed at vertex II. [2] Consequently, some kind of $\nu - \bar{\nu}$-transition is required within the neutrino propagator which is only possible, if the particles ν and $\bar{\nu}$ are identical. This first condition for $\nu - \bar{\nu}$-transitions implies that the neutrino is a Majorana particle: $\nu = \bar{\nu} = \nu_M$ and that there are only two chirality states: $\nu_L \equiv \bar{\nu}_L$ and $\nu_R \equiv \bar{\nu}_R$.

The $\nu - \bar{\nu}$-transition requires a second condition which is the conversion of the neutrino helicity. According to the (V-A)-theory, the W-bosons only couple to left-handed particles (and right-handed antiparticles) so that the W-boson is marked as W_L^- in figure 2.3. At vertex I, the antineutrino therefore needs to be right-handed whereas the neutrino at vertex II is left-handed. Consequently, the neutrino helicity state H has to change throughout the $\nu - \bar{\nu}$-transition in the middle. This helicity conversion is illustrated by the L and R subscript of the (anti)neutrinos.

[2] This results from the inherent properties of Feynman diagrams. Each particle that moves in positive time direction is identical to the corresponding antiparticle that moves in negative time direction and the inversion of any propagator switches the particle-antiparticle identity.

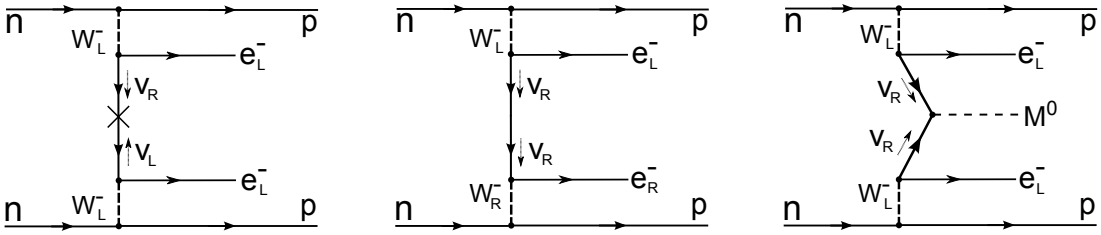

Figure 2.5.: Several ways to accommodate the helicity conversion within the neutrino-antineutrino transition of the $\beta\beta0\nu$-decay. From left to right: The conversion is achieved by the m_ν-mechanism, the existence of right-handed electroweak currents and the emission of a Majoron. (Compare to [3] p. 303)

Both conditions for a $\nu - \bar{\nu}$-transition are forbidden in the Standard Model yet both conditions are necessary to describe $\beta\beta0\nu$-decays. The first condition ($\nu = \bar{\nu} = \nu_M$) looks as if it can be fulfilled easily since the Majorana- or Dirac-nature of the neutrino is not identified yet and there are strong arguments for each position. Actually, it can be derived that the observation of one single $\beta\beta0\nu$-decay necessarily implies Majorana-neutrinos irrespectively of the exact $\beta\beta0\nu$-mechanism (this is called the Schechter-Valle-theorem, see [2], sec. 3.2). This eventually leads to a violation of the lepton number by $|\Delta L| = 2$ and the whole SM-based view on neutrino interactions has to be reconsidered. The second condition is more difficult. Basically, there are three different ways to introduce a helicity conversion in neutrino-antineutrino transitions. They all are presented in the Feynman diagrams of figure 2.5.

The first way to achieve a helicity conversion is the m_ν-mechanism shown in the left diagram. Since the neutrino is a massive particle, it has no definite helicity state but a mixture of $H = +1$ and $H = -1$. In fact, according to [3], the possibility that the helicity of a real particle has the "wrong" value is

$$W = \frac{1}{2}\left(1 - \frac{v}{c}\right) \approx \left(\frac{m_\nu}{2E_\nu}\right)^2 \quad . \tag{2.4}$$

As a result, the upper right-handed neutrino has a small negative helicity component, which is absorbed at the lower vertex since this component is able to couple to the left-handed electroweak current. In this case, the amplitude of such a transition is proportional to the effective neutrino mass $m_{\beta\beta}$ in equation 2.3. In this case, this mass can be called the *effective neutrino Majorana mass*. The second way is shown in the middle diagram. Here, the neutrino helicity is conserved and a right-handed electron is created at vertex II. This requires a right-handed electroweak current (RHC) and also the corresponding W_R-boson. The amplitude of this $\beta\beta0\nu$-mode is proportional to a factor $\eta \ll 1$ which is the coupling constant of this new-

kind right-handed interaction. Typically, a heavy Majorana neutrino N_i steps on the place of the ν_R in the Feynman diagram.[3] A third possibility to introduce a helicity conversion is the emission of a light or massless neutral boson – the so-called Majoron M^0 or $\mathcal{X}^0$. In this case, the number of particles in the final state is changed and the helicity problem vanishes. The corresponding $\beta\beta0\nu$-energy distribution is not sharp but a continuous spectrum as shown in figure 2.4.

In conclusion, there are several ways to explain the helicity conversion. Today's most favoured mode is the m_ν-mechanism since it could employed successfully to describe the phenomena observed in neutrino oscillation experiments. If the $\beta\beta0\nu$-decay is observed, the neutrino definitely has to be a Majorana particle. If not, it gives a limit to the unknown half-life of this nuclear transition. Assuming a correctly determined phase space and matrix mixing element according to equation 2.3, this gives us an upper limit to $m_{\beta\beta}$ and hence to the actual neutrino mass eigenstates. As a summary, the $\beta\beta0\nu$-decay is a decent way to prove physics beyond the Standard Model. This includes the Majorana-nature of the neutrino, the absolute neutrino mass, and consequently the hierarchy of the different neutrino mass-eigenstates.[4]

2.1.4. Consequences for Experimental $\beta\beta0\nu$-Searches

Due to the extremely low decay rate, experimental methods along with $\beta\beta0\nu$-searches have to face several challenges. At first, a large mass of the decay material is required to observe enough $\beta\beta0\nu$-events in a reasonable time interval. Considering an ideal detector with perfect efficiency and no background, the general formula to calculate the amount A of observed decays is according [3]:

$$A = \ln(2)\frac{M}{m_A}\frac{T}{T_{1/2}} \quad , \tag{2.5}$$

where M is the observed mass, m_A is the nuclear mass of the decay material and T is the data-taking time. The EXO-experiment determined the neutrino accompanied half-life of ^{136}Xe to be $(2.11 \pm 0.21) \times 10^{21}\,\mathrm{yr}$ [2]. Based on this half-life, equation 2.5 yields that as little as $1.45 \cdot 10^3$ decays can be expected in 1 kg of ^{136}Xe within one year. In contrast, the $\beta\beta0\nu$ half-life is supposed to be several orders of magnitude larger than the measured $\beta\beta2\nu$ half-life. The most stringent experimental limit is obtained by combined results from the KamLAND-Zen and EXO-200 collaborations. They determined a neutrinoless double beta half-life of $T^{0\nu}_{1/2} > 3.4 \times 10^{25}\,\mathrm{yr}$ at 90 % C.L. (see [6] and additionally [14]). This means that a

[3] This appearance of heavy neutrinos originates from the so-called see-saw-mechanism (see also [2], sec. 2.3.). It provides a way to deal with the relatively small neutrino masses by introducing heavy Majorana neutrinos N_i with a predominantly positive helicity mass state.

[4] Further information and theoretical details can be found in [3] pp. 300-309, [2] pp. 3-23 and [13] pp. 80-84.

much higher mass of the $\beta\beta$-isotope is required to examine actual $\beta\beta0\nu$-events and -rates. Basically, there are two problems involved with high decay material masses. On the one hand, the setup gets very large and complex and much effort has to be made to create a proper experimental design. For example, vacuum systems as well as cooling systems and electronic readout devices have to be scaled up with increasing mass. On the other hand, the total mass of the $\beta\beta0\nu$-isotope has to be enriched in the natural isotopic ratio. By doing so, the influence of different decay channels of other isotopes is reduced. However, enrichment processes are quite expensive so that the natural abundance is among the arguments considered in the choice of the particular $\beta\beta$-isotopes used in a certain $\beta\beta0\nu$-experiment. The abundance of ^{136}Xe is 8.9 %. Furthermore, xenon can be enriched to high purities very easily since it is gaseous.

The second challenge is the reduction of the massive amount of background in the sensitive volume regarding the large acquisition time needed to cope with the low $\beta\beta0\nu$-rate. At the one hand, there is intrinsic background due to the $\beta\beta2\nu$-channel of every nuclide that is capable of $\beta\beta0\nu$-decays. This part of the background can only be distinguished from $\beta\beta0\nu$-events measuring the energy of the electrons (the neutrinos leave the detector without interaction). A very good energy resolution is necessary to prevent that the $\beta\beta0\nu$-spectrum is overwhelmed by the $\beta\beta2\nu$-tail near the Q-value of the decay (see spectrum (1) and (2) in figure 2.4). To achieve the best energy resolution possible, current experiments use all kind of modern detector technology like semicondcutor detectors (GERDA, COBRA), cryogenic detectors (CUORE) or noble gas detectors (NEXT, EXO, KAMLAND) [2]. On the other hand, there is the natural radioactivity of the detector components. For example, ^{208}Tl and ^{214}Bi have a high Q-value and their decay products may lead to false positive events (i.e. events that deposit the same energy in the sensor as the Q-value of a $\beta\beta0\nu$-decay but are not $\beta\beta0\nu$-event) ([2] p. 39). Furthermore, several Rn-isotopes within natural decay chains are able to diffuse easily through many materials and to pollute a given sensor material with undesired decaying isotopes. Beyond that, there is background from cosmic rays and natural radioactivity of the surrounding materials. To reduce these effects, external shielding and internal active veto systems can be applied as well as a radiopure fabrication of the required experimental components.

A novel way to cope with the background problem is to measure additional signatures of a given event. A possibility to do so is to measure multiple signals as the scintillation and secondary electron signal (as in the case of EXO; see [2], sec. 6.3). Another possibility is to achieve particle identification of the observed events by applying some kind of particle tracing in the detector system. For example, it is possible to drift secondary electrons, which are generated along an incident particle track, in a pixel detector sensor without loosing the spatial

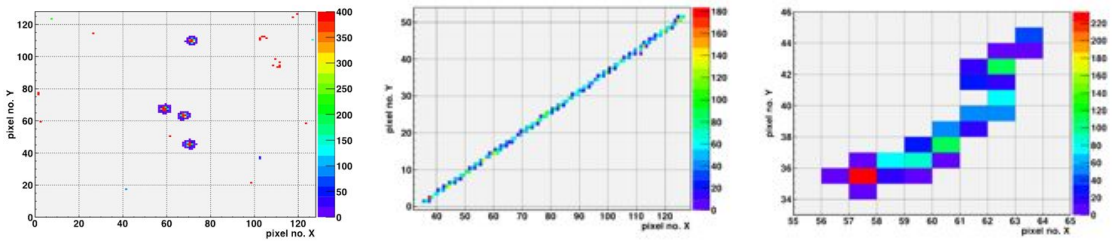

Figure 2.6.: These projected tracks of different incident particles are obtained with a pixelated semiconductor detector (see section 3.3). The axes correspond to the x- and y-pixel number of the pixel matrix and the colour scale shows the energy in keV. The big blobs on the left picture are heavy ionising α-particles. The plot in the centre shows the straight track of a minimal ionising muon. The right picture presents an electron track, which can be recognised by its jagged trajectory ending up in a Bragg-peak.

information of the projected track [15]. By doing so, the additional information of a 2D projection of the track obtained with a pixelated detector together with the energy deposition per pixel can be used for particle identification. For example, α-particles are heavily ionising particles and manifest in a strong ionising track in the detector whereas cosmic muons are minimal ionising particles which can be recognised by their straight and long lines.[5] These tracks can be seen at the left (α-track) and in the middle (muon track) of figure 2.6. In contrast, electrons with typical energies of radioactive decays (on the keV/MeV scale) are often scattered and travel on curvy trajectories through the sensor. Additionally, the stopping power for charged particles in a certain material increases with decreasing kinetic energy so that the electron deposits more and more energy the longer it moves in the sensor material. As a consequence, each electron track gradually turns to a high energetic head at one end of the jagged tail as it can be seen at the right in figure 2.6.[6]

In the case of the $\beta\beta0\nu$-decay, two Bragg-peaks are expected – one for each electron and therefore at each end of the overall track as shown in figure 2.7.[7] This interaction signature can be used as starting point to suppress parts of the

[5]The term *minimal ionising* refers to a minimum in the stopping power of charged particle in matter at $E \approx 3M_p$. In the case of atmospheric muons produced by $\pi^{\pm}$-decays in the atmosphere, all muons arriving at the sea level fall in that energy range.

[6]This high energy deposition at the end of the a charged particle track is referred to as *Bragg-peak*. The reason for the significant rise of the stopping power lies in the increase of $-dE/dx$ in the Bethe-Bloch formula with decreasing energy below $E_{mip} = 3m$.

[7]Such signatures do not occur necessarily. It is possible that one electron carries only a small part of the decay energy whereas the other electron carries the entire rest. In this case, one might not see two Bragg-peaks.

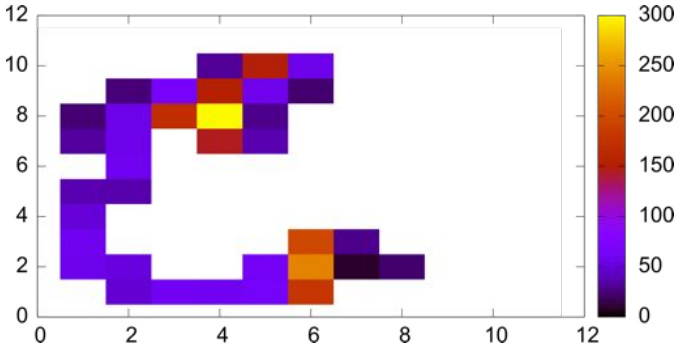

Figure 2.7: This picture shows, how a $\beta\beta0\nu$-event would look like on the pixel matrix of a Timepix detector. The track is based on a simulation of a $\beta\beta0\nu$-decay of ^{116}Cd within a cadmium-telluride sensor layer. Again, the axes correspond to the pixel number and the colour scale to the energy per pixel in keV.

single electron background left after the α- and muon-separation. Considering the stopping power in solid xenon and the kinetic energy of $\beta\beta0\nu$-electrons according to the $\beta\beta$-Q-values of ^{136}Xe of about $2-3\,\mathrm{MeV}$, the length of the whole path length until $\beta\beta0\nu$-electron are stopped completely is about $6\,\mathrm{mm}$.[8] Due to the curvy electron tracks with their strong bends and edges, the actual track is somewhat smaller. According to previous experiments with CdTe-sensor Timepix detectors, the expected length of the whole $\beta\beta0\nu$-track is about $2\,\mathrm{mm}$. In conclusion, particle tracking might support the background suppression in $\beta\beta0\nu$-experiments, if a projection of the initial particle track onto some kind of detection chip can be realised.

Each individual $\beta\beta0\nu$-study presents different sensor concepts, detector designs and background suppression methods. A possibility to compare the single experiments and their efficiency is provided by the sensitivity to the neutrinoless double-beta half-life or – more physical – to the effective neutrino mass. The sensitivity refers to a limit in $m_{\beta\beta}$ based on the mass M of the decay material and the data-taking time t. It can be derived by [7]:

$$m_{\beta\beta} = K\sqrt{1/\epsilon}\left(\frac{c\,\Delta E}{M\,t}\right)^{1/4} \quad , \tag{2.6}$$

where K is a constant depending on the isotope, ϵ is the signal detection efficiency, ΔE is the energy resolution and c is the background rate (in counts per keV, kg and year). This formula means that if the actual $m_{\beta\beta}$ is higher than the calculated value, it should be possible to detect $\beta\beta0\nu$-events based on a given M within the time t. In contrast, if no events are discovered, this allows to set an upper limit to $m_{\beta\beta}$. The $T^{0\nu}_{1/2}$-limit of the combined KamLAND-Zen and EXO data mentioned above corresponds to a Majorana neutrino mass limit of $m_{\beta\beta} < (120-250)\,\mathrm{meV}$ [6].

[8] This over all path length is often referred to as the *complete slowing down approximation*.

2.2. Detection Process in Sensor Materials

Detecting particles basically means to detect the secondary radiation emitted by the products or by-products of the interaction with the sensor material. The actual particle cannot be observed directly. Detector physics is mainly about optimising the sensor material for the specific particle or interaction that is about to be examined.

This section takes a closer look on the physic behind the interaction of incident particles with a given particle detector sensor. Since the $\beta\beta0\nu$-decay is in the focus in this work, the section only deals with the interaction of charged particles e.g. electrons.

2.2.1. Interaction of Charged Particles with Matter

At this point, a fast, incident, charged particle is considered generated in a radioactive decay or a cosmic ray interaction. The particle hits a particle detector or – more precisely – the sensor material of the detector. This sensor material is also referred to as interaction material. It is the active part of the detector and therefore sensitive for the interaction of the given particle. Possible sensor materials are for example rare gases or specifically designed depleted semiconductor layers.[9]

While propagating through the sensor material, charged particles pass the electric field of all nuclei and electrons of the atoms close to the particle trajectory. The particles interact with the atomic fields by multiple scattering processes. As a result, a certain part of the particle energy is absorbed by the atoms along the trajectory within the sensor material. This energy deposition is described by the *Bethe-Bloch-formula*, which can be written as the following [16]:

$$-\left\langle \frac{\mathrm{d}E}{\mathrm{d}x} \right\rangle = Kz^2 \frac{Z}{A} \frac{1}{\beta^2} \left(\frac{1}{2} \ln \frac{2m_\mathrm{e}c^2\beta^2\gamma^2 T_\mathrm{max}}{I^2} - \beta^2 + \cdots \right) \quad . \tag{2.7}$$

In this formula, $\mathrm{d}E/\mathrm{d}x$ describes the energy deposition per track length in $\mathrm{eVg^{-1}cm^2}$. This dimension is also referred to as the *stopping power* of a certain material. The stopping power depends on the charge z of the incident particle and its velocity (β and γ) as well as the proton and mass number Z and A of the sensor material. K is a factor that only depends on natural constants.[10] T_max describes the maximal energy that can be transferred to a single electron of the sensor material in one

[9] E.g. in the case of the Timepix detector explained in section 3.3.

[10] K can be calculated by $4\pi N_\mathrm{A} r_\mathrm{e}^2 m_\mathrm{e} c^2$ and its value is about $0.307075\,\mathrm{MeVcm^2}$.

Quantity	Value	Source
silicon	3.61 eV	[16], tab. 2.2
germanium	2.96 eV	[16], tab. 2.2
CdTe	4.43 eV	[16], tab. 2.2
liquid krypton	20.5 ± 1.5 eV	[17], tab. 4
liquid xenon	15.6 ± 0.3 eV	[18], tab. I; [19], tab. I
solid xenon	12.4 ± 0.3 eV	[20], tab. 2.4

Table 2.1.: Overview of several experimental values for the average energy W for the generation of one e/H-pair in different sensor materials.

scattering process. It depends on both energy and mass of the interacting particle. I refers to the material-dependant mean excitation energy.[11]

The deposited energy is absorbed by the sensor material atoms along the trajectory. The spatial distribution of the absorbed energy therefore can be used to reconstruct the pathway of the incident particle

2.2.2. Creation of Electron/Hole-Pairs

Any electron or light ion penetrating an insulator loses energy mainly by electronic excitations and by generation of electron-hole pairs along its pathway [12]. As a result, a track of so-called secondary electrons and positive, excited ions is generated. The track carries the information of the spatial orientation of the incident particle trajectory but also the energy deposition distribution along its pathway. The number of produced of electron/hole-pairs (and hence secondary electrons) therefore is very important – especially in particle tracking experiments intending to reconstruct the initial particle track.

This number $N_{\mathrm{e/h}}$ is proportional to the deposited energy E_Σ of a given interaction and can be calculated by $N_{\mathrm{e/h}} = E_\Sigma / W$. W is the average energy of one e/H-pair compared to all possible excitation processes caused by the entire absorbed energy. It is characteristic of the given material and can be calculated according to [11] by:

$$W = E_i + f\, E_x + \bar{\epsilon} \quad , \tag{2.8}$$

where E_i is the characteristic average ionisation energy, E_x is the energy required to create an exciton, f is the number of excitation created for each e/H-pair and $\bar{\epsilon}$ is the average initial kinetic energy carried away by the charge carriers and

[11] I can be roughly estimated by $16\, Z^{0.9}$ eV for small Z and $10\, Z^1$ eV for $Z > 20$. This estimation gives 172 eV for silicon (measured: 137 eV), 216 eV for argon (measured: 191 eV), 500 eV for cadmium-telluride and 540 eV for xenon.

eventually goes into heat (see also [20], sec. 2.2). Some measurements of W for several semiconductors and condensed rare gases are given in table 2.1.

Additionally, scintillation light occurs along the trajectory due to the relaxation of excited sensor material atoms. The scintillation light propagates through the sensor and is partially absorbed. The remaining light can be detected at the side of the sensor as well, e.g. by PMTs or avalanche photo detectors. As a consequence, two different general signatures of the ongoing particle interaction can be evaluated.

3. Experimental Basics and Properties of Solid Xenon as Detector Material

Contents

This chapter presents the basic ideas behind the experimental setup covered in this work. Chapter 2 already explained the theoretical background and demands of $\beta\beta0\nu$-searches. At this point, section 3.1 gives an introduction to the experimental basics of rare gas solids (RGS) and their possible application as sensor material whereas chapter 5 will present the conceptual design of this experiment up to now. Section 3.2 deals with the properties of condensed xenon considering its suitability as sensor material in particle detectors. Section 3.3 focuses on the Timepix detector and its application in imaging experiments.

3.1. Experimental Background

3.1.1. Inspirations for Tracking Experiments in Solid Xenon

In section 2.1, it is explained that the biggest problem of $\beta\beta0\nu$-searches is the very long half-life of the corresponding $\beta\beta$-isotopes. As a result, background rejection is the main challenge in designing $\beta\beta0\nu$-experiment. One way to deal with that problem is to measure more than one signature of the ongoing decay or interaction. For example, many modern particle detectors record both the secondary electrons as well as the scintillation signal (see also section 2.2). Especially in the case of recent low-background experiments, the setup designs are specified to combine the measurement of both signals e.g. to achieve a better energy resolution of the ongoing interactions in the detector.

One way to gather more information of the observed $\beta\beta$-decay is to look at the shape of the track of the decay products i.e. the primary electrons in this case. As shown in figure 2.6, tracking examinations can be used to separate a wide range of detected events depending on the initial particle. Tracking is therefore a promising way to reduce the large amount of background in $\beta\beta0\nu$-experiments [15], [8]. This technique is supposed to be applicable for a much larger detector volume than that of the Timepix sensor layer as well.

3.1.2. Principal Setup Design

The setup design requires three basic elements: The sensitive volume of the sensor material, a homogeneous electric field and the detector including the electronic readout devices. Figure 3.1a shows a scheme of this basic design.

The sensor material is the active volume, where the interaction takes place. It is shown in turquoise in figure 3.1. In the experimental concept of this work, the far-end design includes a solid xenon sensor enriched with the $\beta\beta$-isotope ^{136}Xe. Any incident particle as α-particles from radioactive impurities, atmospheric muons or intrinsic $\beta\beta x\nu$-electrons generate electron/hole-pairs in the sensor as explained in section 2.2.

The secondary electrons are drifted to the surface of the RGS due to an electric field applied over the sensitive volume. The secondary electron trajectories are illustrated in blue in figure 3.1. Afterwards, they are extracted into the medium above the sensitive volume. Three electrodes are used to generate two different field strengths for both the sensitive volume as well as the medium above. A homogeneous electric field is assumed so that the secondary electrons present no horizontal velocity component. The drifting and emission process is explained in detail in section3.2.

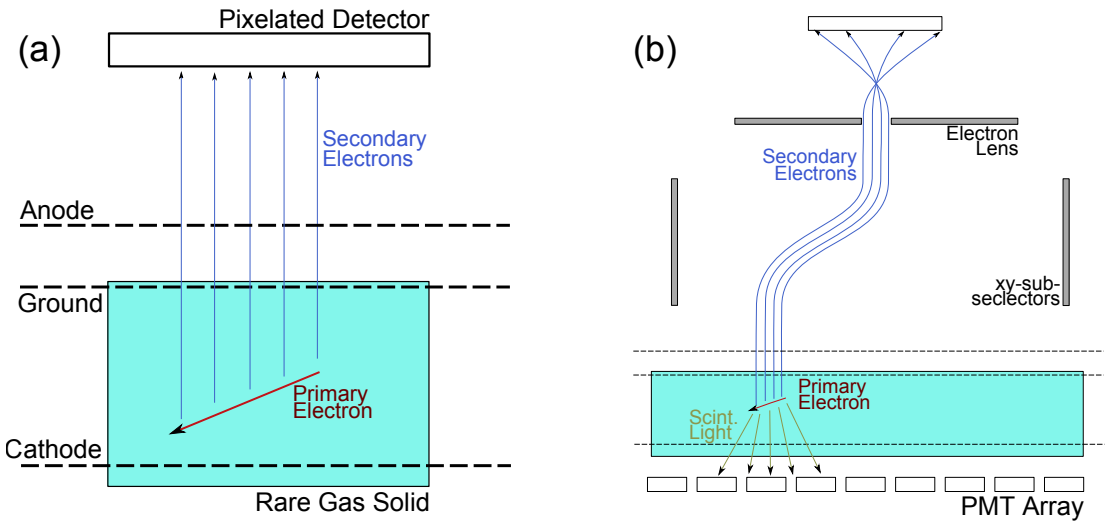

Figure 3.1.: (a) Scheme of the basic components of a RGS-detector. At the bottom, the detector sensor material can be seen, where ionising particles interact with the atoms of the material and generate secondary electrons by energy deposition. The secondary electrons are drifted to the surface due to an electric field. There, a flat detector with spatial resolution evaluates the 2D-projection of a 3D-track. **(b)** The same design including the electron optical system which is necessary to cope with the large dimension of the $\beta\beta$-signal mass.

The secondary electrons finally are projected onto a pixelated tracking detector. Since the secondary electrons carry all information of the primary particle trajectory, the tracking detector requires spatial resolution to reconstruct the primary trajectory. Additionally, the shaping of the electric field is important to conserve the spatial information of the secondary electron signal. As a result, electron optical considerations have to be done. In this conceptual framework, the Timepix-detector is used to act as pixealted imaging detector (see section 3.3). It is shown in black at the top of the experimental design in figure 3.1a.

Due to the extremely low $\beta\beta0\nu$-rate, a large mass of the decaying isotope is required. This involves large-scaled particle sensors. In order to achieve tracking experiments in this case as well, an electron optical system is required, which is supposed to deflect every possible $\beta\beta0\nu$-track onto the imaging detector. A concept for this setup design is presented in figure 3.1b. The sensor material, the potential electrodes and the drifting secondary electrons in the sensor are identical whereas the scale of the sensor is much larger. The electron optical system is supposed to only look at the specific square of the sensitive volume where the interaction occurs. Any particles originating from this square are deflected onto the optical axis and focussed by an electron lens. The proper choice of the selector fields can be

done by a PMT array with spatial resolution beneath the sensor materials, which determines the interaction point by detecting the scintillation light. The primary track is projected onto the Timepix sensor layer to evaluate the secondary electron track as in the first scheme. The interaction signal can be amplified by accelerating the secondary electrons after the emission form the sensor.

This electron optical system would be a big step forward to realize tracking experiments with large-scaled sensor. Therefore, the main focus of this work is on simulating the required potential distribution for the imaging of a secondary electron track. The geometry and simulation results of a possible electron optical system are presented in chapter 4. The system is merely realised in simulations since basic experiments have to prove the individual parts of the detector presented in figure 3.1a before the electron optical components actually are constructed. One of the first basic projects considering rare gas solid detectors is presented in chapter 5.

3.2. Properties of Solid Xenon as Particle Detector Sensor

In this section, some basic properties of solid xenon are presented, which are of importance considering the suitability of this rare gas solid (RGS) for particle detector applications. Generally, rare gases are very much favoured for many different kinds of experimental applications – especially in the gaseous and liquid state. There are several advantages of rare gases e.g. the inert character. Rare gases can be cleaned easily and chemical alteration can be avoided if exposed to energetic particles [12]. As a result, this allows the application of large scaled sensitive volumes with a low contamination level. Furthermore, rare gases can be enriched easily – a very important property regarding $\beta\beta0\nu$-searches with xenon sensors, for which the abundance of the intrinsic $\beta\beta$-isotope ^{136}Xe needs to be increased significantly.

3.2.1. Excitation Process and Secondary Electrons

The basics of the creation of secondary electrons due to fast incident particle are already explained briefly in section 2.2. Solid xenon is a nonpolar and monoatomic insulator with a band gap of 9.28 eV (see [20], tab. 2.4 and [21], tab. II). As a result, there is no possibility to excite any vibrational and rotational modes. Nearly all of the deposited energy E_Σ is used to excite or ionise atoms of the xenon lattice. On the other hand, due to the high band gap, less charge is created in solid xenon at a given interaction compared to other sensor materials as one can see in table 2.1.

Electron-hole pairs are produced very quickly after the interaction in RGS with delay times in the order of 10^{-16} to 10^{-14} s [12]. Besides direct ionisation, other processes like Auger electrons, inner-shell vacancies and ionisations created by cascade effects of fast secondary electrons also contribute to $N_{\mathrm{e/h}}$ [12]. However, the observable number of secondary charge carriers tends to be smaller than the value $N_{\mathrm{e/h}}$ according to equation 2.8 due to the escape of energy by fast secondary electrons or fluorescence effects [11].

The initial energy of secondary electrons is predicted to follow a $1/E^2$-distribution with a shape similar to the post-emission spectrum presented in figure 3.3a below [11], [22]. The initial energy also differs due to a distribution of the term $\bar{\epsilon}$ (see again equation 2.8).

3.2.2. Charge Carrier Transportation

Once produced, secondary charge carriers as electrons and holes undergo a random walk in the lattice while losing energy due to the creation of phonons [11]. Since solid xenon is a nonpolar material with a simple fcc lattice, the charge carriers solely can lose energy due to the creation of acoustic phonons which have an energy of less than 5.4 meV in solid xenon (see [23] fig. 27).[1] Consequently, the energy loss rate is very small. Secondary electrons undergo many collisions in the lattice until they are finally trapped by impurities e.g. chemically different bulk centres, defects in the crystal lattice or positively charged holes.[2] As a result, all energy deposited in the sensor material is converted into scintillation light and heat.

The multiple collisions of secondary electrons imply a loss of information considering the orientation and energy distribution of the track. This can be avoided by introducing a preference direction to the electron movement if a homogeneous electric field is applied over the sensitive volume. As a result, secondary electrons are accelerated up to a certain drift velocity v_{D}, which depends on the electric field strength as well as the characteristic sensor material. The electron are drifted parallel to the electric field. The corresponding side of the sensor material can be connected to some kind of imaging device in order to detect the arriving secondary electron signal from the primary particle interaction. By doing so, particle tracking experiments can be realised.

[1] This figure presents the measured phonon energy in terms of the terahertz-frequency. This has to be distinguished from the actual phonon frequency in the lattice ω_{k} according to the dispersion relation since the corresponding harmonic oscillator energy eigenvalues are derived by quantum mechanics. The maximum phonon energy appears at the X- and L-point of the first Brillouin zone with a frequency of about 1.3 THz, which corresponds to 5.4 meV as mentioned above.

[2] Or until they escape through the crystal surface if their energy is large enough (see next subsection).

Quantity	Value	Source
e^--mobility μ_e (solid)	$\sim 4500\,cm^2s^{-1}V^{-1}$	at 157 K [9], tab. I
	$4000\,cm^2s^{-1}V^{-1}$	at TP [21], tab. I
e^--mobility μ_e (liquid)	$2200\,cm^2s^{-1}V^{-1}$	at 163 K [9], tab. I
	$1900\,cm^2s^{-1}V^{-1}$	at TP [21], tab. I
H^+-mobility μ_H (solid)	$2 \times 10^{-2}\,cm^2s^{-1}V^{-1}$	[9], tab. I
	$1.8 \times 10^{-2}\,cm^2s^{-1}V^{-1}$	[21], tab. I
sat. drift vel. $v_{D,sat.}$	$5.5\,cm\,s^{-1}$	[9], tab. I
	$5.77\,cm\,s^{-1}$	[21], tab. I

Table 3.1.: Measurements of the low field mobility of electrons and holes in solid xenon and the saturated drift velocity.

The drift velocity describes the drift movement of a whole bunch of electrons as produced during the interaction of the sensitive volume with a a fast ionising particle. However, the single electrons inside this bunch may have a significantly larger kinetic energy due to multiple collisions with the lattice centres. The mean free path λ of secondary electrons typically is much smaller than the total drift distance travelled in the lattice [11]. The energy of the individual secondary electrons again follows a similar distribution as shown in figure 3.3a with a peak at rather low energies and a small high-energetic tail. The average energy $\bar{E}_e$ can be increased significantly by applying a stronger electric field. This is called *effective heating* of the secondary electrons [10].

At low fields, secondary electrons are accelerated smoothly with respect to their mean free path in the lattice. Such electrons are called *cold electrons* which refers to their kinetic energy, which is at the order of $k_B T$. In this domain, v_D is proportional to the electric field strength E_D and the corresponding quotient is called the low-field mobility μ_e of electrons. The mobility indicates the resistance of a certain material for drifting electrons at which small values correspond to bad drifting properties of the given material. In the case of condensed rare gases, the electron mobility is very large as shown in table 3.1. This is a "remarkable and probably unique feature" of RGS ([21], p. 1141). Due to the high value of the electron mobility, such electrons are also called *quasi-free electrons* since they are allowed to propagate in the lattice without major attenuation. This property lead to a very long free mean path of electrons in condensed rare gases [21]. Due to this feature and the small energy loss rate mentioned above, the electron escape depth is very long in RGS, which in turn facilitates the design of large-scaled RGS-sensors

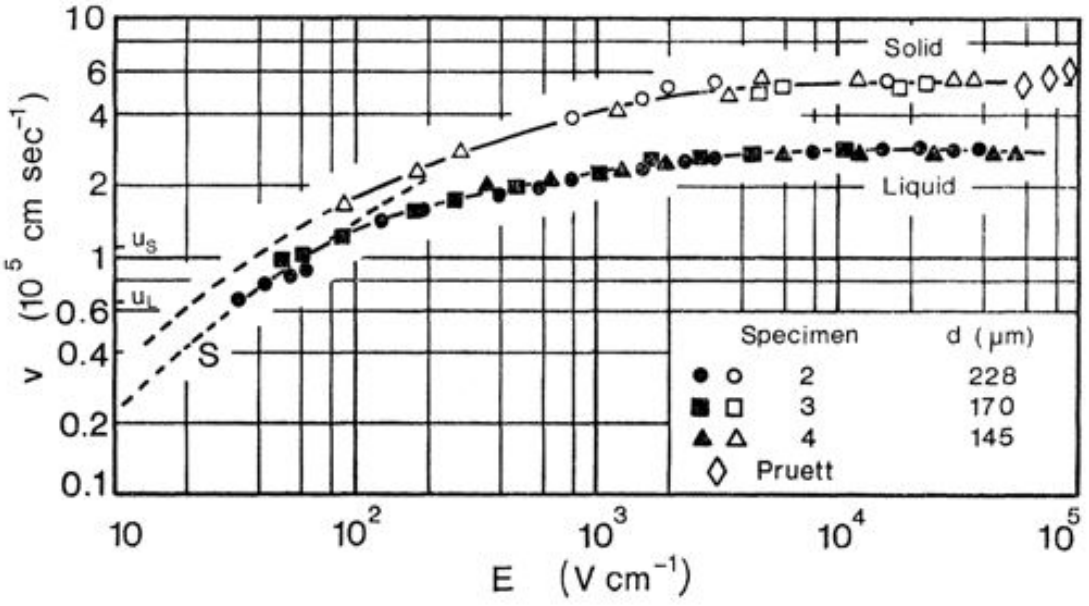

Figure 3.2.: High-field drift velocity v_D of electrons in liquid (163 K) and solid xenon (157 K). v_D increases with the electric field strength and saturates above 5 kV cm^{-1} with a $v_\mathrm{D,sat.}$ of about 5.5 $\times$ 10^5 cm s^{-1} in the case of solid xenon. The velocity of sound u for liquid and solid xenon are indicated at the y-axis. This plot is taken from [9].

using condensed xenon [11][3]. Furthermore, the ratio of μ_e of solid and liquid xenon is about 2.1 which makes solid xenon much more preferable as sensor material [9], [21]. Additionally, the low-field mobility increases with smaller temperatures so that electron transport in RGS is even more supported under cryogenic conditions. Measurements with solid argon indicate a $T^{-3/2}$-dependency, which can be assumed to be roughly similar in the case of the other RGS [9].

At a higher electric field strength, a transition to a $E^{1/2}$-dependency occurs and finally, v_D saturates at a characteristic velocity-level. Figure 3.2 shows measurements of v_D versus the electric field strength for liquid and solid xenon [9]. The low field region is not plotted due to experimental reasons, the $E^{1/2}$-region is indicated by dotted lines and the saturation of v_D occurs above 5 kV cm^{-1} with a saturation value $v_\mathrm{D,sat.}$ of about 5.5×10^5 cm s^{-1} in solid xenon [24], [9]. The ratio of $v_\mathrm{D,sat.}$ for the solid and liquid phase is about 1.9 and quite similar to the ratio $\mu_\mathrm{e}\,(\mathrm{sol.})/\mu_\mathrm{e}\,(\mathrm{liq.})$ presented above. It is important to mention again that v_D only describes the velocity of the whole drifting electron bunch. In the case of high field

[3]The electron escape depth is fairly field-dependent. For example, in the case of very weak internal fields, massive electron attenuation effects occur with electron escape depths of only about 0.18 μm [12]

strengths, the individual electrons are heated up well above the thermodynamic equilibrium $k_{\mathrm{B}}T$ as explained in the following subsection [10]. As well as the low-field mobility, also the saturated drift velocity depends on the temperature of the condensed rare gas. In the case of solid xenon, $v_{\mathrm{D,sat.}}$ is observed to increase with falling temperature and a value of $10^6\,\mathrm{cm\,s^{-1}}$ can be achieved below 100 K ([25], fig. 1). As a consequence, the excellent electron drifting properties of solid xenon are maintained at temperature far below the melting point which is an important feature of this RGS as presented in section 5.3.

It is also possible to detect well-defined signals of the drifting hole in solid xenon at temperatures slightly below the melting point, albeit no saturation effect similar to the electron drift velocity can be observed [9]. The hole mobility is $2 \times 10^{-2}\,\mathrm{cm^2 s^{-1} V^{-1}}$ according to table 3.1. This fairly small value indicates the bad excess hole transportation properties of RGS in general. A reason for that observation might be the formation of immobilised excess holes (especially in solid argon and krypton) whereas Xe^+ or Xe_2^+ centres may be sufficiently unstable to allow hole transport to take place [9]. Besides that, the insulation property of solid xenon might also be a reason for the low hole-mobility. In fact, it can be shown that the hole mobility in solid xenon is maintained and even increased at temperatures down to 111 K ([26], fig. 1 and [21], fig. 7).

As mentioned above, secondary electrons can be trapped by molecular impurities in the sensor material and crystal defects. Especially strongly electronegative impurities as oxygen have a large trapping efficiency so that the lifetime of electrons in condensed rare gases can be assumed to be predominantly limited by oxygen impurities [9]. Such impurities also include oxides as H_2O or CO_2 that also presents a significant drop in the electron yield per incident particle with increasing concentration [11]. Additionally, even though considerable concentrations of so-called quencher gases can enhance the electron mobility, such admixtures decrease the electron life time in condensed rare gases. For example, significant concentrations of the nonpolar quencher gas methane in liquid argon is shown to decrease the attenuation length of electrons measurably [27]. However, even at concentrations of 20 mol % CH_4 an attenuation length of still 11.8 m can be expected at $1\,\mathrm{kV\,cm^{-1}}$ in liquid argon. Considering the increasing attenuation length with better purification of the drift medium and the much better electron transport properties of xenon (and especially solid xenon) compared to liquid argon, significantly larger attenuations length can be expected in the case of a xenon RGS.

3.2.3. Secondary Electron Emission from RGS

After having been drifted to the crystal surface due to the electric field, secondary electrons are faced with a surface potential barrier that has to be overcome in order to escape the insulator. The height of this barrier is the so-called electron

Quantity	Value	Source
electron affinity U_a	0.5 eV	[29], tab. I
	0.42 eV	[10], tab. I
	0.4 eV	[28], tab. 4.2

Table 3.2.: Overview of several experimental values for the electron affinity in solid xenon.

affinity U_a, which is a characteristic property of the given material. Since this barrier influences the emission process to a far extend, it is important to determine the value of U_a. The results from several experimental approaches are presented in table 3.2. The electron affinity is slightly lowered if strong electric fields of about $10^3\,\mathrm{V\,cm^{-1}}$ are applied but this decrease is rather small compared to U_a [10]. The electron affinity of liquid xenon depends on the density of the material (see [28], fig. 4.10) [4]. Solid xenon is assumed to present the same behaviour so that qualitatively, U_a is reduced with increasing density. This in turn supports the emission probability of secondary electrons out of solid xenon with decreasing temperature.[5]

Due to the electron affinity, secondary electrons below a certain energy are blocked at the transition zone from the crystal to the gaseous phase above. The escape is only possible, if the kinetic energy component perpendicularly to the crystal surface exceeds U_a. However, considering the saturated drift velocity presented in table 3.1 the corresponding kinetic energy of the secondary electrons is only about 0.086 meV and hence significantly smaller than U_a. Furthermore, the height of the electron affinity results in a potential barrier that is too broad for the existence of the tunnel effect. As a consequence, the emission of electrons from solid xenon is neither thermionic nor due to field emission processes. Yet it is connected with the heating of the secondary electrons inside a drifting bunch because of the penetration of the electric field in the insulator as mentioned above [24], [10]. In this way, the average energy $\bar{E}_e$ of the secondary electrons significantly exceeds the thermodynamic equilibrium $k_B T$ in the case of high internal fields, which is why such electrons are referred to as *hot electrons*. For example, the energy at $k_B T_b$ is about 0.014 eV, which is far more than the kinetic energy corresponding to $v_{D,sat.}$. However, due to the electron heating caused by the electric field, $\bar{E}_e$ is significantly

[4] According to table A.2, the density of liquid xenon is $3100\,\mathrm{kg\,m^{-3}}$ or in terms of the atomic density $1.6 \times 10^{22}\mathrm{cm^{-3}}$. Considering fig. 4.10 in [28], the resulting electron affinity agrees with the values given in table 3.2.

[5] The crystal density increases with smaller temperatures (see table A.2).

larger.[6] Measurements at $2\,\mathrm{kV\,cm^{-1}}$ yield values of $1 \cdot 10^{-5}\,\mathrm{cm}$ for the mean free path λ and $0.5\,\mathrm{eV}$ for $\bar{E}_\mathrm{e}$, which is comparable to U_a so that emission is possible (see [24] for values and [11], especially fig. 14).

As a consequence of the secondary electron heating up to $\bar{E}_\mathrm{e} \sim U_\mathrm{a}$, emission coefficient curves present a threshold of the electric field with no emission at all below field strengths of about $1.25\,\mathrm{kV\,cm^{-1}}$ in the case of solid xenon. Above about $5\,\mathrm{kV\,cm^{-1}}$, the coefficient curves saturate and practically all secondary electrons are emitted in the gas phase [24], [10]. The effective electron lifetime and hence the escape length therefore can be very long under presence of an electric field [11]. In the case of such electron temperatures, emission occurs very fast and electrons attenuated by the surface potential barrier do not remain in the transition layer for more than $0.1\,\mu\mathrm{m}$ [10]. Furthermore, thermoactivated electron emission should be possible in the case of much weaker fields as well, if the electron life time exceeds the surface barrier attenuation time for such field strengths. However, this requires rare gas purification levels that are not achieved yet (see [20], sec. 3.3.1.2).

The actual electron emission process from the insulator into the gas phase requires a longitudinal kinetic energy component larger than U_a. The angular shape of the escape cone follows a cosine-law distribution with a slight dependency on the kinetic energy of the secondary electrons (see [22], fig. 10). This escape cone can be described mathematically as:

$$\cos\,\theta = \frac{p_\perp}{p} > \left(\frac{U_\mathrm{a}}{E}\right)^{1/2} \quad , \tag{3.1}$$

where p and E is the momentum and the energy of the electron inside the insulator and θ is the angle between the surface normal and p [11]. As a result of the angular relation, the angles of the secondary electrons hitting the insulator surface from inside the sample present the same intrinsic shape. For that reason, the distribution of the secondary electrons of the drifting electron bunches inside the lattice has to be isotropic (see [22], sec. III.a.2.a). This conclusion is consistent with the negligible preference velocity v_D compared to the significantly larger average secondary electron energy $\bar{E}_\mathrm{e}$ which also leads to an isotropic angular distribution of the electron momenta.

Figure 3.3a presents the energy distribution of secondary electrons in its general shape whereas figure 3.3b shows the case of the insulator MgO [22],[30]. Both plots present the initial energy distribution plotted as secondary electrons flux $\Delta\,N_S/\Delta\,V$. The energy dependency mainly originates from the field-induced heating of the secondary electrons achieving energies well above the thermodynamic equilibrium. A relatively sharp maximum corresponding to the most probable energy can be

[6] This is not getting reflected in v_D due to the multiple collision of electrons with the lattice centres.

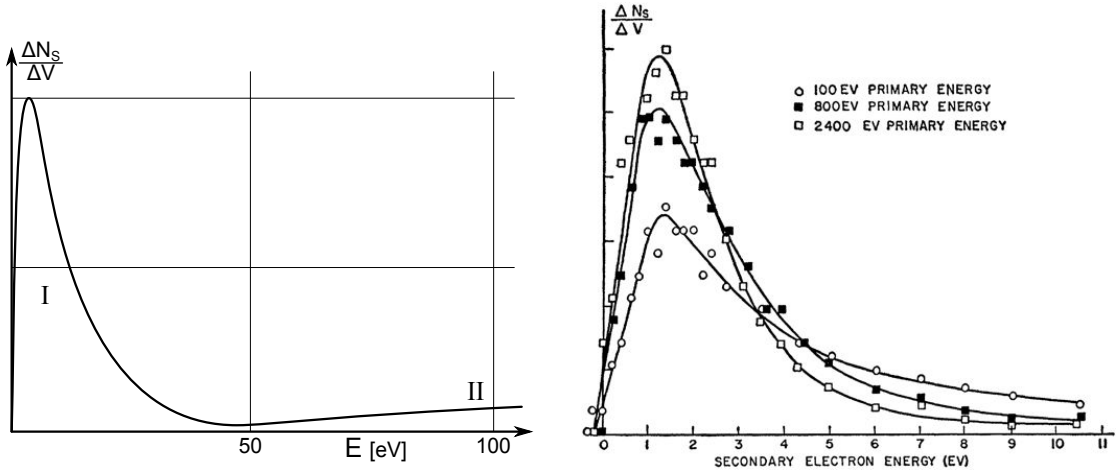

(a) General shape **(b)** MgO

Figure 3.3.: Energy distribution of secondary electrons after emission from an insulator. **(a):** General shape of the electron flux over the energy. A maximum is developed at several eV (I). The long tail at higher energies resembles the Maxwell–Boltzmann distribution although they have nothing in common. The slight increase above 50 eV (II) is no effect of *true secondary electrons* but is due to so-called *rediffused primary electrons*. This plot is redrawn from [22]. **(b):** Energy distribution in the case of the insulator MgO at different primary electrons. All curves are normalised. The maximum is slightly above 1 eV. This plot is taken from [30].

seen at several eV (a little more than 1 eV in the case of MgO). The shape of the distribution is strongly influenced by the potential barrier at the surface which is also the main reason for the distinct maximum [22],[30].

3.3. The Timepix Detector

As presented in figure 2.6, pixelated detectors as the Timepix detector can be used as imaging device for particle tracks. This semiconductor detector is a modification of X-Ray imaging detectors developed mainly for medical imaging purposes by the Medipix-Collaboration.[7] In this section, the design and functionality of the Timepix detector is explained. A close look on the components and physics of pixel detectors is presented in [16] whereas [31] gives detailed information about the detector calibration process (especially section II.4 and chapter III).

[7]See also the Medipix homepage: `http://medipix.web.cern.ch/medipix/`

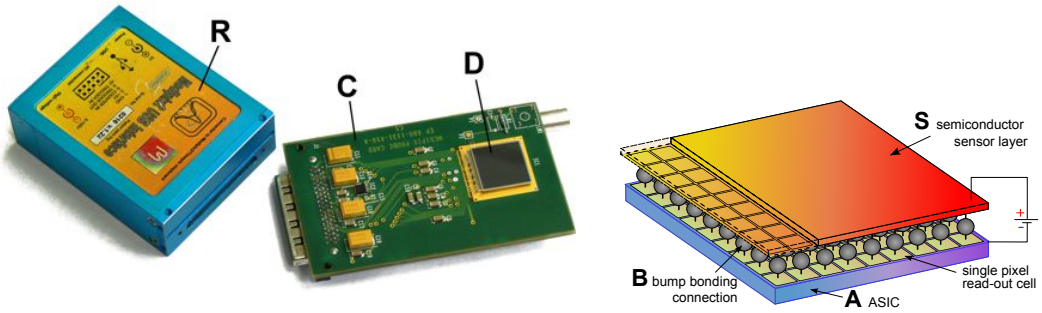

(a) Picture of the Timepix and Readout **(b)** Scheme of the sensor

Figure 3.4.: This picture and scheme of the Timepix detector shows the actual detection part (D) mounted on the chipboard (C), which is connected to the readout device (R). The detector itself consists of the sensor layer (S) which is conntected to the ASIC (A) via bump bonds (B). The pixelation of the ASIC and the voltage for the drift field inside the sensor material are indicated.[8]

3.3.1. Detector Design

Common particle detectors consist of a sensitive volume where the interaction takes place, a signal processing part and a readout that transmits this signal to the computer software. The Timepix detector also includes these three parts. Figure 3.4a shows a picture of the detector chipboard and the associated USB readout device. The scheme in figure 3.4b shows the vertical structure of the sensor layer and the ASIC.

The sensitive volume of a Timepix detector is the sensor layer (S) located at the top of the pixelated ASIC (A).[9] Each pixel of the ASIC and the sensor layer are equipped with electrical pads and each pad pair is connected via bump bonds (B). Bump bonds are small pieces of soft metals or conductive films, which allow charge transport from the sensor layer to the ASIC. The ASIC is connected to the chipboard (C) via thin and sensitive wires – the so-called wire bonds. They can be seen in figure 3.4a on the left edge of the detector core. Beside the actual detection unit (D), the chipboard contains all the electronics that is necessary for the power supply of both sensor layer and ASIC, the external control and the transmission of the signal from the ASIC to the readout device (R).

[8] The sign of charge carriers, which are drifted towards the ASIC to generate the charge pulse, depend on the direction of the drift field. In the case of silicon sensors, these charge carriers are holes whereas in the case of cadmium telluride electrons are collected. This scheme shows a silicon sensor layer.

[9] The acronym stands for *application-specific integrated circuit* and refers to a pixelated, monolithic chip here, which is specifically adapted to the purpose of the customer or user. An ASIC is therefore highly efficient yet barely manipulable.

In the case of the Timepix and Medipix detectors, the sensor material is a doped and depleted semiconductor layer (e.g. silicon or cadmium telluride) with a regular thickness of about 300 µm to 1000 µm. The imaging surface is about 14 mm squared. Incident ionising particles deposit energy and generate charge carrier pairs in the sensor layer as explained in section 2.2. Due to the applied electric field (see figure 3.4b) the positive charge carriers are drifted in direction of the ASIC.[10] The sensor layer is connected to the ASIC where the charge that is deposited in every pixel is converted to a voltage pulse that is proportional to the deposited charge and hence to the deposited energy. The voltage pulse carries the energy information of the particle interaction and is transmitted to the readout.

The pixelation of the ASIC enables space-resoluted imaging of the propagation trajectory of ionising particles in the sensor layer. The Timepix ASIC provides 265×265 pixels with a pixel pitch of 55 µm. Depending on the purpose, detectors with a pixel pitch of 110, 220 µm and so on can be realised by simply connecting only every second, third, etc. ASIC pixel to the sensor during bump bonding. Each pixel has its own electronic architecture to process the accumulated charge from the sensor volume above the pixel and hence, the Timepix detector is able to gain information of each independent pixel at the same time.

3.3.2. ASIC Signal Processing

The processing of the voltage pulse of the charge carriers that are drifted in the sensitive volume is carried out in the ASIC pixels. The Timepix can be run in two different modes and allows to obtain either the deposited energy per pixel or a timing information in every pixel from the votlage pulse (depending on the mode of operation). The signal processing in these modes happens as shown in figure 3.5. The voltage pulse (or charge pulse) of an incident particle interaction hits the ASIC at a certain time within a frame time interval. Afterwards, the pre-amplifier shaping generates a triangular pulse. The slope of the rising and falling edge can be manipulated by so-called DAC-values.[11] Since electronic and thermal noise plays an important role in the ASIC, it is necessary to set a *threshold level* (THL) and to ignore signals that do not exceed this limit. This process is carried out by the discriminator unit based on a THL-DAC-value. The remaining part of the pulse above the THL is used to determine the deposited energy information.

The ASIC contains an internal clock which provides steady clock pulses with a frequency up to 48 MHz. These clock pulses are used to scan the pulse above

[10] I.e. the positive electron holes left by the ionising primary particle. Changing the sign of the voltage will cause the secondary electrons to drift in this direction but the physics going on in the pixel cells stays the same.

[11] This is an abbreviation for *digital analogue converter* – a component which is essential to control the analogue ASIC based on external settings.

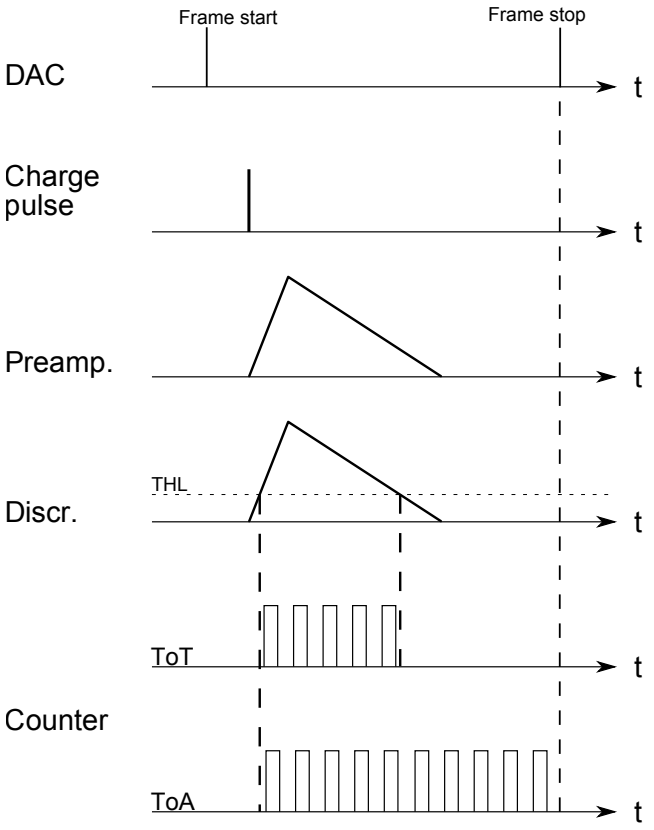

Figure 3.5.: This plot presents an overview of the pulse converting process in each pixel of the ASIC. The individual plots illustrate the processing steps from top to bottom in logical order based on one particular frame. On the left, the electronic element responsible for each processing step is named.

the THL. As soon as the pulse exceeds the THL for the first time, a counter unit starts to count the clock pulses until the pulse falls below the THL again. The length of this time interval above the THL depends on the maximum height of the charge pulse, which in turn depends on the energy deposited in the sensitive volume. Measuring the clock pulses while the pulse exceeds the THL therefore provides a value for the deposited energy in the sensor layer above a particular pixel. This measurement mode of the Timepix detector is called *Time-over-Threshold* mode.

Another mode is the so-called *Time-of-Arrival* mode shown on the bottom plot in figure 3.5. In this mode the counting of the clock pulses is stopped with the end of the frame instead of the pulse falling below the THL again. The ToA mode provides an arrival time information of the charge pulse at a particular pixel within one frame. Since the starting and stopping time of one frame is the same for the entire pixel matrix, the ToA information can also be used to compare the detection time of a specific event amongst all pixels. This allows for example the calculation of the perpendicular distance of a particle track to each pixel cell and hence 3D-reconstruction techniques. Additionally, the ToA mode provides the possibility to separate several independent events by measuring coincidences in

the signal arrival times between different pixels of the ASIC. This might facilitate low-background experiments as $\beta\beta0\nu$-searches.

The third and last mode is the so-called Medipix mode. In the Medipix mode, the Timepix detector counts the number of interactions per pixels and can be used as a simple pixelated counting detector.[12]

[12]This is why the Medipix detector does not need to include any internal clock.

4. Simulation of the Electron Optics System

Contents

This chapter presents the simulations of an electron optical system consisting of a space dependent selector system and an electrostatic lens according to figure 3.1b.

The basic principles of electron optics and electrostatic lenses are explained in section 4.1 whilst the motivation for the application of such a system is explained in section 3.1. Section 4.2 explains the simulation program COMSOL. Section 4.3 then shows an overview of the setup and section 4.4 takes a closer look on the basic features of the individual simulated components. Section 4.5 summarises the simulation results whereas section 4.6 closes with the CAD drafts of the experimental setup including the electron optical system that were created and simulated as well.

4.1. Qualitative Introduction to Electron Optical Systems

4.1.1. Basic Principles

The field *electron optics* describe electron (or ion) trajectories in electromagnetic fields from an optical angle. Macroscopic electric and magnetic fields can be used in electron optical systems to manipulate electron beams in the same manner as in photo-optical systems. Additionally, it is possible to introduce acceleration or deceleration fields depending on the sign of the applied potentials. In this work, only electrostatic fields were used. These fields are introduced by potentials applied to several potential plates. The geometrical arrangement of these plates and their shape eventually determine the motion of the electrons in the experimental setup.

The most important element in the optical system is the lens. To achieve a lensing effect in electron optics, electron trajectories need to be focussed to a focal point. This can be realised by introducing converging electric fields. Usually, it is more conceivable to regard the equipotential lines instead of the electric fields of a given potential distribution. Due to the fact that the strongest field strength gradients always are perpendicular to the equipotential lines, potential plots allow to image better the effect of the involved electric fields. Furthermore, the shape of equipotential lines reminds of the usual concave or convex lenses in photo-optics which makes it easy to see the effect on the beam.

Figure 4.1 presents an example to illustrate this point. The upper picture shows the potential contour lines of a Braun cathode tube as it is used in old CRT television sets. On the very left, a hot cathode emits electrons in direction of the z-axis. First they cross the inside area of a cylinder electrode with a positive potential of about 1 keV. Due to the potential difference to the negative cathode, the equipotential lines get a convex shape. This implies a dispersion effect of the

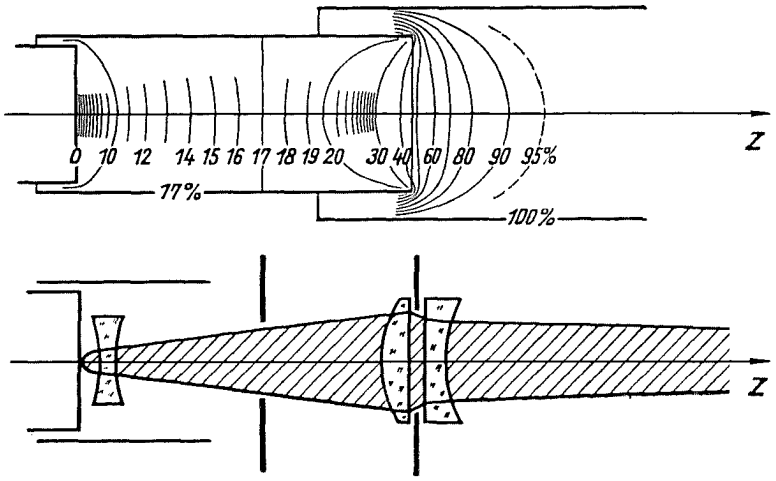

Figure 4.1.: The Braun cathode tube is a basic example for an electro-optical system, which can be used to focus an electron beam in CRT television sets. The upper scheme shows the setup consisting (from left to right) of an electron source, a cylinder electrode with positive potential and a second cylinder with larger diameter and higher potential. The concave or convex shape of the equipotential lines indicate the corresponding impact on the electron beam. The lower scheme shows the photo-optical analogy to the electro-optical components. This figure is taken from [32].

electron beam as presented in the photo-optical analogy below.[1] Afterwards, a second larger cylinder follows which has a significantly higher positive potential than that of the first cylinder. The resulting electric field is much stronger than the first so that the contour lines inside of the first cylinder are bulged to the left. This leads to a focussing of the electron beam compared to a photo-optical collecting lens. At last, the equipotential lines indicate a second concave field which compensates the focussing effect. Additionally, due to the larger field, the long contour lines (those are shown in increments of ten percent) are stacked more tightly indicating the main acceleration area is located at this point.

The functionality can be described mathematically as well. In the case of electron optical systems, the refractive index n corresponds to $\sqrt{\Phi}$ so that the refraction is caused by equipotential lines or rather equipotential planes as mentioned above. The entire mathematical representation of n at the transition of two region with different but constant potential is [33]:

[1] The field arrows point from plus to minus so that the electrostatic force upon negative electrons is directed the other way round. In this case, the force arrows point in direction of the z-axis causing a dispersion effect.

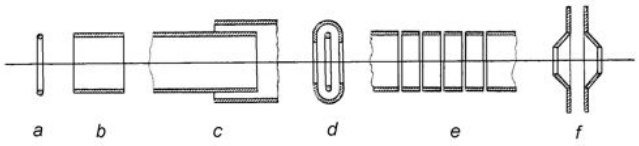

Figure 4.2: This overview presents several schemes of different electrostatic lens designs. This figure is taken from [32].

$$n = \sqrt{1 + \frac{\Phi_0}{\Phi}} \quad , \tag{4.1}$$

where Φ is the potential of the electron beam before crossing the equipotential plane and Φ_0 is the potential beyond the plane. In this simple case, there are only two equipotential regions and one plane and the calculation of the refraction index is very easy. In reality, electric fields are widely extended and as a consequence, the determination of particle trajectories in electric fields is rather complex. Especially in the case of inhomogeneous lensing fields, this task has to be done with powerful simulation programs. The exact arrangement, the shape and the field strength of the electrodes eventually determine the effect on the trajectories and hence the optical imaging properties.

4.1.2. Fundamental Electron Optical Elements

The most important element of electron optical systems is the electron lens. As mentioned above, the specific geometry of an electron lens creates a potential distribution which leads to a focussing or diverging effect on a crossing electron beam. Typically, such lenses are rotation symmetrical so that aperture plates or cylinders (as in the case of the Braun tube) are often used for developing electron optical systems. In this work, by the term *aperture plate* a plate is meant which is equipped with a small pinhole in its middle. The plate dimension has to be significantly larger than the size of the pinhole while the actual shape is not very important.[2]

The lensing effect can be restricted to a well defined area by the usage of several electrodes which are located quite close to each other. By doing so, the impact of the electric field on the electron beam is encapsulated in a small area, since all concave or convex equipotential lines are packed together in the transition zone between two related lenses. This leads to a better possibility to regulate the lensing effect by adjusting the corresponding lensing potentials.

[2]The rotation symmetry only refers to the pinhole and such the transit point of the particle trajectories one intends to manipulate. As long as the plate is quite large compared to the pinhole diameter, the electric fields close to the optical axis presents a rotation symmetry, too.

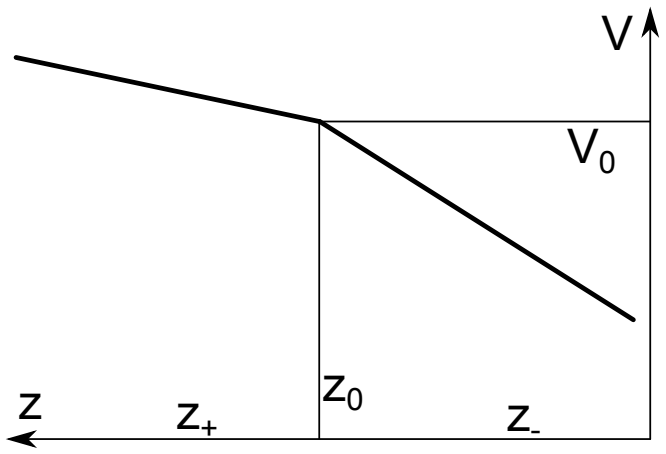

Figure 4.3: This scheme presents a transition between two potential differential quotients generated by a single lens. This figure is redrawn from [34].

Figure 4.2 shows several types of electron lenses. The simple pinhole lens (a) and the cylinder lens (b) can be seen. The third type (c) corresponds to the lens type which is used in the Braun cathode (see figure 4.1) and acts as a good example for a rather small scaled lensing area. This lens type is also called *immersion lens*. [3] An even stronger field compression can be achieved by a lensing system consisting of three aperture lenses with identical optical axis (d). Typically, the three associated potentials are applied in a $-/+/-$ arrangement. A modification of this lens type is the aperture lens systems, which consists of three separated aperture plates in a row and provides a better regulation of the lensing effect since all potentials can be applied individually. The last lens type shown here is an arrangement of several aperture plates or cylinder electrodes (e). This lens allows to shift the lensing area in order to chose the magnification factor of the lensing system. At last, further structural adjustments as the usage of cone-shaped electrodes (f) might improve the lensing properties of the electron optical system.

The focussing effect of electric lenses can be described mathematical based on the definition of the refractive index presented in equation 4.1. In the simplest case of a single electron lens, one can approximate the potential distribution by two areas with different potential differential quotients separated by the lensing plate in their middle. This approximation is presented in figure 4.3. The lens is located at z_0 and has a potential V_0. The thick line indicates the potential depending on the specific z position and V' is different left (z_+) and right (z_-) of the lensing plane. Based on this potential distribution, the focus f of a paraxial electron beam is given by [34], [35]:

[3] The term *immersion lens* refers to any kind of lens that is embedded between two areas with different refractive index n. The term has its origin in immersion microscopy, where an oil film is applied between an object and the objective that prevents light rays to be diffracted away from the microscope. Since $n \sim \sqrt{\Phi}$, the immersion lens can be seen as transition zone between two areas with different potentials as in the case of the Braun tube.

$$\frac{1}{f} = \frac{V'_{z+} - V'_{z-}}{4\,V_0} \quad . \tag{4.2}$$

In this equation, the second derivative of the potential V'' is assumed to be zero except at z_0. Realistic potential distribution of actual lenses are far more complicated – especially in the case of complex lens types. Due to the complexity of the mathematical description in the case of such lenses, the determination of their realistic potential distribution has to be done by simulations.

Another important electron optical element is the electron mirror. Basically, each electron lens can also act as a mirror as long as the negative potential is large enough to represent a barrier to the electrons depending on their kinetic energy. In the simplest case, the mirror is realised by a single potential plate without aperture hole [36]. It can be extended by a second potential plate with opposite potential and fac eto face with the first plate. In this way, a plate capacitor is established in which particle beam can be deflected much more predictable than in the diverging electric fields of a single mirror. Such deflector plate pairs are also used in CRT television sets to change the position of the electron beam with respect to the monitor.

Other electron optical elements are a wide range of magnetic lenses with different designs or the cylindrical capacitor. These elements allow further structural possibilities to construct electron optical systems but since they are not included in the framework of this thesis, they are merely mentioned in this chapter. More information about such lens designs and about electron optics in general can be found in [37], [34], [33].

4.1.3. Imaging Errors of Electron Optical Systems

Imaging errors is the general term for all kinds of deviations between the actual path of a beam and the ideal path predicted from mathematical formulas describing optical imaging. These deviations are often simply referred to as *aberrations*. The mathematical formulas can be used for photo-optical systems as well as for electron optical systems since their mathematical description follows the same formulas. Within this theory, electrostatic equipotential lines correspond to planes with constant refraction index (compare with footnote 3).

Imaging aberrations can be subdivided in several categories. In electron optics, the most important aberrations are the chromatic aberration and the third-order aberrations. The term third-order aberrations summarise several different imaging derivation of which the spherical aberration is the most significant. The term *third-order aberrations* refers to the mathematical framework of electron optical systems and the corresponding formulas are based on the angle α between the

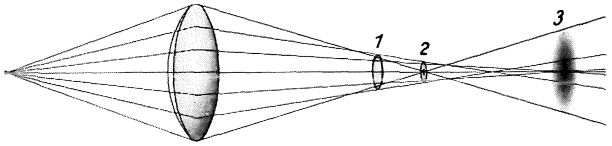

Figure 4.4: This drawing shows an example for spherical aberration in photo-optical systems. The lens deflects off-axis beams under a larger angle so that there are different focal lengths which blurs the image. This figure is taken from [38].

electron beam and the horizontal plane containing the optical axis. This angle occurs in several trigonometric formulas that can be expanded in the following way:

$$\sin\alpha = \alpha - \frac{\alpha^3}{3!} + \frac{\alpha^5}{5!} - \frac{\alpha^7}{7!} + \cdots \quad . \tag{4.3}$$

For rather small angles α, the small-angle-approximation can be used and the imaging process is ideal since no aberrations occur. In reality this condition is fulfilled only for beam paths close to the optical axis. However, off-axis beams are necessarily required as soon as it comes to the imaging of extended objects. This implies that high-order aberrations cannot be neglected any more. The lowest order carries the angle to the power of three and the corresponding imaging deviations are called third-order aberrations.

Spherical aberrations are caused by different deflection strengths of the lens depending on the distance to the optical axis. Regarding a concave lens as shown in figure 4.4, the off-axis parts of the lens need to induce a larger deflection than the inner parts. However, the deflection strength of these parts typically deviates from the ideal value. If the lens is considered to be subdivided in several circular zones with different radial distance to the optical axis, each lensing zone has its own focal point. In this way, every extended light or electron beam experiences imaging errors during the optical process, which eventually affect the quality of the image. For example, the images (1 to 3) in figure 4.4 shows surrounding rings or are blurring depending on the image distance. Consequently, off-axis beams experience a stronger deflection so that distortions occur in the case of non-circular sources. This aberration occurs irrespective of whether the initial light or particle beam is parallel to the optical axis or is emerged from a point source. In general, beams emitted from point sources present stronger problems with spherical aberration. In the electron optical systems of this work only parallel electron beams are used for the imaging process. The impact of spherical aberrations can be reduced by adjusting the lenses in order to homogenise the deflection strength.

Chromatic aberrations occur, if the lensing properties of an optical elements depend on the wavelength of the light beams (and therefore the colour) as it is for the refractive index n_λ. As a result, lenses fail to focus light beams with different

colour to the same focal point. In the case of electron optical systems, the kinetic energy of the electrons is equivalent to the light wavelength and the initial energy spectrum determines the magnitude of the chromatic aberrations. Considering an electrostatic lens, electrons with a larger kinetic energy are deflected under a smaller angle and hence converge at a different focal point as slow electrons.[4] The only way to reduce the chromatic aberration is to narrow the initial kinetic energy spectrum. In the case of electron optical systems including an acceleration part, this can be achieved by a careful adjustment of the potential plates and grids of this part to establish very homogeneous acceleration fields. The electron optical system simulated in this work contains such an acceleration part which makes homogeneous acceleration fields being an important task (see section 4.4).

4.1.4. Electrostatic Lens Types used in this Work

As mentioned above, multiple-element lenses allow a better control and fine-tuning of the lensing potentials and hence a better regulation of the imaging process. Common electron lens designs typically consist of three electrodes, whereby the potential of the middle electrode is different from the other two potentials. Figure 4.5 shows four designs of such lenses. The triple aperture lens (a) was already mentioned as well as the cylindrical immersion lens (b) which is shown here in an alternative design including a third cylinder. Lens designs (c) and (d) are supposed to cause smaller aberration due to the more suitable design considering electron imaging (see page 65 in [34]). Especially design (d) presents some similarity to lens type (f) in figure 4.2 which is supposed to provide a better imaging quality than other lens types in that figure.

In this work, two electron lens designs were implemented in the simulation: The triple aperture lens (a) and the so-called hyperbolic lens (d). The first one is realised by three aperture plates which are positioned with the same distance to each other. Different inner diameters of the middle plate and the outer plates are examined as well as different configurations of the three lensing potentials. The middle potential is always strongly positive and the other two potentials are strongly negative (but not necessarily identical as shown in figure 4.5). The hyperbolic lens is realised by two hollow cone electrodes enclosing a torus electrode in the middle. Different smaller outer cone diameters and the larger inner ones are examined as well as the major and minor diameter of the torus and of course the potentials.

The shape of the electric field of both simulated lens designs is quite similar. In both cases, the middle electrode has a positive potential whereas the outer

[4] All electrons with different kinetic energy experience the same deflection force as long as they both crossed the lensing fields at the same distance to the optical axis. However, the deflection angle varies with the dominance of the initial longitudinal velocity component.

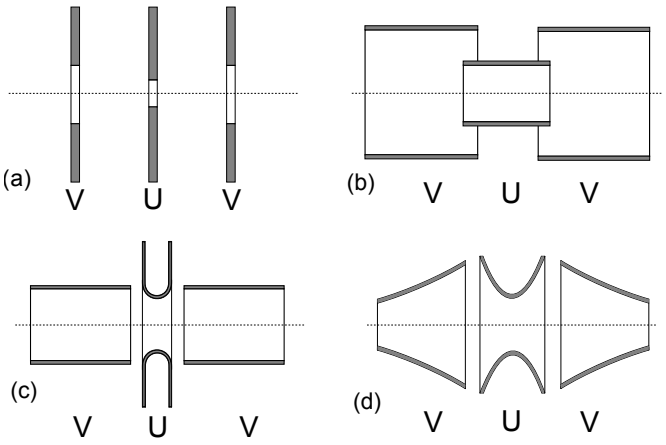

Figure 4.5: This drawing shows a sideview of four lens designs consisting of three electrostatic electrodes with different potentials. Designs (a) and (d) were examined in the simulations of this work. This figure is redrawn from [34], fig. 14.3.

electrodes are on negative potential. The electric field of the middle lens causes the field lines to be bulged out towards or right through the openings of the outer electrodes. This effect is shown in figure 4.6. The lens geometry combines the triple aperture lens design and that of the hyperbolic lens with a larger middle electrode and a cone like shape of the outer ones. As long as the three electrodes are parallel to each other the equipotential lines are highly compressed. At the location of the outer openings, the field lines establish a potential at the outside of the lens which is shown by the potential bulged at each side. The saddle point of the lensing potential is located exactly in the middle of the lensing system – as long as the outer potentials are identical. Electrons entering the lensing system experience a deflection caused by the electrostatic force which acts perpendicularly to the equipotential lines. In this figure, the lines left from the middle lens present a concave shape of the electric field and the electrostatic force causes the electron beam to be focused towards the optical axis. The field right of the middle lens shows a convex shape and such a de-focussing impact which, however, is less strong than the left field due to the smaller diameter of the electron beam at the level of the convex field.[5] In summary, the figure shows a collective lens which can be used to focus particle beams emitted by a random source that should be imaged in the electron optical system.

[5]The deflection strength depends on the distance to the optical axis so that off-axis rays or trajectories experience a stronger focussing impact than if they are close to the axis.

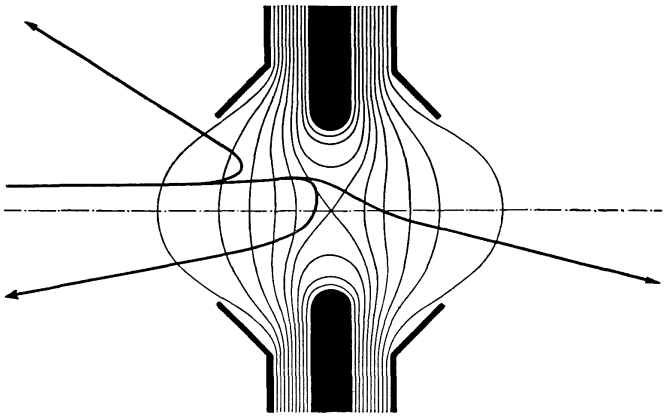

Figure 4.6: This figure shows a triple electrode lens design somewhere between a triple aperture lens and a hyperbolic lens. The arrangement of the equipotential lines of both lens types are quite comparable so that this scheme provides a closer look on the effective lensing potential of both types. This figure is taken from [36].

4.2. COMSOL Multiphysics

The simulation plots and results presented in this chapter have been performed with COMSOL Multiphysics – more precisely versions 4.3b and 4.4.[6] COMSOL is programmed to solve complex problems via a multifunctional step by step model as well as study builder and is used for a wide range of scientific application areas.

COMSOL provides an powerful, interactive graphic user interface to create many different kinds of physical models. Depending on the specific challenge, COMSOL offers several physical environments (so-called modules) like heat transfer, fluid dynamics or electrochemestry for a wide range of different models. All of these environments are equipped with the required theoretical, physical and mathematical background as well as essential constants and characteristic properties. One strength of COMSOL is the possibility to couple several physical environments within one model and solve them simultaneously so that one environment is able to refer to the results of another to simulate complex physical phenomena (*Multiphysics*). For the simulations of this work, the electrostatics (es) module was used together with the charged particle tracing (cpt) module. The es-module can be used to calculate macroscopic electrostatic field distributions for a given set of input potentials; the cpt-module then determines the trajectories of a given particle based on the solution of the es-module.

4.2.1. Setup of COMSOL Models

In order to set up a COMSOL model the following steps have to be carried out. At first, the geometry of the model has to be created. COMSOL provides basic

[6] Before 2005, the program was called FEMLAB. This name still appears in some publications about COMSOL-simulations from time to time.

geometric shapes like cubes, cones and spheres but also less primitive shapes like polygons and parametric curves. Each shape can be positioned in a three dimensional cartesian space. The individual objects are also referred to as domains within the simulation. Afterwards, materials properties are allocated to the single domains. The materials are described by a set of characteristic constants and properties which are required to solve the equations set up by the corresponding implemented physical environment. The next step is to define initial values considering the implemented physical environment. In the case of the es-module, this means to allocate potential values to the geometry domains acting as electric field sources. In the case of the cpt-study, a particle inlet has to be defined. As last, the meshing properties are set. Meshes are required for the finite element method, which is used by COMSOL to calculate the simulations. The mesh subdivides the domains in small elements that are calculated individually and the accuracy and the resolution of the solution depend on the maximum mesh size. COMSOL allows to allocate an individual maximum and minimum element size for each domain. Especially such domains that enclose the interesting physics can be meshed with much higher resolution to obtain more accurate solutions.

As soon as the model is completed, the simulation commands have to be set. The most important definition hereby is the study type. It is possible to implement more than one study step as it is possible to implement more than one physical environment. Consequently, several environments can be coupled which means to create dependencies between the solving processes of the corresponding study steps. In doing so, the solution of one study step can be linked to the solution of another step or even be used as initial parameter set. For example, the simulation of particle trajectories in an electrostatic field requires a stationary es-study to calculate the electric potential distribution in the simulated volume with respect to the initial potential values. Afterwards, the particle trajectories are computed in a time-dependent study step. To ensure the correct simulation of the particles based on the given external potentials, the initial values of the cpt-study are linked to the solution of the preceding es-study.

COMSOL provides a wide range of different possibilities to plot data. For es-studies, the electrostatic potential can be plotted in a 2D-plot groups by defining specific cut planes in the simulated volume. Such plots are referred to as surface plots in this work. In contrast, particle trajectories are presented in 3D-plot groups. More details and application possibilities of COMSOL can be found on the COMSOL-Webpage: `http://www.comsol.com/`.[7]

[7] Check also the short introduction to COMSOL: `http://www.comsol.com/shared/downloads/IntroductionToCOMSOLMultiphysics.pdf`.

4.2.2. Finite Element Method

The technique used by COMSOL for the solving process of the simulated models is the finite element method (FEM). Generally, FEMs are used as a powerful numerical method to solve a large set of partial differential equations. Once the whole geometry is created, COMSOL generates meshes of the individual domains. By doing so, every domain is divided into small subparts, which are referred to as *finite elements* at this point. The single elements are not infinitely small, which is also the origin of the name *FEM*. However, this procedure implies a certain granularity of the final solution.

To perform a certain study, all finite elements are equipped with several characteristic properties and parameters as well as a bunch of differential equations. These equations derive from the the specific physical laws given by the implemented physical environment and are used to calculate the effect of an external influence on a given element and its reaction to that very effect as well as its influence on neighboured elements. In short, for each finite element, the simulation calculates external influence, internal response and the resulting impact on the next element. The initial source of the external effect are physical variables like electric potentials, which are set in the model builder.

For the evaluation of the response of the single finite elements, each element is equipped with so-called shape functions variables and several ansatz functions.[8] Neighbouring elements are described by boundary conditions and transmission equations of a given effect. The variables and their derivatives as well as the ansatz functions are inserted into the differential equations to describe the general response of a finite element. Afterwards, the solution are calculated as numerical approach based on the initial set of parameters describing the external influence. Finally, the differential and transmission equations are integrated over the entire simulated area to couple the individual elements.

A very important quantity is the number of degrees of freedom f, which is specified by the physical environment. This number determines the size of the system of equations. Such systems are typically rather large and iterative methods have to be used to solve the equation system. The iterator improves an initial solution step by step until a certain degree of accuracy for the numerical approach is achieved.[9] Finally, the simulation is done and the results are written in the

[8] Shape variables are related to both shape functions and the degrees of freedom of a given finite elements. Shape functions are Lagrangian shape functions, which are the essential mechanism in FEMs.

[9] Depending on the degree of accuracy, the degrees of freedom and the mesh size, cluster computing with large RAM is necessary. With the cluster node, COMSOL provides an architecture to deal with such simulations.

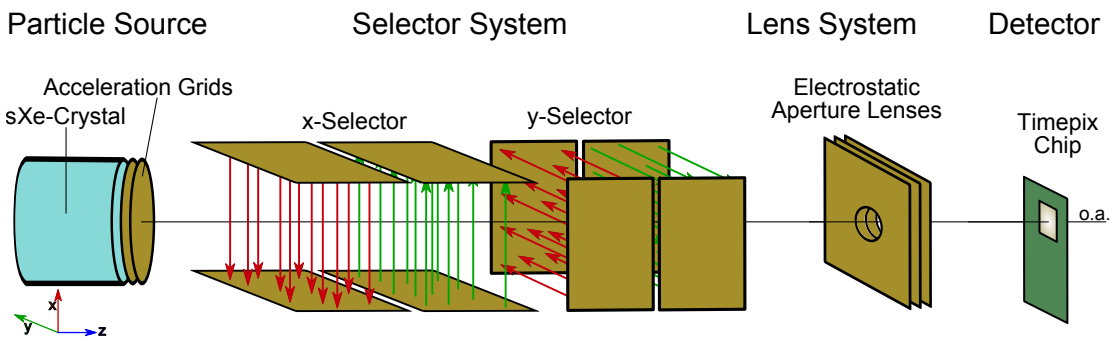

Figure 4.7.: This overview of the simulated setup illustrates the four main parts of the simulation: At first the solid xenon crystal as sensor material, the selector system for the deflection of particle beams to the optical axis (o.a.), the lensing system for the focussing of the particles and the detector eventually recording the incoming signal.

corresponding solvers or the parameter sweep defines a new set of initial variables and the whole process starts all over again.

4.3. Overview of the Simulated Setup

This section presents an overview of the setup that was simulated within the scope of this thesis. This includes the entire electron optical system as explained in the following, however not the excitation, drift and emission process of secondaries in the RGS or the detection process of the Timepix detector. As explained in section 3.1, a lensing system could be used to focus and enlarge a secondary electron signature of an interaction in the sensor material in order to improve the spatial resolution. However, the typical dimensions of the sensor required for $\beta\beta0\nu$-studies are rather large compared to the length of the Timepix signal chip. To cover a larger RGS-sensor surface compared to the Timepix sensor layer area, a selector system can be applied. Figure 4.7 shows a scheme of the main parts of the simulation setup to gain an overview of the electron optical system.

On the left, the solid xenon crystal acts as a particle source. As explained in chapter 3, fast particle produce secondary electrons inside the crystal which can be extracted by an external electric field in z-direction. The electrons are drifted to the crystal surface, extracted and accelerated by potential grids. The grids ensure a proper field configuration to accelerate the electrons in axial direction parallel to the optical axis (o.a.). Typical kinetic energies after the acceleration are about $6 - 8\,\mathrm{keV}$.

The following part is the selector system, which consists of several electron mirror pairs. The electrostatic potential distribution generated by the mirror pairs is specified to bend the particle beam onto the optical axis. Since the particles are emitted from a two dimensional plane, two sub-selector systems are required to compensate the distance in both x- and y-direction between the particle interaction point and the optical axis. In the scheme, both x- and y-selector consist of two plate electrode pairs. The first plate pair deflects the electron beam towards the optical axis whereas the second plate pair re-compensates any transversal velocity component of the electrons and eventually deflects the particle beam onto the axis. The voltages of both plate pairs have to be inverted as indicated by the electric field lines in the scheme. The x-selector has to fulfil two tasks: First, the particle beam has to lie in the yz-plane after passing the selector and secondly, the particles must not have any velocity component in x-direction. Speaking in terms of degrees of freedom: To accomplish these two tasks, at least two plate pairs are required for each selector. In the final simulation, the whole selector will consist of eight plate pairs.

Assuming that the selector system works well, the particle beam is on the same line as the optical axis after leaving the y-selector. In this case the electron lens will be able to focus the particle beam symmetrically. The simulations in this work mainly use three-electrode lensing systems as aperture lenses and hyperbolic lenses. The field configurations and functionality of such lenses are explained in section 4.1. In section 2.1 it is stated that typical electron tracks of the $\beta\beta0\nu$-decay have a length of about 2 mm. Therefore, the 2D-projection of a $\beta\beta0\nu$-track in the sensitive volume onto the crystal surface was assumed to be about 2 mm × 2 mm in the simulation and the dimension of the electron beam was set to the same value. The diameter of the holes of the aperture lenses are about twice that size. The negative potential of the first lens electrode should not exceed the electron energy (because in this case it would act as an electron mirror).

At last, the Timepix detector is used to detect the electron signal. As explained in section 3.3, the surface of the ASIC is 14 mm × 14 mm. As a result, the lensing system may magnify the electron beam up to seven times. The energy threshold for the detection of single electrons is about 3.5 keV and the electron energy is supposed be at least about 6 keV. This should cause no big challenge for the acceleration grids.

In figure 4.8 the setup geometry can be seen as it is created in COMSOL. The four main parts are indicated whereas additional features are explained in the following section. The geometry components are embedded in a long cylinder, which is necessary since the FEM only solves elements allocated to a specific material as physical environment. Domains without material are simply ignored during the solving process. To avoid such errors, the whole setup is located inside

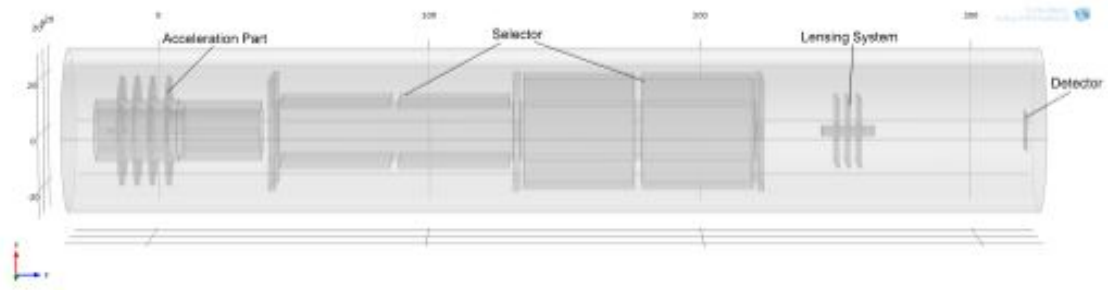

Figure 4.8.: A snapshot image of the simulated setup in COMSOL. Again, the four main parts are illustrated. The dimension of the grid tics is mm.

a surrounding cylinder that is specified as air since the material properties of air considering es- and cpt-studies are very equal to the values of vacuum.[10] Hence, the potential distribution of the electron optical components in the vacuum is simulated in an air environment. This domain can be meshed and solved just like all other domains.

To avoid long computing times the mesh size of the air is rather coarse. Additional smaller air domains with a much finer mesh are created around the particle beam to provide a proper simulation of the interesting processes in electron optical system despite the general coarseness of the air mesh size. Such domains will be explained in the following section. Typical upper limits for the mesh size were about 12 mm for the geometry details and the surrounding cylinder and 8 mm for the better resolved domains around the optical axis. Such upper limits create quite satisfying simulation results. Several high-resolution simulations are presented in section 4.5 with an upper limit of about 2 mm close to the optical axis. In all cases, the lower mesh size limit were about 0.05 mm.

4.4. Simulation of the Optical Components

This section takes a closer look on the basic features of the electron optical components as well as the whole simulation setup. As explained above the setup consists of four main parts: The acceleration part, the selector system, the electrostatic lens and the detector.

[10] Actually, the only important value is the relative permittivity. In COMSOL its value for air is $\epsilon_r = 1$ as it is for vacuum. One can argue that the density is of importance for the calculation of particle trajectories. However, the cpt-study does not consider the stopping power of the single domains so that the physical difference between air and vacuum has no influence in the simulation.

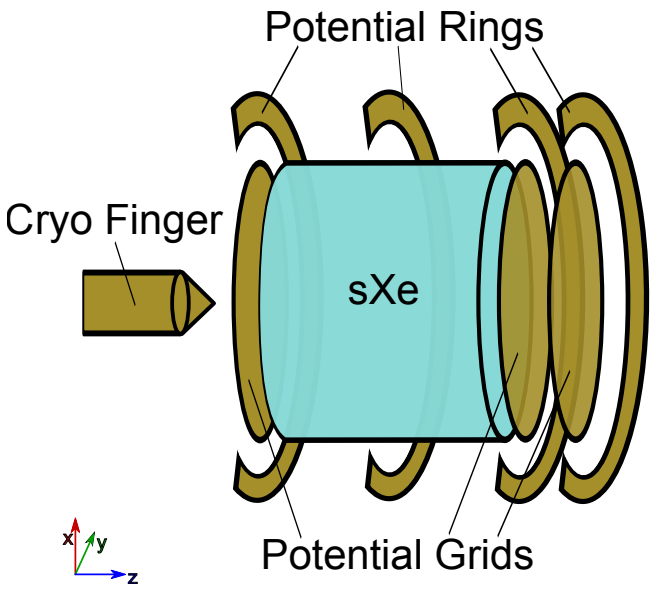

Figure 4.9: This scheme of the acceleration part illustrates the three grids for the drift and the acceleration field, the potential rings to parallelise the field lines at the edge of the crystal and the cooling finger at the bottom of the crystal.

4.4.1. Particle Inlet and Acceleration Part

The acceleration part has to manage several tasks: The generation of the drift field inside the xenon crystal, the acceleration of the particles after they surmount the crystal surface, the proper direction of this acceleration since the particles need to be emitted perpendicularly, and lastly the cooling of the whole crystal via a cooling finger. Additionally, the crystal is grown in an insulator cylinder followed by vacuum flanges that have to be considered.

Potential Rings and Grids

At first the potential shaping system is explained. In the simulation presented here, it consists of three grids and four potential rings. Figure 4.9 shows a scheme of these parts including the cooling finger.

The three grids generate two different electric fields: The drift field and the acceleration field. The first two grids enclose the xenon crystal in z-direction and generate the axial drift field. They are referred to as bottom grid and top grid. Secondary electrons in the sensitive volume are being drifted in positive z-direction due to this field. To minimise the influence of diffusion and scattering processes the drift velocity should be maximised. According to section 3.2 the drift velocity saturates at fields above $5 \times 10^3\,\mathrm{kV\,cm^{-1}}$. The height of the xenon crystal is set to 10 mm in the simulation and consequently, the potential difference between top and bottom grid is 5 kV.

After having surmounted the crystal surface and the top grid, the secondary electrons are accelerated by the second field. Their final kinetic energy needs to be about 7 keV as explained above. To create the acceleration field, a third grid is used, the so-called acceleration grid. The potential difference between the acceleration grid and the top grid is 7 kV whilst the distance between these two grids is set to about 5 mm.[11]

The three potential grids have to establish axial electric fields to drift and accelerate secondary electrons parallel to the optic axis. However, field scattering and distortion deform the electric field lines at the outer parts of the xenon crystal and above. Consequently, particle interaction events far away from the optic axis cannot be detected since the emitted secondary electrons are not accelerated perpendicularly to the crystal surface. This can be avoided by adding potential rings around the crystal to support the homogeneity of the drift and acceleration field.[12] Each grid has an associated potential ring surrounding the grid at the same z-level. The rings are supplied with the same potential level as the related grid so that the homogeneous zone of the electric fields is extended in radial direction. An additional grid is positioned between bottom and top grid to avoid minor scattering effects in the middle of the xenon crystal. This fourth ring is referred to as the middle ring.

The potentials of the bottom, top and acceleration grid/ring are −12 kV, −7 kV and 0 kV respectively.[13] Consequently, the drift field is high enough to saturate the electron drift velocity in solid xenon whereas the acceleration field speeds the electrons up to 7 keV (as required by the Timepix detector). The reason why the acceleration grid is set on earth potential is the following: The acceleration part is connected to the rest of the setup via vacuum flanges, which are on ground potential. If the acceleration grid has a different potential than 0 V, the electric field configuration generated by the grid and the following flange would not be homogeneous causing a deflection of the particle beam. This can be avoided if the acceleration grid is grounded as well. Further explanation of this choice of the potential zero-point are mentioned in the following subsections.

At last the cooling finger has to be considered. This copper finger is the top part of the cryogenic system, which has to be grounded as well. As a consequence, the

[11] The electric breakdown field in vacuum is roughly 1000 kV mm^{-1} – depending on the material and shape of the electrodes. However, the roughness of the electrode surface presents many tiny tips which establish much higher field strengths and the realistic breakdown field is rather several 10 kV mm^{-1}. The acceleration field of 1.4 kV mm^{-1} is within this limit.

[12] The easiest way would be to use larger potential grids. However, the crystal is grown inside of an growth chamber with cylindrical walls. Consequently, there is a small gap between the grids inside the chamber and the potential rings outside.

[13] The potential of the middle ring has to be 9.5 keV to maintain a homogeneous drift field strength inside of the crystal.

finger potential of 0 kV in direct neighbourhood to the −12 keV-potential of the bottom grid generate inhomogeneous electric fields. There are two possibilities to avoid this problem. The first one is to split the cooling finger in two parts with different voltage levels, which are connected thermally by thermally conductive foil. The cooling finger tip can then be set to the potential of the bottom grid. In turn, the grid is equipped with a hole at its centre, the cooling finger being positioned in its middle. Most of the following simulations have been done with a cooling tip at a potential of −12 kV. The other possibility is to place the cooling finger several millimetres below the bottom grid. Then, the xenon crystal would be grown from the cooling tip right through the bottom grid and so on. In this setup, the cooling finger stays on ground potential. A simulation of this setup is shown later.

Other Features of the Acceleration Part

Figure 4.10 shows a snapshot of the actual simulation geometry of the acceleration part in COMSOL. Note that only the electron optical components are simulated and not the drift end emission process of secondary electrons in the sensitive volume. All parts specified as copper in the model builder are highlighted in blue (mainly all parts mentioned above). Additionally, the xenon crystal is shown in turquoise. As explained above, the crystal needs to be grown in a special chamber mainly consisting of an insulator tube (PTFE is chosen here).[14] The inner diameter of this tube is 20 mm and the thickness is 1.5 mm. A steel flange with a thickness of 1 mm is connected to the PTFE tube to provide an adapter to the following vacuum system. The inner and the outer radius of the potential rings is 12 mm and 20 mm respectively. Their thickness is set to 1 mm. The potential grids are approximated in COMSOL as thin copper disks since the cpt-module generally ignores material properties as the stopping power. The bottom grid is hidden behind the bottom ring with a thickness of 1 mm as well. The top and acceleration grids (thickness 0.5 mm) can be seen rather faintly in the middle of their corresponding potential rings. The cooling finger has a diameter of 4 mm and the height of the tip is 2 mm.

As already mentioned, the xenon gas will start to freeze at the coldest spot which is the tip of the cooling finger. The finger is embedded in a PTFE flange for several reasons. At first the crystal growth chamber consists of PTFE in this simulation as mentioned above. Secondly, PTFE is a very good insulator with an electrical breakdown field strength between $33 - 80\,\mathrm{kV\,mm^{-1}}$.[15] This enables the setup of potential grids and rings as explained above without causing short-circuits.

[14] PTFE is the short term for *polytetrafluoroethylene* – better known under the brand name *teflon*. PTFE is a fluoropolymer and its chemical structure is similar to that of polyethylene if all hydrogen atoms are substituted by flour atoms.

[15] This value depends massively on the geometry of the electrodes. The breakdown field strength of PTFE can be higher than the realistic field strengths in vacuum as explained in footnote 11.

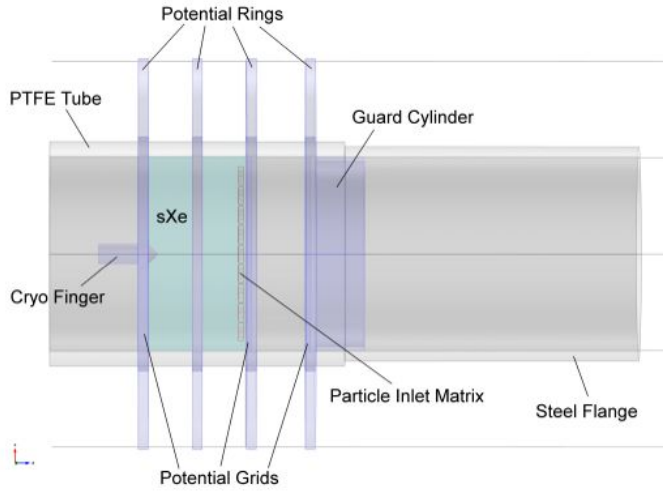

Figure 4.10: This snapshot image of the acceleration part in COMSOL presents the additional components of this part. Besides the grids, potential rings and the cooling finger, the PTFE tube, in which the crystal is being grown, is illustrated along with its flange connection to the rest of the setup.

Additionally, the electric fields of the potential rings introduced to support the field homogeneity are not shielded by the growth tube. Another reason is the bad heat conductivity of PTFE which is also why PTFE is chosen as growth chamber material. The cooling finger has to establish the coldest pole for the crystal growth. By embedding the finger in a PTFE flange, it is thermally insulated from the vacuum system and nearly the whole cooling power can be used for freezing xenon. The last reason is the excellent suitability of PTFE as working materials in vacuum due to its little gas emission and strong hydrophobic nature.

The PTFE flange is connected to the vacuum system via a stainless steel adapter that is also shown in figure 4.10. In the simulations, the adapter is approximated by a steel tube with the same inner diameter as the PTFE tube. The outer diameter will be much larger in the case of the final vacuum flanges but its actual size has no effect on the electric potential inside of the steel tube.[16] The potential of the adapter itself is 0 V since the vacuum components are grounded.

The last part to be explained here is the guard cylinder. This cylinder is a thin circular copper sheet between the acceleration grid and the steel flange. All these parts are on ground potential. Without the guard shield, the electric field from the other potential rings would pass through the gap between acceleration ring and steel flange causing disturbing field gradients in the area above the acceleration grid.

[16]The final setup of the vacuum components has not been finished up to the deadline of this work, so that this approximation of the adapter has to be sufficient.

Potential Cut Planes

Figure 4.11 shows a potential plot of the acceleration part with the mentioned potentials as initial values.[17] The plot presents the following features: At first, the the contours of the geometry in the zx-plane are illustrated in deep black. The four potential rings, the two tubes, the acceleration grid and the guard cylinder can be recognised easily. The units of the axes are set to mm. Secondly, the potential distribution is presented as a so-called surface colour plot, which indicates the potential by a rainbow colour scale (high negative voltages are blue; high positive voltages are red). At third, equipotential contour lines are drawn with a particular potential step. The scales on the right present the plotting range and the extreme values at the very top and bottom of the scale. In figure 4.11 the potential reaches from $-1.7 \times 10^4\,\mathrm{V}$ at the location of the bottom grid, bottom ring and cooling finger to $1.2 \times 10^4\,\mathrm{V}$ at the middle part of the electron lens which is discussed later. 0 V areas are shown in green. The unit of the colour scale is Volt.[18] The contour plot scale indicates the potential step of the equipotential lines which is 750 V. It spans from $-1.73 \times 10^4\,\mathrm{V}$ to 0 V to cover the whole potential range in the acceleration part.[19] The plot is produced from a simulation with a particle velocity of 12 keV so the potential difference of the acceleration field is 12 kV and the bottom voltage is −17 kV. Besides that, the figure shows several artefacts:

- Straight, parallel and equidistant contour lines between the bottom and top grid and the top and acceleration grid indicate a homogeneous drifting and acceleration field inside of the PTFE tube.
- The density of the contour lines shows that the acceleration field strength is larger due to the larger potential difference over a smaller distance of the grids compared to the drift field.
- The potential rings stabilises the homogeneity of the fields. Without the rings, the equipotential lines would bulge out at diameters comparable to that of the PTFE tube. This effect still can be seen due to the small bumps in the lines at the location of the PTFE tube.
- Some geometric borders appear in grey instead of black. This is because conductive parts as the potential rings (copper) and the steel flange represent

[17] A German expression has found its way to COMSOL here. *Elektrisches Potential* means *electric potential* in English.

[18] Consider the multiplication factor $\times 10^4$ at the top of colour and contour lines scale.

[19] The contour plot only shows multiples of 750 V. That explains why instead of the absolute minimum potential of $-1.7 \times 10^4\,\mathrm{V}$, the minimum here is $-1.65 \times 10^4\,\mathrm{V}$, which is 22 times 750 V.

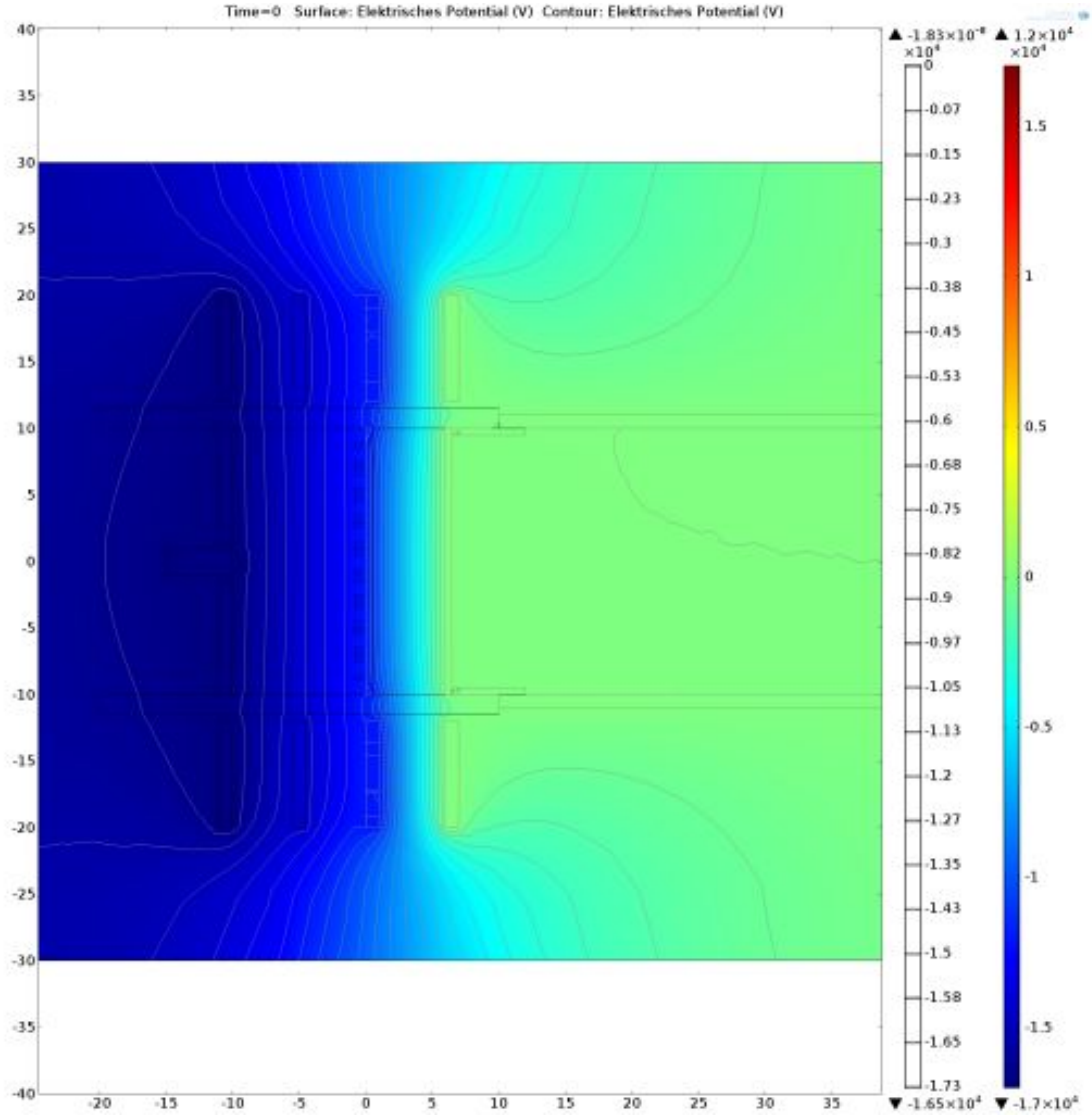

Figure 4.11.: This figure presents a plot of the potential distribution of the acceleration part. The cut plane evaluated here is a zx-plane without y-offset. The potential is shown as surface plot in a rainbow colour scale. Additionally, grey curves indicate the equipotential lines.

an own equipotential line. Their borders are replotted in grey, if their potential is the same as one of the contour lines.

- The potential lines originating from the negative potential rings bulge over the acceleration ring but the 0 V-area inside the steel tube is not penetrated. The propagation of the particles beyond the acceleration grid can be assumed to be parallel to the optic axis.

- Some equipotential lines show rough edges and unsmooth bends. In addition, a contour line is shown in the middle of the 0 V-area inside the steel flange where no potential gradients are expected. These artefacts are due to the meshing of the domains. The finite mesh size implies a certain coarseness to the simulation that is manifested in the smoothness of the plots. The structure inside of the top ring and the line at the top right corner of the PTFE tube is due to the same reason.

The following sections present various potential surface plots that show similar artefacts as listed above. The origin of the artefacts, however, is the same.

Particle Inlet Matrix

To include particles to the simulation, the cpt-module requires a boundary selection as particle origin or *particle inlet*. The initial values are chosen as follows: The particle properties (mass, charge) are those of electrons, the release time is 0 s so that the entire simulation starts with the particle inlet and the number of simulated particles is usually about 500.

The inlet also requires an initial kinetic energy. The cpt-module ignores material characteristics as drift velocities so that electrons in the xenon domain are not drifted but accelerated. This approach disagrees with the physical reality so that the simulation needs to be manipulated to approximate the realistic particle behaviour. The inlet boundary is located only several millimetres beneath the surface of the xenon crystal and the initial particle inlet energy is set to be the saturated drift velocity of electrons in solid xenon, which is $5.5 \times 10^5\,\mathrm{cm\,s^{-1}}$.[20]. Only the z-velocity is allocated with this value whereas all the other components are zero to emit the particles perpendicularly to the crystal surface. This is only an approximation to the physical emission process of secondary electrons from an insulator surface (compare to section 3.2); however, this approximation makes much sense for the simulation of the electron propagation. The particle inlet is located directly below

[20] As mentioned above, the drift velocity in solid xenon saturates at fields above $5\,\mathrm{kV\,cm^{-1}}$, which also is the strength of the drift field. The saturation value is taken from section 3.2. Several simulations are performed with an inlet velocity of $6.0 \times 10^5\,\mathrm{cm\,s^{-1}}$.

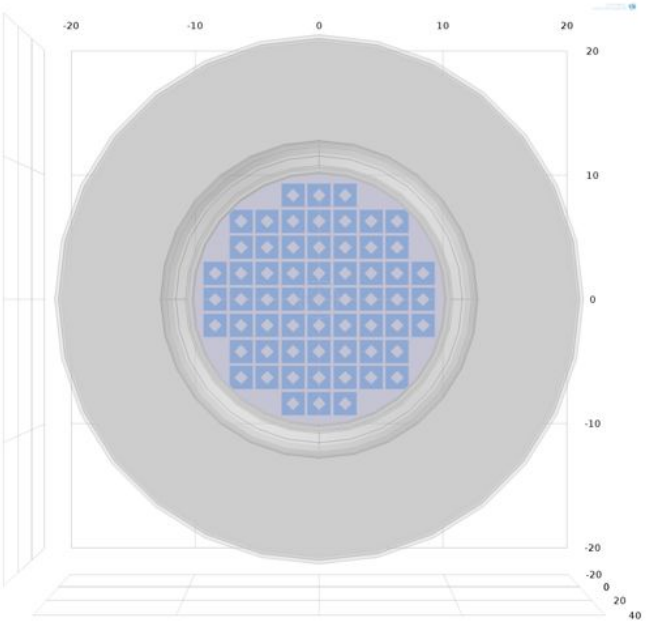

Figure 4.12: This figure shows a topview of the particle inlet matrix. All units are millimetres. One can an array of identical inlet shapes located on the circular surface of the xenon crystal. The shapes are highlighted in blue. The other circular structures represents the topview on the tubes and the potential rings.

the crystal surface so that the acceleration of the particles is done nearly entirely by the acceleration field as intended.

To establish a particle inlet in COMSOL, a geometry domain has to be allocated as inlet boundary. This domain should have a detailed shape to allow comparisons of the enlarged picture after focussing and the actual inlet shape to evaluate the aberrations of the electron optics. The shape should be approximately $2 \times 2\,\mathrm{mm}$ in size, since this is the expected interaction area of a $\beta\beta0\nu$-event. Furthermore, several shapes at different xy-locations have to be created to simulate and check the function of the selector under different optical deflection requirements. To meet all these demands, the particle inlet matrix shown in figure 4.12 is added to the model. It can also be seen from the side in figures 4.10 and 4.11 directly below the crystal surface.

The inlet matrix consists of several identical boundary shapes. The shapes are assembled in an array on the circular surface of the xenon crystal and are highlighted in figure 4.12.[21] The edge length of the squares is 1.9 mm to meet the estimated length of a $\beta\beta0\nu$-track. A smaller rotated square has been cut out of the middle of the big square to create some edges that can serve as reference for the image quality. The single shapes are assembled with a distance of 2 mm to each other and accordingly, the selector can be evaluated in increments of 2 mm.

[21] In COMSOL, an extrusion of the draft of the inlet matrix generates the actual inlet boundaries. The extrusion is done with respect to crystal surface. The material and meshing properties are the same as for the xenon crystal domain.

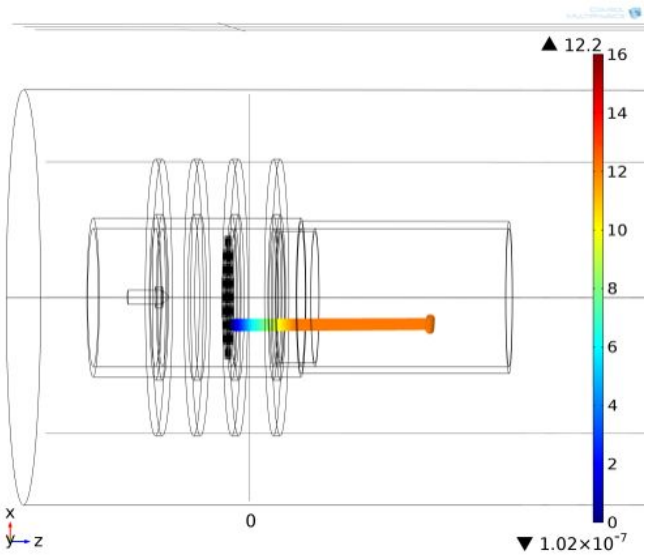

Figure 4.13: This figure presents a 3D-plot of the trajectories in the acceleration part. The evaluation time is 0.6 ns. The particles are emitted from the selected inlet boundary and accelerated in positive z-direction.

As soon as the inlet shapes are meshed, its boundaries are assigned as particle inlet in the cpt-node of COMSOL. Afterwards, the particle trajectories are calculated with respect to the solution of the es-study. The final 3D-plot of the trajectories is presented in figure 4.13 – based on the field distribution of figure 4.11. The trajectories are indicated by lines whereas the present location of the particles are represented by points. This location depends on the evaluation time of the particle movement, which can be set as one of the plotting parameters.[22] Both lines and points are coloured according to the particle energy at the specific location along the trajectory. The inlet velocity is $6 \times 10^5\,\mathrm{cm\,s^{-1}}$ or $1.02 \times 10^{-7}\,\mathrm{keV}$ and hence, this energy is indicated to be the minimum on the keV-colour scale. The particles here are accelerated up to 12.2 keV. The position of the centre of the inlet shape (and therefore the simulated location of the $0\nu\beta\beta$-event) with respect to the optical axis is $(x, y) = (-4, 0)\,\mathrm{mm}$. Consequently, this specific simulation can be used to examine the function of the x-Selector.

Besides the rhombic shape shown in figure 4.13 a second inlet shape was created to simulate the secondary electron distribution assumed to result from a $\beta\beta0\nu$-decay. This shape is presented on the left in figure 4.14. Based on MC-simulations of a particular $\beta\beta0\nu$-event in the sensor layer of a Timepix chip, the alternative inlet shape copies that pattern with the same binning steps. The whole shape consists of 10 times 8 tiles with a side length of 0.2 mm in order to reproduce the expected projected area of such a $\beta\beta0\nu$-event. The energy distribution per pixel is supposed

[22] This is why the cpt-study needs to be a time-dependent study. Arbitrary time steps can be set in COMSOL. The smaller these steps are, the smoother the trajectories can be plotted. This smoothness needs to be compensated by larger computing times.

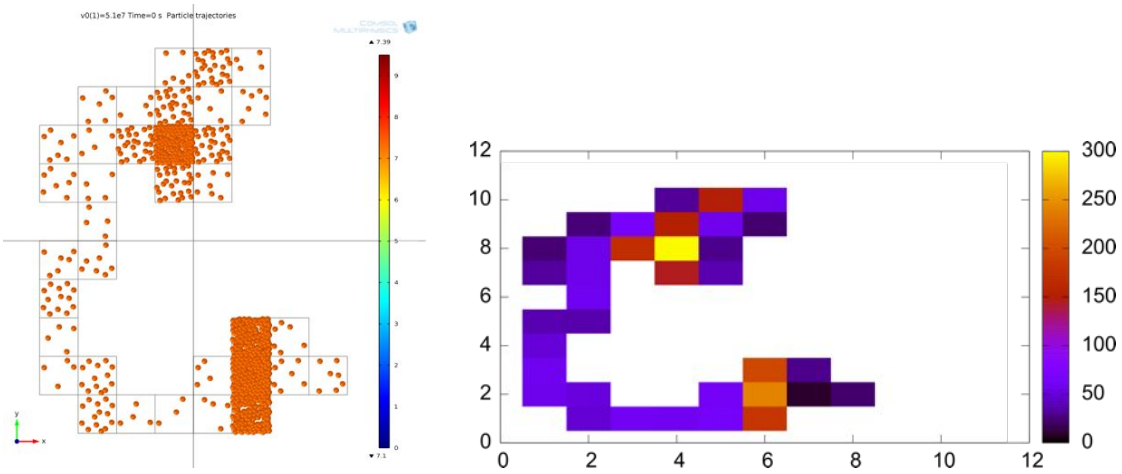

Figure 4.14.: Left: A topview trajectory plot representing the secondary electron distribution associated with a $\beta\beta0\nu$-event. The inlet shape is divided in several tiles that correspond to the pixel of a simulated event in a Timepix sensor layer (right, compare to figure 2.7).

to arise from a distribution of the number of secondary electrons, which all have the same kinetic energy. As a result, the different pixel intensities are reproduced by a different number of particles per inlet tile.

Figure 4.14 presents the simulated event in the Timepix on the right and the reproduction in COMSOL on the left.[23] The evaluation time of the plot is 0 s, so that the particles are shown as they are emitted from the inlet shape boundaries. The strongly populated tiles correspond to the energetic orange and yellow pixels in the MC-simulation whereas nearly empty tiles are referred to the low-energetic purple pixels. This inlet shape is an alternative to the shape above but requires more computing time due to the higher number of simulated particles that is necessary to present the different particle densities. Additionally, optimizations of the optical components are difficult due to the complexness of this inlet shape. Most of the simulations in this work are done with the rhombic inlet shape for this reason.

Simulation of a Bottom Grid

As mentioned above, there are two possibilities to locate the cooling finger in the acceleration part within the simulation geometry. The main challenge is the direct proximity to the bottom grid which has a high negative potential whereas the

[23] No electric field is implemented here since only the particle inlet pattern is of interest. The inlet velocity is already set to $5.1 \times 10^7\,\mathrm{m\,s^{-1}}$ or a little more than 7 keV in this simulation. Both values can be seen on the top or the energy colour scale respectively.

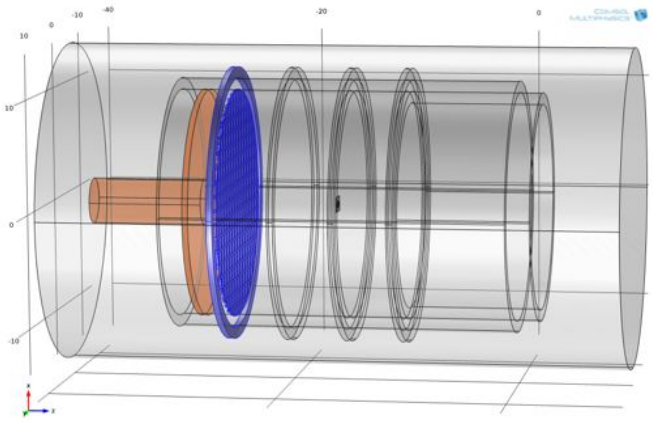

Figure 4.15: This geometry snapshot of the acceleration part shows a realistic bottom grid (blue) and the cooling finger right behind (copper). All other geometry details are similar to the previous setup. The displayed coordinates are given in mm. The distance between cooling tip disc and bottom grid is 2.3 mm.

cooling finger has to be grounded. Both parts have to be positioned at the bottom of the xenon crystal. One possibility is to place the cooling finger below the bottom grid so that the xenon crystal grows right through this grid. The concern with this plan is that the 0 V-potential of the cooling tip might affect the homogeneity of the drift field in the crystal on the other side of the bottom grid.

To examine this influence, a realistic grid was designed in COMSOL. Due to the numerous tiny boundaries and edges of a grid, the number of meshing domains is quite large so that the mesh size needs to be very fine over the whole grid. As a consequence, the calculation time increases massively with decreasing distance of the single fibres. This is also the reason why all grids in the simulations of this work are approximated by thin discs.

A snapshot of the adjusted acceleration part is presented in figure 4.15. The bottom grid is highlighted in blue and the cooling finger in orange. The finger ends in a disc that covers the whole diameter of the PTFE tube. The freeze-out of xenon is assumed to start at this disc so that the crystal grows right through the bottom grid. The snapshot also shows the middle, top and acceleration grid, the guard cylinder and a single particle inlet. The grid consists of multiple perpendicular fibres with a diameter of 0.2 mm and a grid gap of 1 mm. The distance between the surface of the cooling tip disc and the backside of the bottom grid is 2.3 mm. The potential of bottom and top grid is $-17\,\mathrm{kV}$ and $-12\,\mathrm{kV}$ respectively whereas the cooling finger is grounded.[24].

Figure 4.16 shows the corresponding 2D potential plot. The evaluation cut plane is a zx-plane with a y-offset of 0 mm. At the level of the bottom grid, the plot shows cuts through the horizontal fibres. Geometry borders are shown in deep black and equipotential lines are indicated by fine dark grey contours again whereas all copper parts are coloured in grey to gain a better overview. The homogeneous drift

[24]This gives an electric field of about $7.5\,\mathrm{kV\,mm^{-1}}$ between the tip surface and the bottom grid. This field strength lays within the limits explained in footnote 11

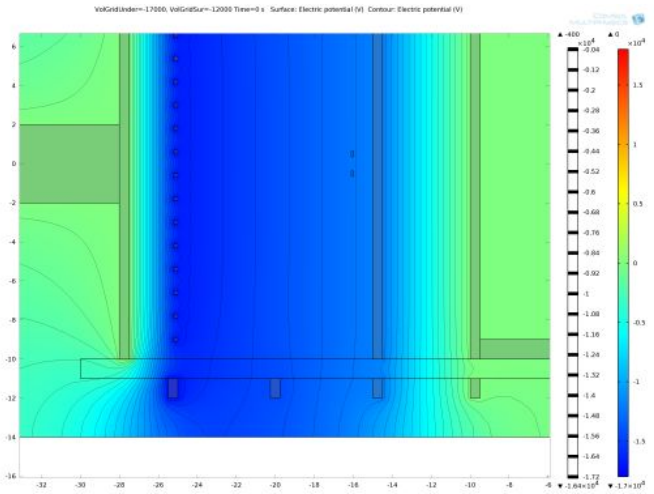

Figure 4.16: This figure presents the 2D potential surface plot of the acceleration part with an authentic bottom grid instead of a thin disc. The plot shows a zx cut plane. Copper parts are coloured in grey. The lowest equipotential line indicates a certain impact of the 0 V potential of the cooling tip on the area beyond the bottom grid at the grid gaps.

and acceleration fields can be seen once more as well as the strong field established between cooling tip disc and bottom grid. Green areas indicate 0 V potentials and the potential minimum is -1.7×10^4 V at the location of the bottom grid according to the colour scale.

The most significant aspect in figure 4.16 is the influence of the 0 V-potential of the cooling finger on the area beyond the bottom grid. The 16.4 kV-equipotential line shows a small leakage of the higher potential beneath the grid through its gaps. The penetration depth of this impact is estimated to be not higher than 0.5 mm. In this part of the sensitive volume secondary electrons from incident particle events cannot be drifted entirely parallel to the optic axis. As a result, there is no great loss in detector volume and basically, the application of grids as placement of equipotential planes is practicable.

On the other hand, the xenon crystal is followed by an extended electron optic so that even small aberrations and transversal velocity components of the electron beam caused by the potential grids might cause a significant impact on the imaging quality. Consequently, very fine grids with thin fibres and small gaps are necessary in reality. These grids should be able to limit the mentioned leakage of potential to a minimum albeit such simulation exceeds the limitations set by the available computing power.

Simulation Errors of Particles Crossing Potential Discs

In some simulations significant errors occurred in the energy distribution of particles after crossing domain boundaries. The problem first got manifested at the domain boundary between the acceleration area and the acceleration disc itself. For a better understanding of this artefact, a plot is presented in figure 4.17. It shows two xy-plots of the same simulation: In the left plot ($t = 0.2$ ns) the particles

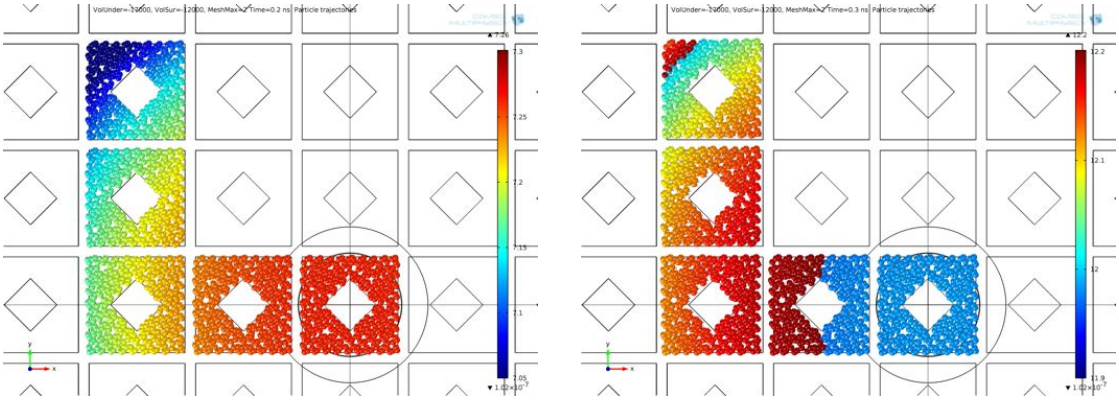

Figure 4.17.: This figure shows two topviews of the particle beams emitted from five different inlet boundaries. The left plot shows the particle beam during acceleration, the right plot after passing the acceleration grid. Clear edges in the particle energy distribution are visible indicating errors during the simulation process.

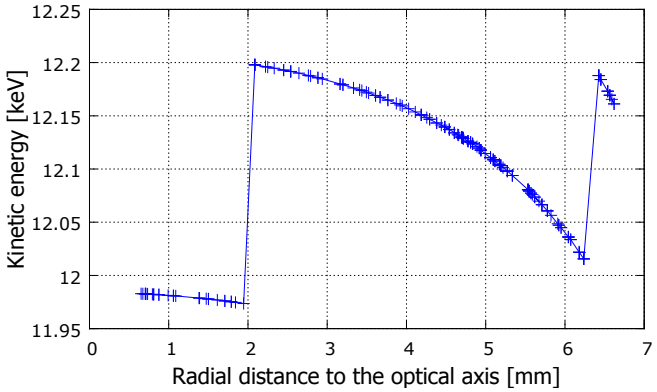

Figure 4.18: The kinetic energies of a selection of particles from fig 4.17 are plotted versus their radial distance to the optical axis. The plot shows obvious energy steps due to simulation errors.

are still located in the acceleration field whereas in the right one ($t = 0.3\,\mathrm{ns}$) the particles have already crossed the acceleration disc. The particles are accelerated to 12 keV.[25] Five different boundaries were selected as particle inlet. Note that both energy scales are different due to the uncompleted acceleration in the left plot.

After the particle transition through the acceleration disc, the energy distribution of the particles with increasing distance to the optical axis shows clear edges so that one part of the beam has significantly less energy than other parts. This is problematic for the function-testing of the electron optics since both deflection intensity of the selector as well as the focussing power of the electrostatic lens depends on the kinetic energy of the electron passing the selector fields.

[25] *VolUnder* is the potential of the bottom grid and *VolSur* the potential of the top grid. Consequently, the drift field potential remains 5 kV.

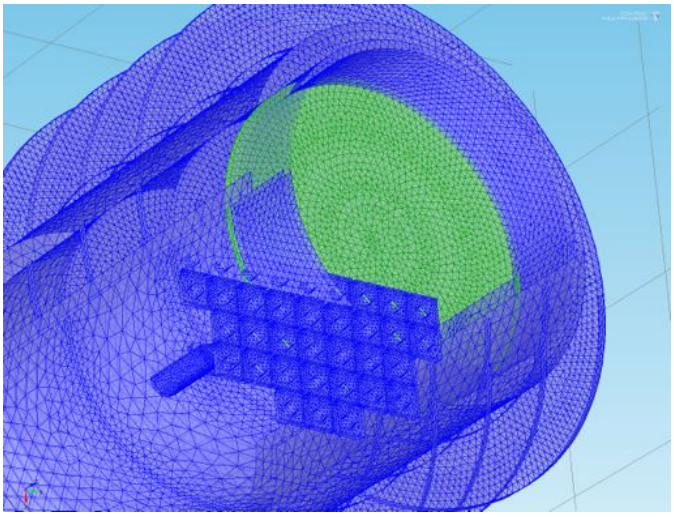

Figure 4.19: This plot shows a snapshot of the acceleration part after the meshing process. The acceleration disc is highlighted in green. The radial symmetric structure of the corresponding mesh is clearly visible.

The plot presented in figure 4.18 provides a better view on the problem. This plot is based on the right topview in figure 4.17. It shows the kinetic energy of a selection of particles versus their radial distance to the optical axis at $z = 0$. The diagram shows a radial dependency of the kinetic energy with the radial distance caused by small inhomogeneities in the radial acceleration field mainly due to different heights of the top grid and the top ring. More vital, however, are the two energy steps, which cause the edges shown in figure 4.17. The height of the steps is about 0.2 keV, which is large enough to cause bad imaging artefacts in the selector.

The reason for the observed edges lies in the finite element method used by COMSOL for its simulation process. Considering two neighboured domains with different mesh sizes, which meet at a particular shared boundary, the different meshes might cause mismatching structures. This in turn can result in discrepancies as soon as such boundaries are evaluated within a certain simulation study. Figure 4.19 presents the mesh of the acceleration disc (in green) in case of the particle trajectory evaluation shown above. The maximum mesh size is set to 2 mm in the vacuum around the disc. If this value is changed, the radial distance of the observed energy edges varies as well. As a consequence, this artefact can be attributed to the size of the mesh elements. Additionally, the figure shows that COMSOL creates radial symmetric mesh structures for radial symmetric objects such as the acceleration disc. Considering this, the circular shape of the energy edges in figure 4.17 is no big surprise.

Such energy steps can be avoided by reducing the maximum mesh size. For example, the edges disappeared in the simulation as soon as the mesh sizes were set to values below 2 mm. However, the radial dependency of the kinetic energy between two energy steps is not related to the mesh size and still has to be considered. Besides that, long computing times have to be accepted to cope with the fine mesh

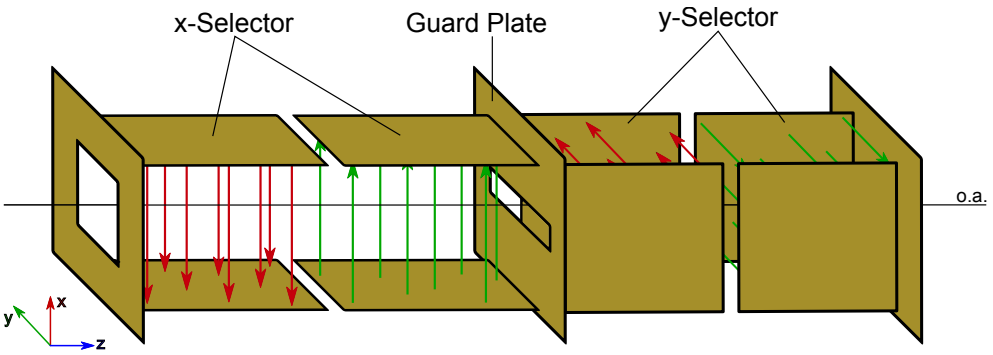

Figure 4.20.: This figure shows a scheme of the selector system. Both sub-selectors consist of two potential plate pairs with opposing electric fields. The sub selectors are separated from each other and from the rest of the setup by three grounded guard plates. Rectangular holes are cut in the guard plates to enable the movement of the particles through the selector.

size in the acceleration part. Therefore and due to the inhomogeneity of the kinetic energy within a certain particle beam, the adjustment of the selector system was done without particle acceleration.

4.4.2. Selector

The main task of the selector system is the deflection of the particle beam onto the optical axis. The particle beam is emitted from the particle inlet matrix so that the deflection degree of the selector has to be adjusted to different radial distances between particle beam and optical axis. This is realised via different electric field strengths so that the main challenge is the correct choice of the field strengths to achieve the right deflection of the beam. Additionally, optical imaging errors caused by the selector fields have to be considered.

Design and Calculations

The particles are emitted from the (two-dimensional) surface of the xenon crystal, which is approximated by the particle inlet matrix. To compensate the x- and the y-coordinate of the inlet position, the selector system is divided into a x-selector and a y-selector. Each sub-selector has to adjust the transversal position x_t as well as the transversal velocity $\dot{x}_t$ of the particles.[26] Both variables have to be zero after the particle passage through the selector field, which means that two potential plate pairs are necessary for each sub-selector.

[26]The corresponding terms adjusted in the y-selector are referred to as y_t and $\dot{y}_t$.

Figure 4.20 presents a scheme of the selector part. Both x- and y-selector consist of two parallel potential plate pairs. The distance between the pairs is 20 mm – as long as the diameter of the xenon surface so that particle beams emitted from any inlet boundary are able to enter the selector. The potential plate pairs of each sub-selector generate opposing electric fields. The first sub-selector field is responsible to accelerate the particles towards the optic axis whereas the second field compensates the transversal velocity until the particle beam hits the optical axis.

Both sub-selectors are separated from each other and from the rest of the setup by three grounded guard plates. These plates are supposed to prevent a negative impact of the individual electric fields of the selector plates on each other but also any influence of the acceleration and lensing fields on the selector functionality and vice versa. The guard plates are equipped with rectangular windows to allow particles to move through the selector system. The particle windows should be as small as possible to minimise any field leakage. The edge length of the first window is 20 mm – as large as the diameter of the xenon crystal. The height of the second window can be somewhat smaller since it can be assumed that the x-selector managed to set x_t to zero. In this simulation, 4 mm has been chosen as vertical edge length, which is twice the size of the particle beam, based on the supposed length of a $\beta\beta0\nu$-event of 2 mm. The width of the second window has to remain 20 mm. The dimension of the third particle window is 4×4 mm.

Due to the opposing electric fields, every two neighbouring plates are on a potential with different signs. Typical voltages applied on selector parts are not larger than about 3000 V. Considering the electric field breakdown strength in vacuum, 0.3 mm should be a sufficient distance between two plate pairs to prevent breakdowns.[27] However, due to the increased possibility of a field breakdown at the plate corners, the distance between two plate pairs is set to 3 mm and the distance between each potential plate and guard plate to 1.5 mm.

Adapted Particle Inlet

As mentioned above, the acceleration was turned off for the test run of the selector to entirely control the particle inlet properties and to minimise the complexity of the simulated geometry. The kinetic energy of the electrons at this point is set to 12 keV (about $6.4 \times 10^7\,\mathrm{m\,s^{-1}}$). Due to this adjustment the beam quality is ideal (and especially not as bad as in figure 4.17). However, a perfect beam is inappropriate to check the function of the selector. For example, some adjustments of the selector geometry or the applied potentials might not cause an observable contribution to the imaging process since the beam already has a quality which

[27] see footnote 11

cannot be expected in the actual experiment. As a consequence, the selector properties cannot be adapted in the way that would be necessary in reality. In the following simulations, a certain artificial reduction of the beam quality has to be added to examine the selector under non-perfect circumstances.

To realise such an adapted particle inlet, the inlet velocity v_0 of the particles is extended by two additional terms. The first term introduces a radial drop of the acceleration field with increasing radial distance to the optical axis as observed in figure 4.17. The drop is approximated by a linear radial term:

$$- v_0 \cdot \rho_r \cdot \sqrt{x^2 + y^2} \quad . \tag{4.4}$$

The weighting factor ρ_r of this first, radial term is set to 0.3 % relative to v_0. The second term adds or subtracts an arbitrary fraction of v_0 to the inlet velocity. For such tasks, COMSOL offers the possibility to define a two-dimensional random function $rn(x, y)$, which provides arbitrary values between 1 and -1 for each individual location on the xy-plane. This random offset introduces a certain granularity in the energy distribution. It is included by

$$+ v_0 \cdot \rho_r \cdot rn(x, y) \tag{4.5}$$

with a weighting factor of $\rho_r = 0.1\,\%$. Both terms are added to the inlet velocity v_0 defined in the cpt-study properties. The simulation results are presented in figure 4.21. The same inlet boundaries and the same evaluation time is selected as above. The inlet velocity is $v_0 = 6.6 \times 10^7\,\mathrm{m\,s^{-1}}$. The radial decrease of the kinetic energy is visible as well as the energy granularity caused by the arbitrary offsets due to the random-function. The energy range spans about 0.5 keV which is comparable to the range between the (0,0) and (-4,-4) inlet boundaries if acceleration takes place. This adapted particle inlet reflects reality in a better way than an ideal beam, which supports the improvement of the selector properties. All of the following simulations without acceleration part are done with this kind of particle inlet properties.

Calculation of the Potentials

In order to calculate the proper selector potentials with respect to the initial inlet coordinates, the selector is approximated by two plate capacitors in a row. The following equations describe the particle movement in such a system when scattered and inhomogeneous electric fields are neglected.

Figure 4.22 shows a scheme of the x-selector. The plate pairs are indicated by black thick lines. The space between the single plates is d, the gap between two plate pairs is K, and the length of the plates is L. The orange particle beam enters the selector with $x_t = x_0 \neq 0$ and $\dot{x}_t = 0$ and leaves with $x_t = x_\infty = 0$ and

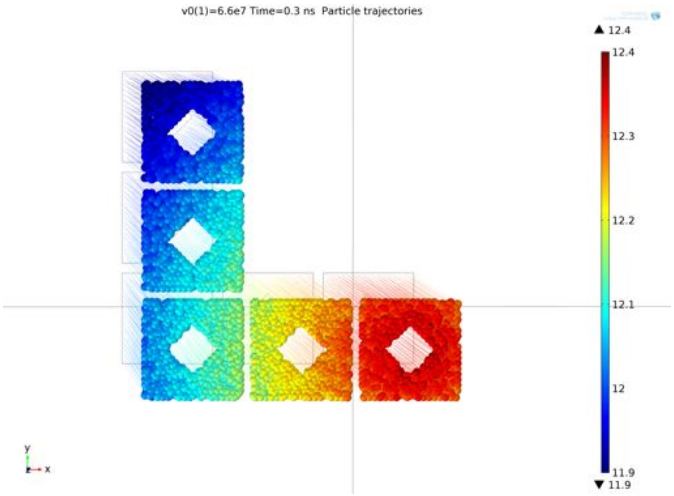

Figure 4.21: This topview shows the adapted particle inlet, which can be used for the voltage adjustments and geometry tests in the selector. The linear decrease in energy is visible as well as the granularity caused by the random offsets to the inlet velocity.

$\dot{x}_t = 0$. The particle velocity in z-direction is $v_z = v_0$ throughout the whole selector system. The trajectory is subdivided in five parts: Before entering the selector, the deflection of the first electric field (U_1, field lines are yellow), the interspace (K) between the plate pairs, the deflection of the second plate pair and after leaving the selector.

Before entering the selector the particle trajectory follows a horizontal line with an offset of x_0:

$$f_1(z) = x_0 \quad . \tag{4.6}$$

The electric field of the first plate pair can be interpreted as regular plate capacitor with voltage U_1, distance d and plate length L. The particles are accelerated in direction towards the optical axis. The problem can be described with a simple acceleration equation:

$$f_2(z) = x_0 + \frac{1}{2}\, a_1\, t(z)^2 \quad .$$

The acceleration a_1 only takes place between the plate pairs and any influence of scattered fields are neglected. As a result, a_1 doesn't depend on z in the area between the plate pairs. The acceleration is caused by electrostatic forces $F = qE = qU/d$ which gives:

$$f_2(z) = x_0 + \frac{1}{2}\,\frac{F_1}{m_e}\, t^2 = x_0 + \frac{1}{2}\,\frac{q_e\, U_1}{m_e\, d}\,\left(\frac{z}{v_0}\right)^2 \quad , \tag{4.7}$$

where the propagation time t in the selector is transposed with z/v_z.

In the third part the particles cross the area between the plate pairs where no electric fields are supposed. The particles are not accelerated but propagate linearly with the transversal velocity $v_x(L)$ gained in the first plate pair. The particle

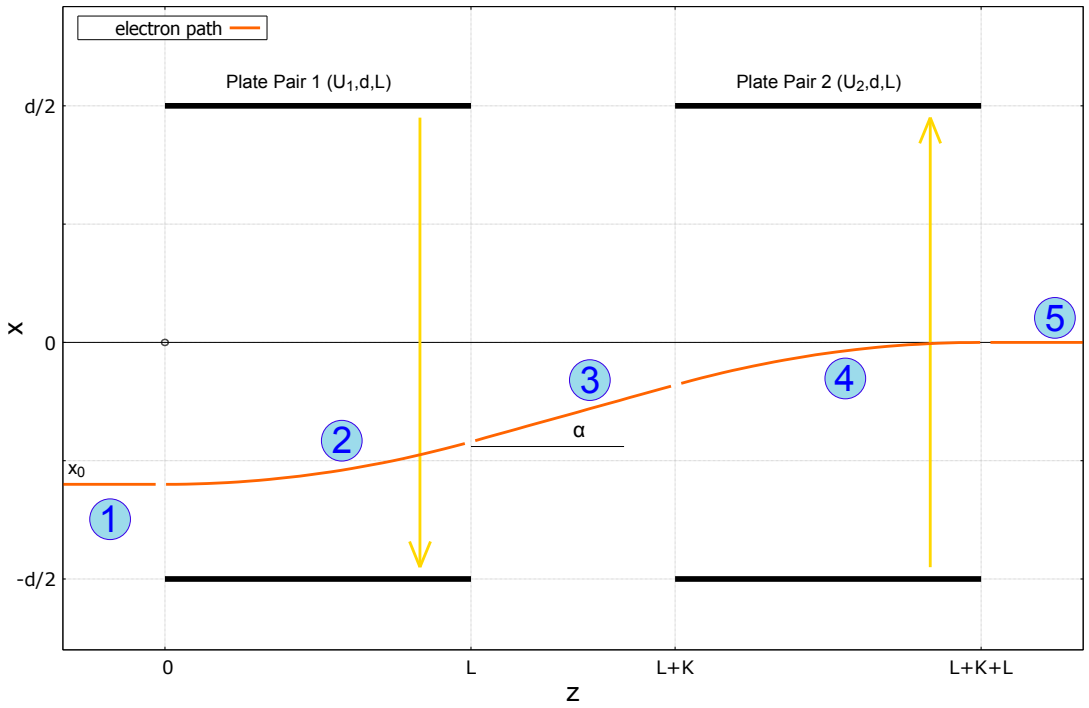

Figure 4.22.: This plot shows a particle trajectory in an ideal plate capacitor with two potential plate pairs (black) with length L, gap d and distance K. The particle path (orange) is calculated from the electric fields strengths (yellow). The path is sub-divided in five different parts.

trajectory and the optical axis span an angle α, which can be written as:

$$\tan\alpha = \frac{v_x(L)}{v_0} = \frac{a_1\, t(L)}{v_0} \quad .$$

Due to geometry comparison α can also derive from the height Δx divided by the distance Δz the particles are travelling in the middle interspace of the selector:

$$\tan\alpha = \frac{v_x(L)}{v_0} = \frac{1}{v_0}\,\frac{q_e\,U_1}{m_e\,d}\,\frac{L}{v_0} \overset{!}{=} \frac{\Delta x}{\Delta z} = \frac{f_3(z) - f_2(L)}{z - L} \tag{4.8}$$

which gives

$$f_3(z) = x_0 + \frac{1}{2}\,\frac{q_e\,U_1}{m_e\,d}\left(\frac{L}{v_0}\right)^2 + \frac{q_e\,U_1}{m_e\,d}\,\frac{L}{v_0^2}\cdot(z - L) \quad . \tag{4.9}$$

The second plate pair again can be seen as a plate capacitor so that the particle trajectory in part four is parabolic. The corresponding equation is similar to the

term in equation 4.7 multiplied with -1 due to the inverted voltage. Since the selector is supposed to set both x_t and $\dot{x}_t$ to zero the origin of the parabola is set to $(z,\, x) = (L + K + L,\, 0)$, giving

$$f_4(z) = x_{\mathrm{oA}} - \frac{1}{2}\,\frac{q_e\,U_2}{m_e\,d}\left(\frac{z-(L+K+L)}{v_0}\right)^2 \quad . \tag{4.10}$$

The fifth and last part is the trajectory of the particles leaving the selector. The corresponding function is the same simple expression as in equation 4.6 just with x_{oA} instead of x_0 referring to the final distance to the optical axis.

These functions build up the mathematical framework for the calculation of the particle path. Now, the physical constraints can be implemented. The first constraint is the differentiability between f_3 and f_4. On this point, both functions have to satisfy the following expression:

$$\begin{aligned}\frac{\mathrm{d}}{\mathrm{d}z}f_4(z)\bigg|_{L+K} &= -\frac{q_e\,U_2}{m_e\,d}\,\frac{1}{v_0^2}\,(z-(L+K+L))\bigg|_{L+K} = -\frac{q_e\,U_2}{m_e\,d}\,\frac{(-L)}{v_0^2}\\ &\stackrel{!}{=} \frac{\mathrm{d}}{\mathrm{d}z}f_3(z)\bigg|_{L+K} = \frac{q_e\,U_1}{m_e\,d}\,\frac{L}{v_0^2} \quad .\end{aligned} \tag{4.11}$$

As one can already see, equation 4.11 is fulfilled, if U_1 is equal to U_2. So the same voltage U is allocated to the both plate pairs in one sub-selector. However, the sign of the voltages is different since the trajectory curvature has to be inverted in the second plate pair. This difference is considered mathematically a priori by inverting the parabolic approach in equation 4.10.

The second constraint is the continuity condition between the third and fourth part, so f_3 and f_4. Here, the following expression has to be satisfied:

$$\begin{aligned}f_4(L+K) &= x_{\mathrm{oA}} - \frac{1}{2}\,\frac{q_e\,U}{m_e\,d}\,\left(\frac{-L}{v_0}\right)^2\\ &\stackrel{!}{=} f_3(L+K)\\ &= x_0 + \frac{1}{2}\,\frac{q_e\,U}{m_e\,d}\left(\frac{L}{v_0}\right)^2 + \frac{q_e\,U}{m_e\,d}\,\frac{L}{v_0^2}\cdot K \quad .\end{aligned} \tag{4.12}$$

Solving for x_{oA}, which of course has to be zero, yields:

$$x_{\mathrm{oA}} = x_0 + \frac{q_e\,U}{m_e\,d}\,\frac{L\,(L+K)}{v_0^2} \stackrel{!}{=} 0 \quad .$$

Finally, a mathematical expression for $U_1 = U_2 = U$ can be formed:

$$U = -x_0\frac{m_e\,d}{q_e}\,\frac{v_0^2}{L(\,L+K)} \quad . \tag{4.13}$$

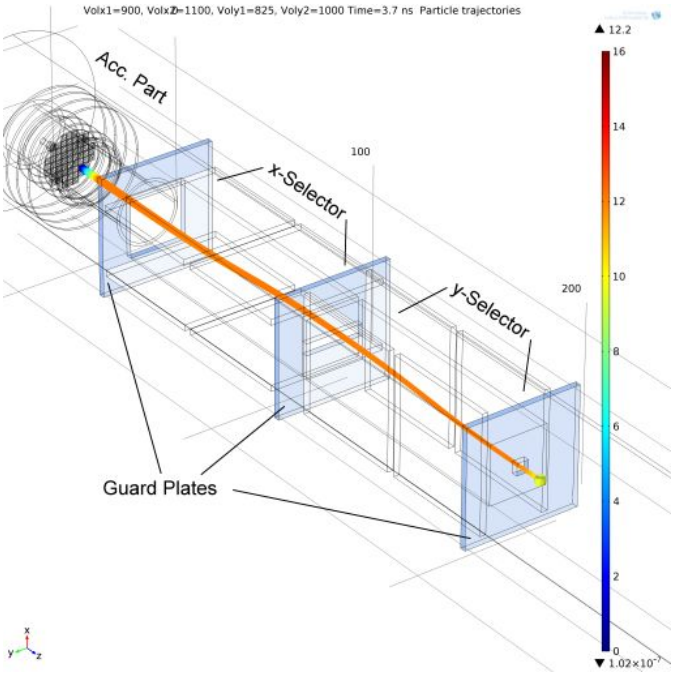

Figure 4.23: This 3D trajectory plot shows a particle beam emitted from the inlet matrix entering the selector where the particles propagate through the potential plates and the guard plate windows. The inlet is $(-4, -4)$. The acceleration part is still included in this overview. The particles are deflected by the electrostatic fields in the subselectors to be aligned with the optical axis and the third particle window.

This expression delivers the specific selector potential which is required to deflect a particle beam starting at x_0 onto the optical axis so that x_t and $\dot{x}_t$ both are zero after passing the selector. Naturally, U depends on the selector geometry properties as the plate length and the space between the plate pairs. The gap between the plates, d, is set due to the diameter of the xenon crystal. The calculation of the potentials of the y-selector can be done analogously.

Implementation in the Simulation

By equation 4.13, it is possible to calculate the suitable potential for a given geometry and inlet position (x_0, y_0). Figure 4.23 shows a trajectory plot of the whole selector and the particle inlet part. The plate length L as well as the length of the guard plates is 40 mm. All plates are quadratic. The plate pair distance K is 3 mm and the distance between selector and guard plates is 1.5 mm. The particle inlet is set to $(-4, -4)$ mm. The acceleration part is still implemented here and the particles are accelerated up to about 12.1 keV ($6.4 \times 10^7\,\mathrm{m\,s^{-1}}$).[28] With these values, equation 4.13 yields $U = 1087\,\mathrm{V}$ for the potential at the selector plates.

The resulting potential distribution in the selector can be seen in figure 4.24. It shows a potential surface plot in the zx-plane with a y-offset of $y_0 = -4$ mm – equal to the particle inlet. The guard plates have a potential of 0 V and therefore

[28] The kinetic energy of the single particles in the beam differs slightly, so that this energy is just an average value.

are displayed in green. Each sub-selector plate has the potential $\pm U/2$. Since x_0 is negative here, the first bottom plate of the x-selector has to be at negative potential in order to deflect the beam in positive x-direction. In the case of the second plate pair the potentials and hence the trajectory curvature are inverted to re-align the beam with the optical axis. The very same procedure is applied in the y-selector so that the particles can exit the selector through the narrow window in the third guard plate. The potentials inside the y-selector are displayed as they are arranged at the height of the cut plane so that smaller values than $U/2$ are indicated here.[29]

However, the value calculated for U from equation 4.13 is not exactly the potential required to deflect the beam onto the optical axis. This is due to the neglected stray fields outside of the plate capacitors and the assumption that the electric fields are completely homogeneous and constrained to the borders of the capacitor. The second potential surface plot in figure 4.24 displays the stray fields in the x-selector with the electric field indicated as an arrow matrix.

The thickness of the arrows correlates with the electric field strength E. E is very high at the corners of the potential plates and especially between both plate pairs, where the largest potential difference occurs.[30] The plot also presents the stray fields outside of the x-selector, e.g. left of the first guard plate. Due to the particle window in this plate, the electric field bulges outwards and establishes a certain field strength outside of the selector. Additionally, the field inside the selector is less homogeneous nearby the guard plates. At the transition between both plate pairs, the arrow map shows considerably strong field components apart from the predominant x-direction as well. Due to these effects, U has to be adjusted in the simulation to lead the particle trajectories right on the desired path. If this is successful, the simulation delivers particle plots as presented in figure 4.23. Here, the potentials of the four plate pairs are in the range between 825 V and 1100 V.

The inhomogeneities in the selector fields also cause a focussing and distortion effect of the particle beam and the projected inlet shape. In figure 4.25a the inlet shape can barely be recognised. This 3D plot is based on a xy-topview of the whole selector system. The particles start at the inlet $(-4, -4)$ as it can be seen in the lower left quadrant. Note that the acceleration part is implemented in this simulation to also display its influence on the distortion as it would be in the actual experiment as well. The inlet shape is distorted massively, mainly due to the influence of the acceleration part on the initial particle beam and inhomogeneities of the selector fields.

[29] The guard plate windows can be seen as black horizontal lines indicating the window edges. In the case of the third guard plate, however, the cutplane crosses the plate beyond the edges of the window since its width is only 4 mm.

[30] This field effect at sharp points is why only considering the common vacuum breakdown field strength for the calculation of K is not practical.

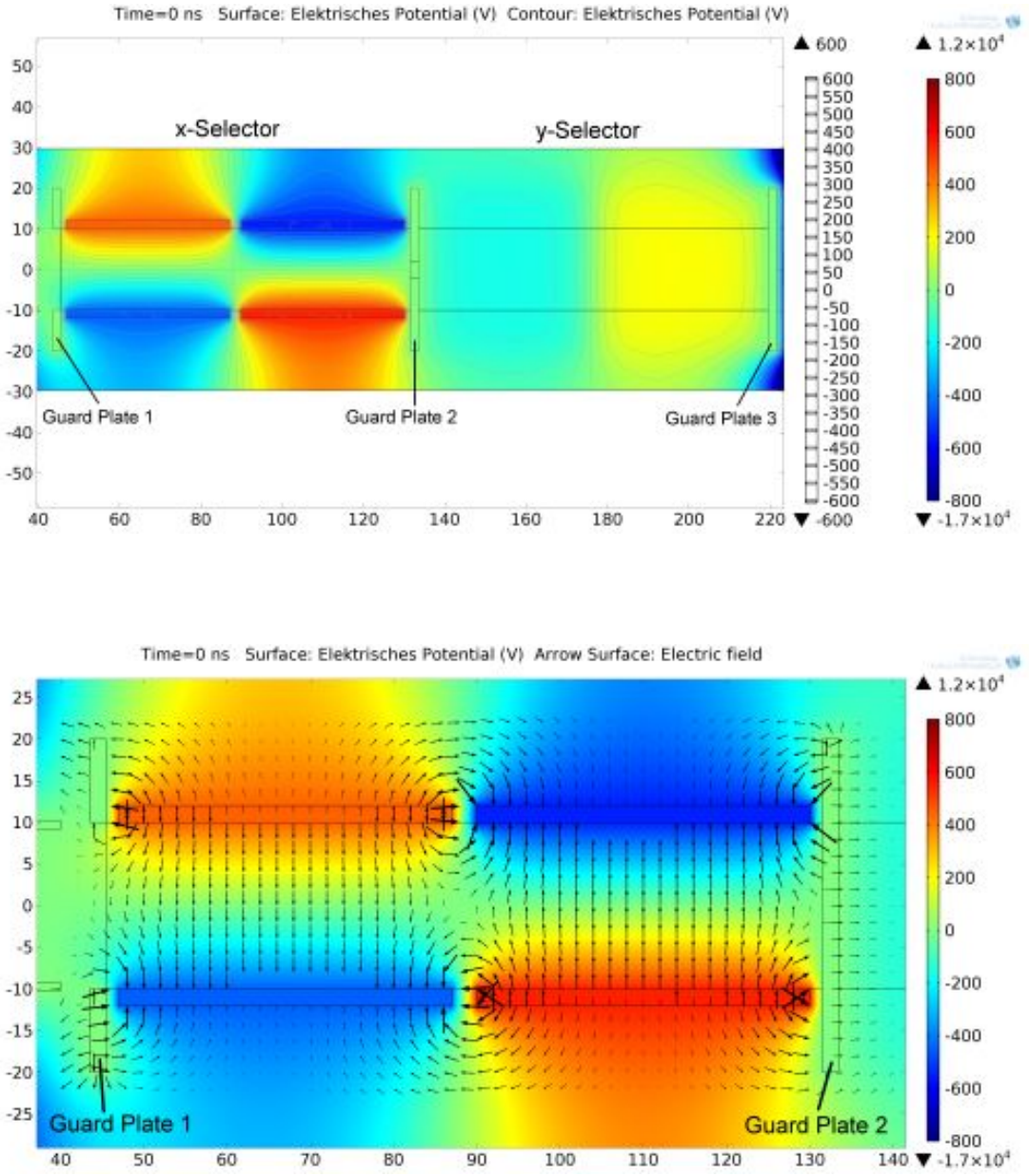

Figure 4.24.: This figure shows two surface plots of the selector system. The potential distribution presents the required configuration to align particle beams with a negative inlet position. The upper plot shows the entire selector system and the lower plot presents a zoom of the x-selector. Black arrows indicate the direction of the electric field. The arrow thickness corresponds to the field strength.

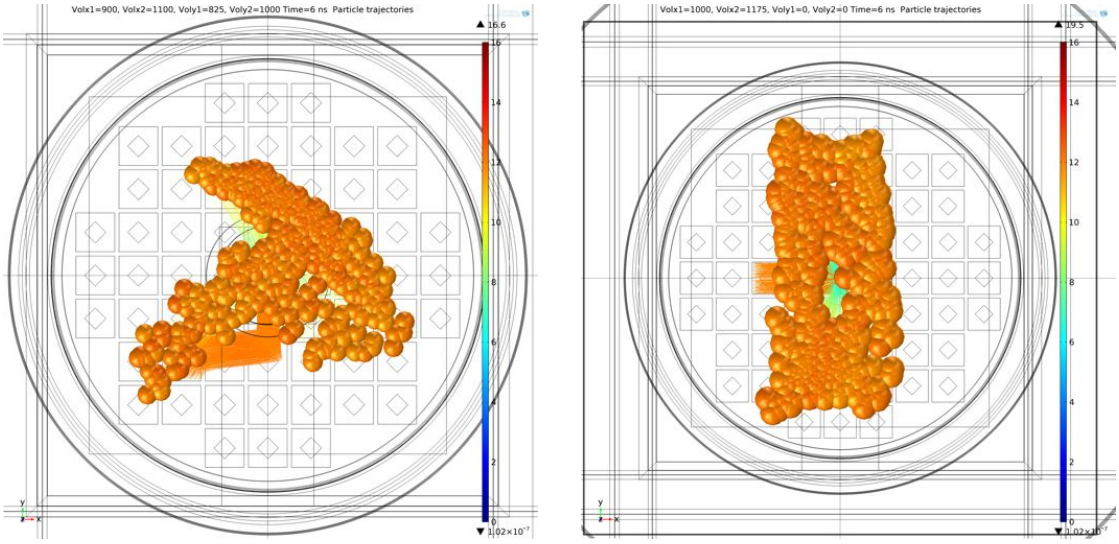

(a) Distortion effect **(b)** Focussing effect

Figure 4.25.: These particle topviews presents the projected image of the inlet shape at the z-position of the detector. The left simulation is done with a bad imaging performance causing the inlet shape to be distorted beyond recognition. The right plots presents the result of minor focussing effects caused by the electric fields inside of the x-selector.

To examine the functionality of the selector in order to improve its performance, the following simulations are performed without acceleration part but with the adapted particle inlet as explained above. Figure 4.26 presents a trajectory plot of the selector with an inlet of $(-4, 0)$. The colour scale is set to a narrow range around the average energy of the particle inlet. The particles are slowed down significantly in the first part of the x-selector due to the negative potential of the first bottom plate. Since this plate has to deflect the particle beam in direction of the optical axis, the nearest plate for particles entering the selector always has a negative potential. At the transition to the second plate pair, the particles get re-accelerated due to the positive potential of the second bottom plate.

The deceleration of the particles within the first plate pair is also the reason why a lower potential is required here. As one can see in the headline of figure 4.26, U_{x1} is 1000 V whereas U_{x2} is set to be 1175 V for the proper deflection of the particles. Particles decelerated inside of the first plate pair experience a stronger deflection because of the larger proportion of the transversal velocity component compared to v_z. As a result, the potential of the first pair can be reduced. This is also why

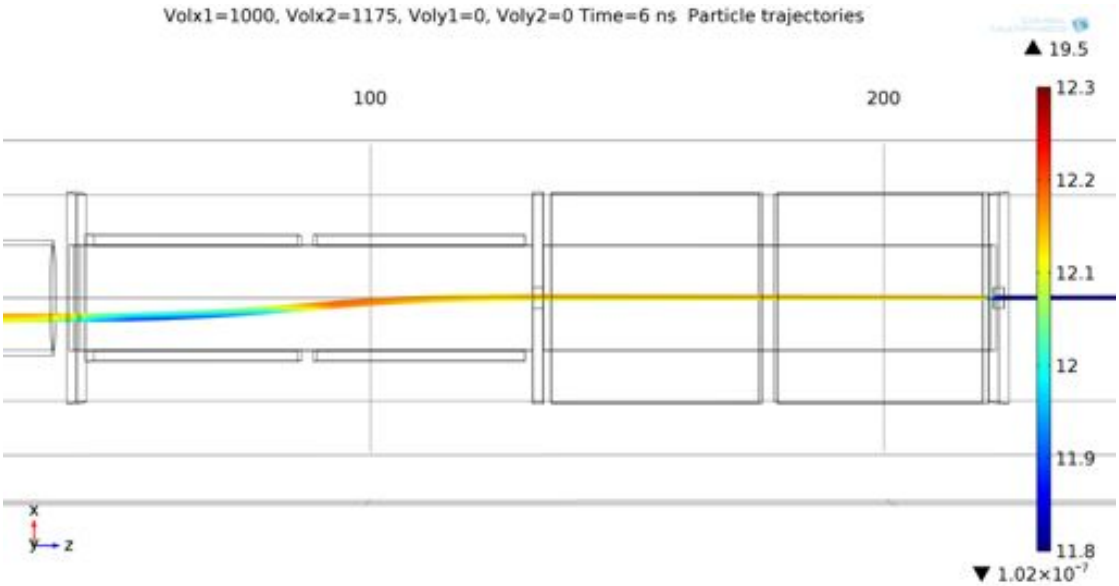

Figure 4.26.: This particle trajectory plot shows the pathway of a particle beam through the selector geometry. The inlet is set to $(-4, 0)$. The energy colour scale is narrowed to a small range around the average energy to display different particle velocities due to inhomogeneities within the selector fields.

the potentials of the second plate pair in figure 4.24 seem to be a little stronger than the first plate pair.[31]

Another consequence of the deceleration is a small focussing effect. One can see in figure 4.26 that the deceleration of the lower part of the particle beam is stronger than that of the upper part at the level of the first plate pairs. Hence the lower part of the beam experiences a slightly stronger deflection than the upper one and the particle beam gets focussed. The consequence can be seen in figure 4.25b. The inlet still is $(-4, 0)$ in this case so that the height (y-direction) of the particle image at the level of the detector represents the pure magnification of the electron lens whereas the width (x-direction) is narrowed due to the focussing effect inside the x-selector. Although the inlet shape can be recognised here, the image is still distorted significantly, which is why a fine-tuning of the selector performance is necessary.

[31] It is important to note that this stronger deflection power is no direct effect of the longer duration of the particle passage of the first plate pair since the particles cross the same potential difference independent of their velocity. However, the deflection angle is different due to the smaller ratio of v_t and v_z in the case of faster particles.

Fine-Tuning

At this point, two principle ways to achieve a better performance of the selector are being discussed. The first way is to reduce the intensity of the focussing effect. This effect is connected with the spatial expansion of the particle beam with respect to the selector fields so that some electrons are always closer to the negative plate than others. The second way is to reduce the bad influence of stray fields like the deceleration of the particles within the first plate pair.

The focussing effect in the selector is due to the asymmetric deceleration of the particle beam. It can be reduced, if the deceleration discrepancy among the particles is decreased, which can be done by lowering the selector potential U. This potential depends on the particle velocity and the selector geometry so that the modification of U can be achieved by decreasing the plate length L and the initial velocity v_0. In the following simulations, L is set from 40 mm to 60 mm. To avoid an increasing impact of minor distortions occurring along with a longer pathways of the particle beam, the plate length was not enlarged any further.[32] Additionally, the kinetic energy is reduced from about 12 keV to about 7 keV.[33] A larger reduction of the velocity is not possible since the Timepix detector requires a kinetic energy of about $6 - 7$ keV to detect electrons. Introducing these two modifications to equation 4.13, the selector potential can be decreased from about 1100 V to about 350 V which is approximately one third. Consequently, the impact of the focussing is also reduced and the resulting simulation plots are presented later.

The second way to improve the imaging performance is to limit the impact of the stray fields and the transversal field components. As one can see in figure 4.24, such field components occur directly in front of the selector. The particles crossing these stray fields experience a deceleration and maybe other effects which are disadvantageous for the imaging quality. These effects could be ruled out to a large extend if there were only stray field components pointing into x-direction along the particle pathway. This can be achieved very easily by breaking the symmetry of the potentials of the selector plates. Until this point, the voltage difference of the selector plates is U (and each plate is set to a voltage of $+U/2$ or $-U/2$). Consequently, particles entering the selector have to move against a negative electric field within the first plate pair as mentioned above along with figure 4.26. This deceleration can be avoided if the corresponding, decelerating, negative potential is reduced. Since the total potential difference in the selector has to be maintained for a proper deflection, this can only achieved by shifting

[32] A comparison of image shapes based on different plate lengths L can be found in figure A.1 in the addendum.

[33] In terms of velocity, this means a decrease from about $6,4 \times 10^7\,\mathrm{m\,s^{-1}}$ to about $4,9 \times 10^7\,\mathrm{m\,s^{-1}}$. This reduction of the particle energy is mentioned in the acceleration part section, as well.

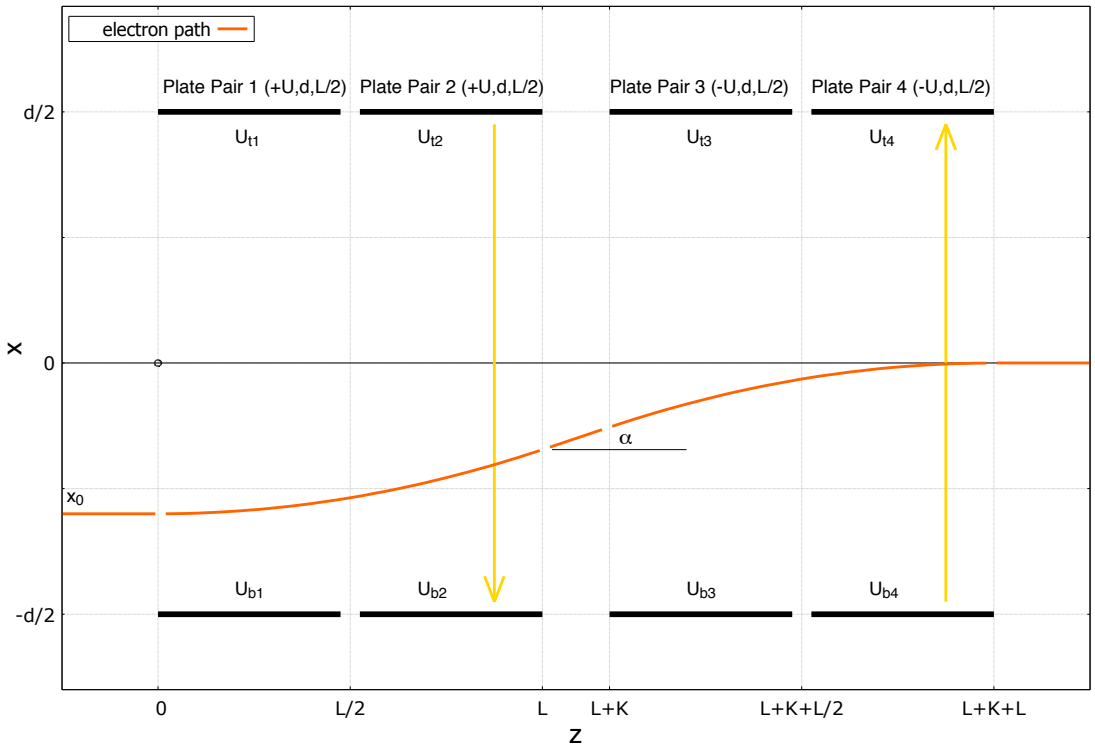

Figure 4.27.: This plot presents a scheme of the adapted selector geometry. The potential plate pairs are doubled for each sub-selector and the potentials can be applied individually.

the potential zero point, which means to shift the 0 V area inside the selector in y-direction. The goal is to form the shape of the equipotential lines in the selector so that the 0 V-area follows the trajectory of the particle beam. This challenge is explained in the following paragraphs.

Figure 4.27 presents a schematic view of an adjusted selector geometry in contrast to figure 4.22. Since the x- and y-selectors are symmetrical, the same considerations apply for both parts and therefore only the x-selector is considered here. One can still recognise the original geometry consisting of two plate pairs with length L, gap d and distance K. Here, each potential plate is divided into two plates with the same depth. The distance between these new sub-plate pairs is set to $K/2$ so that the new plate length is $L/2 - K/4$. Each of the eight sub-plates can be supplied with a different potential. The upper plates have a potential U_{ti} and the lower plates U_{bi}, where t stands for *top*, b for *bottom* and i refers to the specific sub-plate pair 1 to 4. Until this point the single voltages were set to

	Initial deflection (first two plate pairs)				Re-alignment with o.a. (last two plate pairs)			
U_{pi}	U_{t1}	U_{b1}	U_{t2}	U_{b2}	U_{t3}	U_{b3}	U_{t4}	U_{b4}
sign of U	+	-	+	-	-	+	-	+
adjust. sign	-	+	-	+	-	+	-	+
ω_i	100%	100%	75%	75%	25%	25%	0%	0%

Table 4.1.: This table presents the set of parameters used for the fine-tuned selector with adjusted 0 V-tunnel. The signs and the weighting factor ω_i refers to equation 4.15. The arrangement of the potentials U_{pi} within this table correlates with their location in figure 4.27.

$$U_{pi} = \begin{cases} +U/2 & \text{if } p,i \text{ is } t,(12) \text{ or } b,(34) \\ -U/2 & \text{if } p,i \text{ is } t,(34) \text{ or } b,(12) \end{cases} , \tag{4.14}$$

where p indicates the position of the specific plate. The numbers i in brackets still refer to the both original (big) plate pairs. The plate pairs are supplied with the potential $\pm U/2$. The sign of the potentials is chosen such that the negative potential is allocated to the first bottom plate for negative x_0 and to the first top plate for positive x_0, respectively.

Now, the potentials within each plate pair are no longer symmetrical, which means that the have no longer the same opposite value to shift the effective 0 V-line in the selector. The new potentials are calculated by

$$U_{pi} = \pm U \cdot \left(\frac{1}{2} \pm \omega_i \cdot \frac{x_0}{d} \right) \quad . \tag{4.15}$$

In this equation, U is still the selector potential according to equation 4.13 and the term 1/2 is the symmetric term of equation 4.14. The second part refers to the shift of the 0 V-line onto the position of the particle beam x_0 with respect to the plate gap d by increasing or reducing the potentials of each plate. ω_i is the weighting factor of this shift for each individual sub-plate pair. The two signs in equation 4.15 both depend on p and i. Table 4.1 lists the set of parameters of equation 4.15 which was used in the following simulations.

The actual sign of U depends on whether x_0 is positive or negative as in the case of two plate pairs. If x_0 is negative, the first and second bottom plates have

a negative potential, the corresponding top plates a positive potential and so on. Note that this sign also depends on the definition of U leading to positive voltages at the first selector plates and negative ones at the last plates. The second sign marks the direction of the shift of the 0 V-line. If x_0 is positive, all top plate potentials U_{ti} are decreased to reduce the dominant effect of their fields on the particle beam. In the case of figure 4.27, this is the other way round. Consequently, top plate potentials are adjusted with a negative term, bottom plate potentials with a positive term.[34] At last the weighting factor allows a regulation of the absolute shift of the 0 V-line relative to the particle pathway. This is necessary since the x-position of the particle changes throughout the selector system. The proper choice of the single ω_i has to be determined empirically by simulations.

With the settings presented in table 4.1 the fine-tuning is complete. Figure 4.28 presents a particle trajectory plot of the x-selector including the adjusted geometry. The inlet is $(-4, -4)$. The plot shows the shift the 0 V-region in grey onto the particle pathway; e.g. the potential of the plates close to the particle entry at $y = -4$ mm are reduced. The equipotential lines are well aligned with the particle trajectory and this potential distribution can be regarded as 0 V-tunnel around the beam. Consequently, transversal stray field components are avoided – especially in front of the first guard plate. As in figure 4.26, the particle energy is 7 keV and the energy range is set to 0.5 keV to allow qualitative comparisons. Apparently, the focusing impact by the selector fields is decreased massively since no major change in the particle velocity can be seen any more. In summary, the alignment of the 0 V-tunnel to the particle pathway due to the modified selector potentials works quite well. The results on the image quality are shown in section 4.5.

4.4.3. Electrostatic Lens System

The lensing system is responsible for the focussing and optical magnification of the particle beam and hence the projected inlet shape. Two types of lenses were examined in this thesis: An aperture lens system consisting of three parallel aperture plates and a hyperbolic lens with two cones and a torus in the centre. Both lens types consists of three electrodes to apply the lensing potentials. This kind of electrostatic lensing systems is explained in section 4.1 as well as the basic principles of focussing charge carrier beams with electrostatic fields.

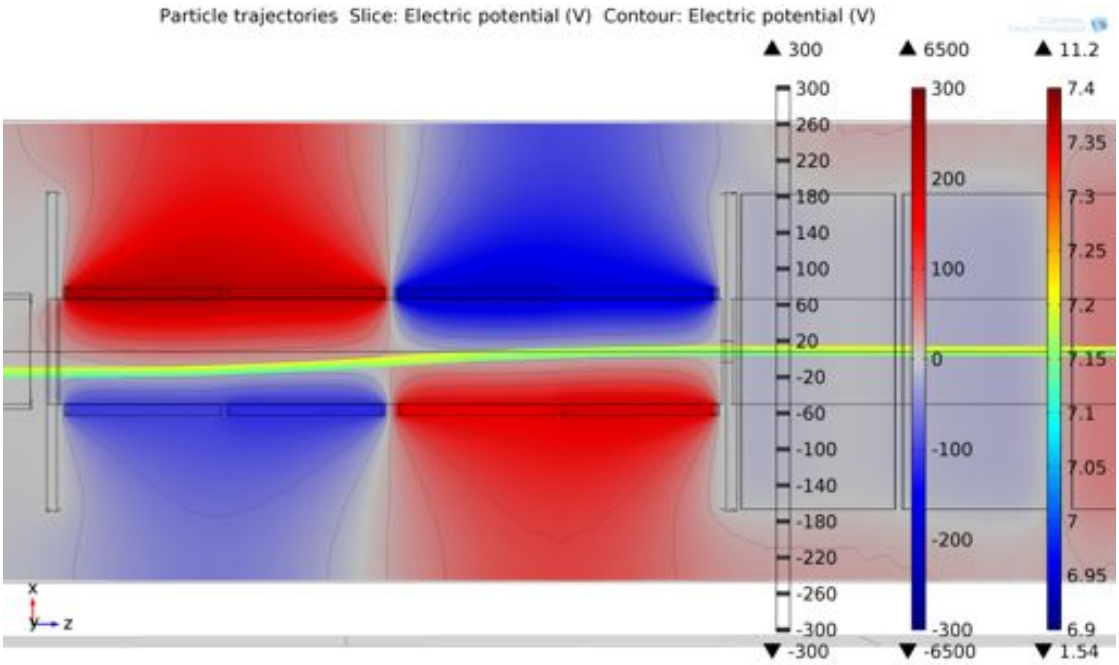

Figure 4.28.: This figure presents the particle trajectory plot with the potential distribution of the adapted selector system. The three-dimensional trajectory is embedded in a potential surface plot. The y-offset of the corresponding cut plane is equal to the y-inlet. Potentials are shown in a wave colour scale and contour lines are drawn in grey. The particle beam shows no major focussing artefacts.

Aperture Lens

Figure 4.29 presents an overview of the aperture lens design in the simulation. This lens consists of three aperture plates with length $L = 25\,\text{mm}$ and thickness $T = 1\,\text{mm}$. The distance D is $3\,\text{mm}$. The circular aperture pinholes in the centre of the plates have to be larger than the electron beam but small enough to generate the aperture character of the lensing system. The diameters of the pinholes are $d_1 = d_3 = 5\,\text{mm}$ and $d_M = 4\,\text{mm}$ so that the pinhole of the middle lens is as large as the particle window of the third selector guard plate. The middle pinhole is somewhat smaller than the outer ones. The long cylinder in the middle is no part of the lensing geometry but a part of the vacuum domains. This allows to introduce a different mesh size inside of the lens to carry out a finer simulation of the actual

[34]Note that x_0 is negative in figure 4.27. This means, the negative adjustment sign of the top plate potentials is compensated and the positive potentials of the top plates are increased as expected.

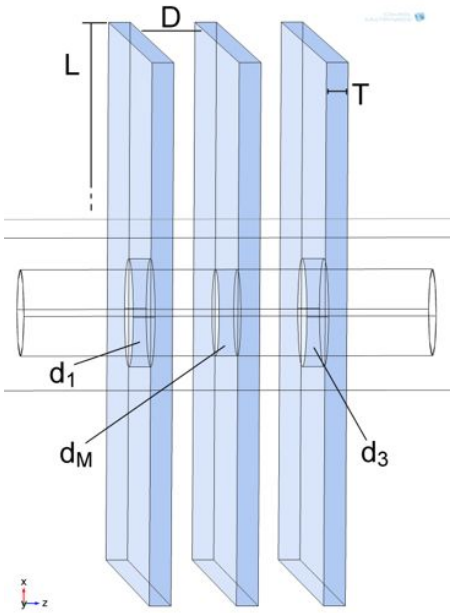

Figure 4.29: This sideview shows the geometry of the aperture lens system consisting of three individual aperture lenses. The length of the plates is L, their thickness T and the distance between the plates is D. The diameters of the pinholes are d_1, d_M and d_3 for the first, middle and last plate respectively. The cylinder in the middle is an artefact of the vacuum domains, which allows to set a finer mesh structure in the interesting focussing region of the lens.

particle focussing.[35] All pinholes and the vacuum cylinder are in line with the optical axis.

The distance D of the aperture plates has to be chosen under consideration of the voltage assigned to the plates as mentioned in the previous section. A distance of 3 mm allows potential differences up to 30 kV. Both thickness and plate length are not changed throughout the simulations. Other combinations for the pinhole diameters (d_1, d_M, d_3) were examined as well. Several examples are presented in figure A.2 in the addendum. The $(5, 4, 5)$ combination showed the best trade-off of a strong focussing power and small imaging aberrations as spherical distortions or wavy edges of the inlet shape. The diameter values $(5, 4, 5)$ are used throughout all of the following simulations.

Figure 4.30 presents the potential distribution of the aperture lens system. The potential is evaluated in a zx-cutplane without y-offset. The three aperture plates with the pinholes can be recognised as well as the vacuum cylinder in the middle. The third guard plate of the selector including its particle window is visible on the left. This guard plate is quite important to shield the selector from the strong lensing fields. The potential is illustrated by a rainbow colour scale. The three aperture plates have a potential of -6500 V, $+6500$ V and -3500 V from left to right. Other lensing potential configurations are also examined and the corresponding

[35] This is a trick to achieve a better evaluation of the particle tracks in the lensing system without large computing time as it would be in the case of a finer mesh size in the whole geometry. All plots of the lenses show this small vacuum cylinder.

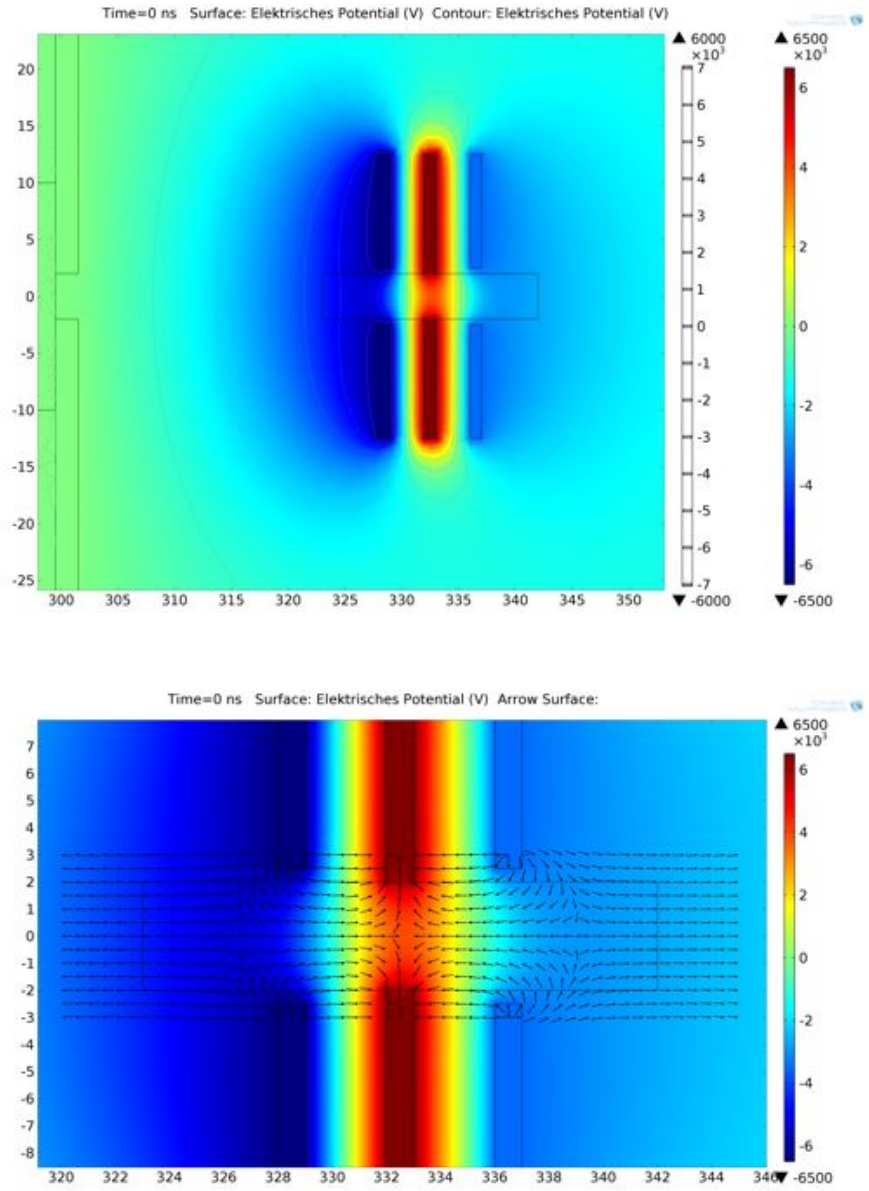

Figure 4.30.: The two surface plots illustrate the potential of the aperture lens. The first plate has a high negative potential whereas the middle lens is supplied with a high positive voltage and third lens with about half the value of the first potential. The dominant focussing region can be seen in the lower zoom into the inner region of the aperture lens system. An arrow map illustrates the inverted electric field. The dominant focussing region is located at the transition from a homogeneous deceleration field to the convex focussing field at about $x = 326$ to 328 mm.

plots can be seen in figure A.3 in the addendum but most of them either present a less strong focussing power or bad imaging artefacts.[36]

The lower plot shows a zoom of this near field region with the electric field strength and direction illustrated by arrows. The direction of the arrows is inverted to better illustrate the acceleration and focussing fields experienced by the (negative) electron beam. The lensing potential distribution can be divided in two areas: The far field beyond the inner vacuum cylinder, where the potential differences and curvature are rather small and the particles are decelerated homogeneously without any focussing effect. Secondly, in the near field inside of the vacuum cylinder, significantly stronger curvatures of the contour lines occur and the electric field arrows point towards the optical axis indicating the focussing of the electron beam.

Figure 4.31 shows the corresponding particle trajectory plot. The particle energy is illustrated by a rainbow scale with a kinetic energy of the particles of 7 keV. The particles are accelerated in the far field and the focussing effect occurs quite promptly at the level of the first aperture plate.[37] The focussing strength depends on the intensity of this potential as well as the particle velocity at the level of the focussing region since the deflection towards the optical axis is less dominant if the remaining particle velocity is rather small. However, the minimum particle energy has to remain about a certain value to avoid distortions of the imaged shape. In several simulations, 1.2 to 1.7 keV turned out to be a good range for a reliable imaging process and the decelerating first potential has to be chosen with respect to that range. In this simulation, the minimum energy is 1.54 keV and occurs directly in front of the first aperture plate.[38]

The particles are re-accelerated and defocussed behind the middle plate. The defocusing effect is far less intense than the focussing effect of the first plate due to the smaller beam diameter behind the middle plate and the larger velocity. The third plate can be used to control the defocussing impact of the field behind the middle lens and therefore the focussing effect of the whole system. On the other hand, the strong acceleration caused by the middle lens potential is compensated so that the particles leave the lensing part with approximately the entry velocity. Having set the lensing potentials properly with respect to the initial velocity, a good focussing efficiency can be achieved. The focussing power can be controlled to a certain degree by adapting the potentials. This is important since the sensor

[36] The potential configurations presented there have to be scaled down according to the reduced particle inlet velocity.

[37] It is important to add that the time resolution of the particle motion evaluation in the time-dependant study can intensify the sharpness of the sudden focussing of the electron beam. This results from the non-continuous evaluation-point based way how particle trajectories are plotted in COMOSL.

[38] The minimum energy is displayed at the bottom of the particle energy rainbow scale in the trajectory plot.

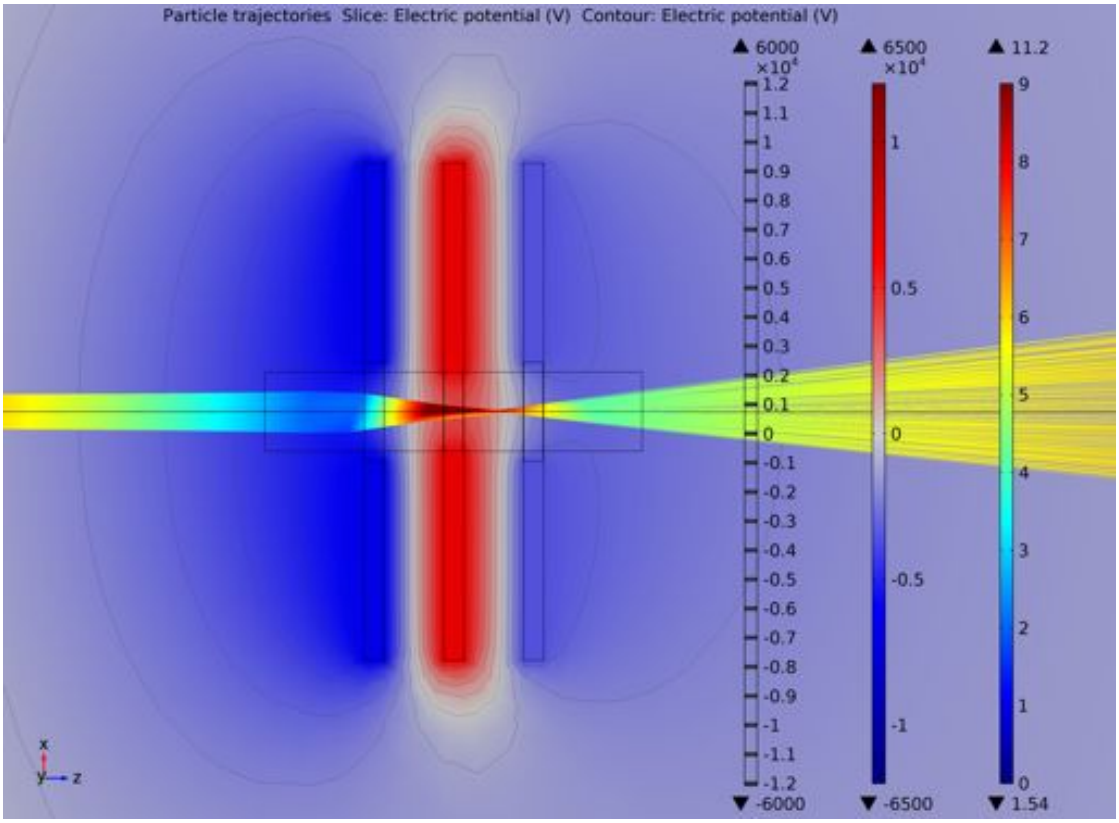

Figure 4.31.: This combined particle trajectory and potential surface plot presents the focussing of the particle beam caused by the aperture lens system. The particle beam is decelerated in the far field of the lenses and then enters the focussing region in front of the first aperture plate. Afterwards, the focussed particle beam gets accelerated again so that it leaves the lensing system shortly after the focus point.

layer surface of the Timepix detector chip is supposed to be fully illuminated by the projected inlet after magnification. The detector is located at a fixed distance to the lensing part so that a manipulation of the focussing power is an important tool. With a length of the inlet shape of 2 mm (as expected for $\beta\beta0\nu$-tracks in solid xenon) and the chip size of 14 mm, a magnification factor of the lensing system of 7 is realised.

Hyperbolic Lens

The second type of lensing system is the so-called hyperbolic lens. This lens type is supposed to provide a smoother main focussing region. This might allow to do electron imaging with less strong distortions and aberration errors. The hyperbolic

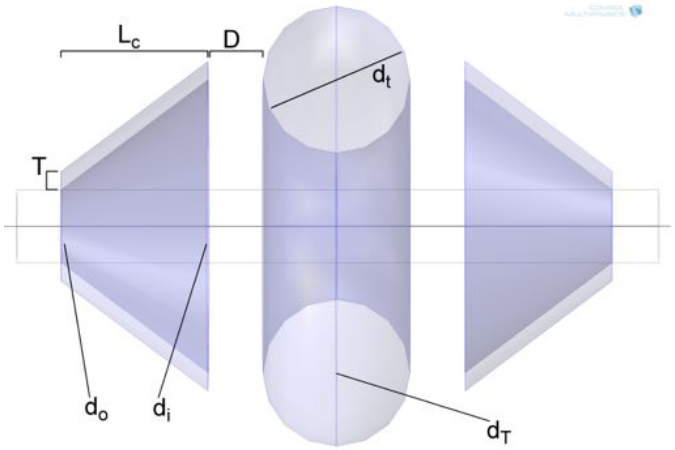

Figure 4.32: The hyperbole lensing system consists of two cone-electrodes enclosing a torus-shaped electrode in the middle. The length of the cones is L_c, the length of the torus is its minor diameter d_t and the distance between the electrodes is D. The outer and inner diameters of the cones are d_o and d_i respectively and their radial thickness is T. The major diameter of the torus is equal to d_i.

lens in this work consists of two hollow cones that encloses a torus shaped electrode in their centre. The geometry can be seen in figure 4.32.

Both cones of the hyperbole lens open up to the torus in the centre. Their outer smaller diameter d_o is 4 mm in this simulation (equal to the aperture pinholes), their inner larger diameter d_i is 8 mm and the radial thickness T is set to 1 mm. The length (or height) of the cones L_c is 8 mm. Both cones are identical. The distance D between the single electrodes is set to 3 mm again considering the possibility of potential breakdowns. The minor diameter d_t of the torus (and therefore its length) is set to 8 mm so that all electrode lengths are identical. The major diameter d_T of the torus is equal to d_i. A cylindrical vacuum domain with finer mesh size allows a better resolution of the particle tracks in the centre focussing region again.

Figure 4.33 shows the potential plot of the hyperbolic lens system. In this simulation, the potentials of the front cone, the torus and the back cone are $V_{cf} = -6000\,\mathrm{V}$, $V_t = +7000\,\mathrm{V}$ and $V_{cb} = -2000\,\mathrm{V}$ respectively. The kinetic energy of the particle beam is 7 keV. Several properties of the hyperbolic lens can be noticed:

- Similar to the aperture lens, the middle lens has a positive potential and the other two electrodes a negative one. Again, the potential of the third lens is somewhat smaller than the other potentials.

- The contour lines present a much smoother transition between the individual potentials and consequently between the deceleration field, the convex field of the focussing region and the concave field of the middle lens. This is due to the expanded geometry of the lens – especially if compared to the aperture

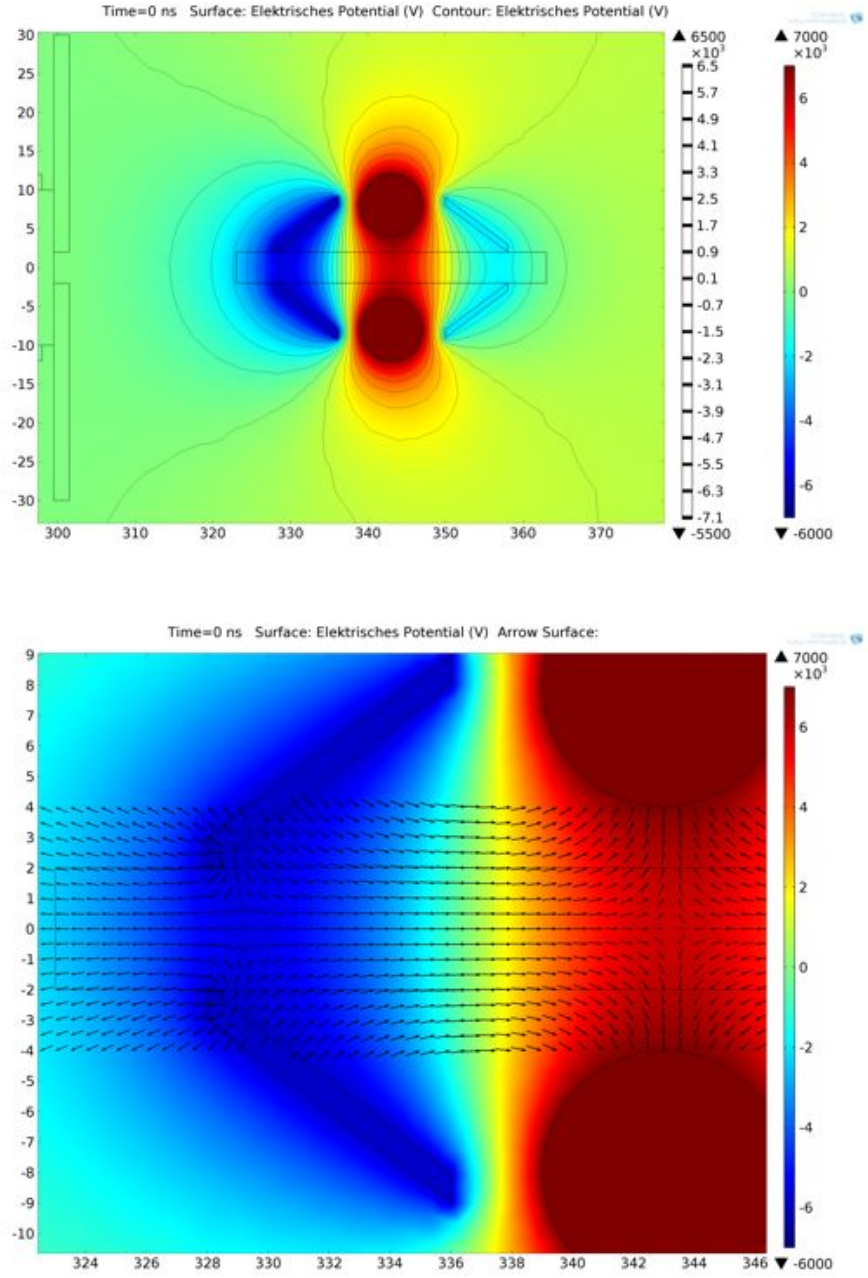

Figure 4.33.: This two surface plots present the potential of the hyperbolic lens system. Both cones have a negative potential, the torus electrode is supplied with a positive potential similar to the aperture lens. The inverted arrow map shows a zoom into the inner focussing region of the hyperbolic lens.

lens. It is assumed that this smooth transition reduces negative imaging artefacts such as spherical aberrations.

- The far field of the hyperbolic lens is far less dominant than in the case of the aperture lens since the shielding of the middle lens because of the negative potential electrodes not being that strong. For that reason, the influence of the lensing potentials at the level of the third selector guard plate and at the level of the detecting part is reduced. As a consequence, strong potential gradients in front of the detector sensor layer, which is on a small positive potential, are avoided as well as the involved influence on the particle beam immediately before hitting the detector (see following paragraph).

The lower arrow map plot shows a closer view of the inner part of the hyperbolic lens. The far field in front of the lens is directed against the motion of the particles causing a homogeneous deceleration. The dominant focussing region is the deep blue region located directly behind the opening of the first cone, where the strongest transversal field components appear. However, transversal components can be found up to the 0 V-region in green. This results in a much longer focussing region in contrast to the aperture lens.

Figure 4.34 presents the trajectory plot associated with the potential distribution shown above. At first and similar to the aperture lensing system, the electrons are decelerated rather homogeneously. Directly in front of the first cone, a slight concave field (and hence defocussing effect) occurs due to the increasingly strong curvature of the potential lines around the optical axis. Shortly behind the cone opening, the dominant focussing region forces the particles towards the focal point on the optical axis. While approaching this point, the particles get re-accelerated by the middle lens potential. Due to this the immediate influence of transversal field components beyond the dominant focussing region is rather low (e.g. the defocusing effect at the level of the torus electrode). Additionally, the particles are exposed to a smaller field curvature due to the small beam diameter as in the case of the aperture plate. Consequently, the particle trajectories are very straight beyond the first cone and the beam eventually leaves the lensing system continuously expanding.

The minimum particle energy inside of the first cone should not drop below approximately 1.4 keV to maintain a good imaging quality (the simulation shown in figure 4.34 is as far as one can go). A higher negative value of the first potential cause significant distortions of the inlet shape whereas smaller potentials reduce the focussing effect massively. The torus potential has to be large enough to generate the field curvature inside of the first cone but not too large to imply a bad impact on the beam at the level of the focal point. Potential values which are slightly larger than that of the front cone showed good results. The third cone compensates

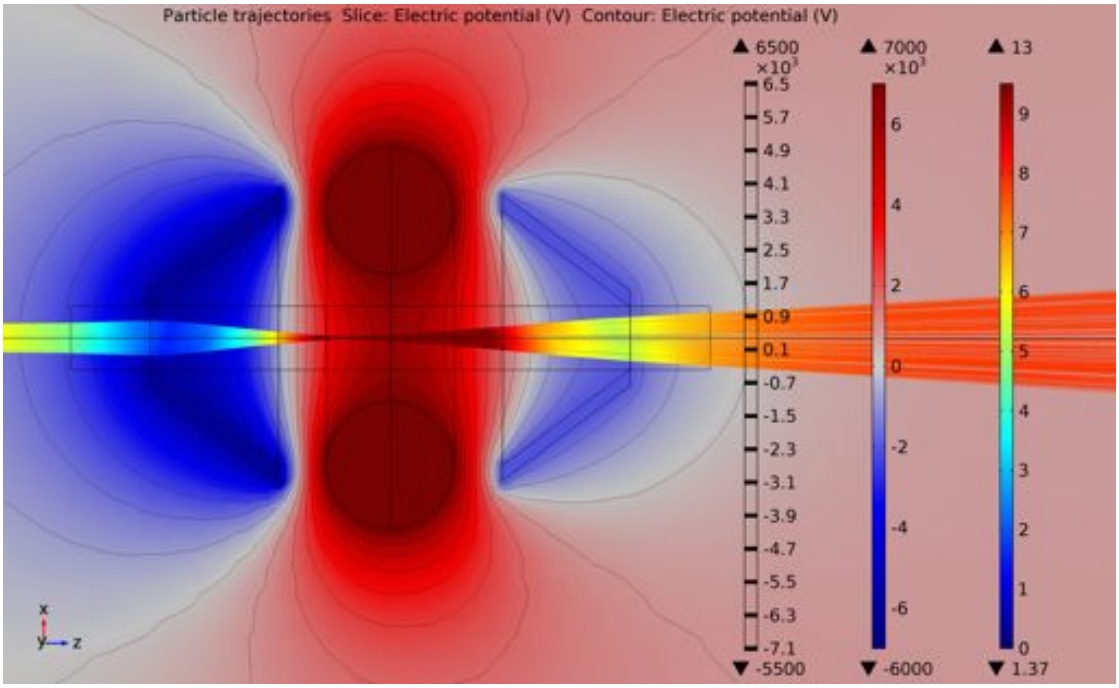

Figure 4.34.: This combined particle trajectory and potential surface plot presents the particle focussing process of the hyperbolic lens system. The particle beam is decelerated in the far field of the lens in front of the first electrode and then enters the focussing region directly behind the opening of the first cone. Behind the focal point, the particles are slightly defocussed due to the third lensing potential and leave the lens afterwards.

the strong positive potential of the torus and allows to adjust the focussing power of the whole lensing system. This is important to exploit the entire sensor area of the detector chip with the projection of the inlet shape as mentioned above. The negative potential of the back cone is approximately one third of the first potential here.

4.4.4. Detecting Part

The only domain of the detection part which has a potential is the backside of the detector sensor layer. This layer is simulated by a rectangular plate with a thickness of 300 µm and a length of 14 mm. Silicon sensors are collecting holes as charge carrier signal so that the backside is supplied with a positive potential between approximately 50 and 150 V. In the simulations of this work, the backside potential is set to 100 V. All of the other parts of the actual detector are ignored in the simulation.

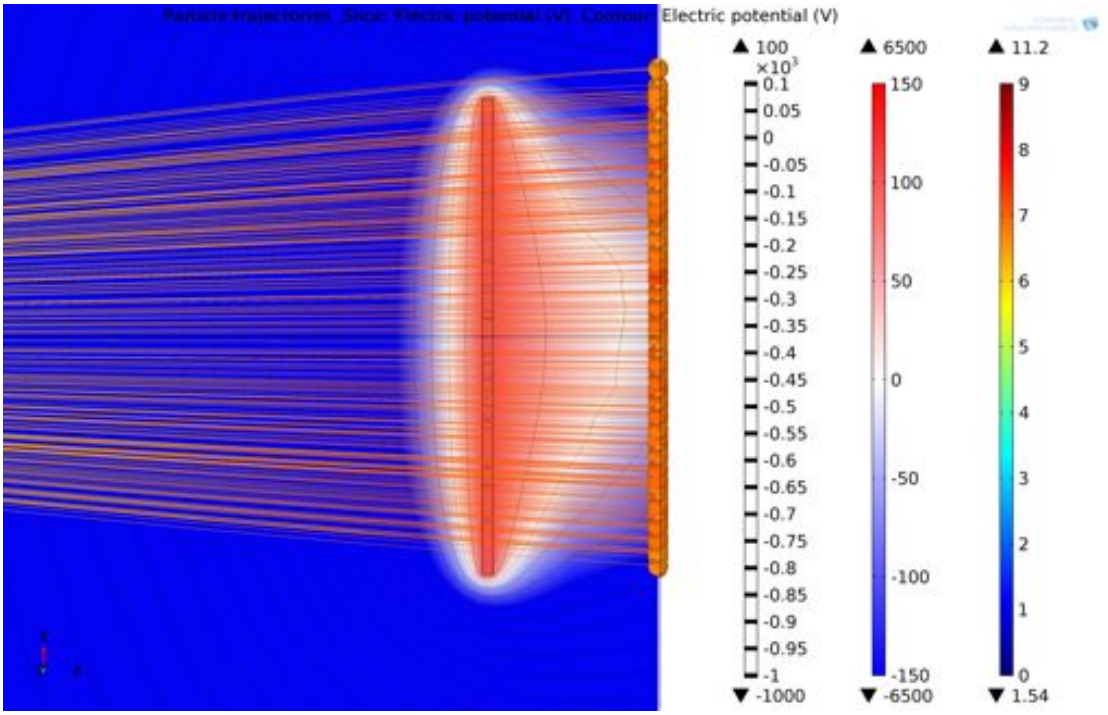

Figure 4.35.: This figure presents a combined particle trajectory and potential surface plot of the detector chip. The potential range is set to a narrow range to set emphasis on the small potential of the sensor backside. The potential cut plane is the zx-plane. The dispersion of the particle trajectories is due to the focussing by the lensing system. The discrepancy between the width of the particle beam and the dimension of the chip surface are due to minor inaccuracies in the electron optics and its potentials.

The distance between lensing system and detector is approximately 60 mm. The detector chip is located in an area which is dominated by the negative potential of the third lens component. Figure 4.35 shows a combined trajectory and potential plot of the detection part. The potential scale is set to a narrow range around 0 V to illustrate the positive potential isle of the sensor in the far field of the lens. The sensor centre is exactly on the optical axis which is illustrated by the black horizontal line.

The imaging process is not perfect. For example, the inlet shape projection at the level of the sensor layer is shifted somewhat to the top so that the topmost particles cannot be detected by the sensor layer. This slight asymmetry is caused if the particle beam is not aligned with the optical axis as soon it enters the lensing system. This, in turn, is the result of a lack in the selector accuracy so that the particle beam is not deflected perfectly. Such imaging errors can be avoided by

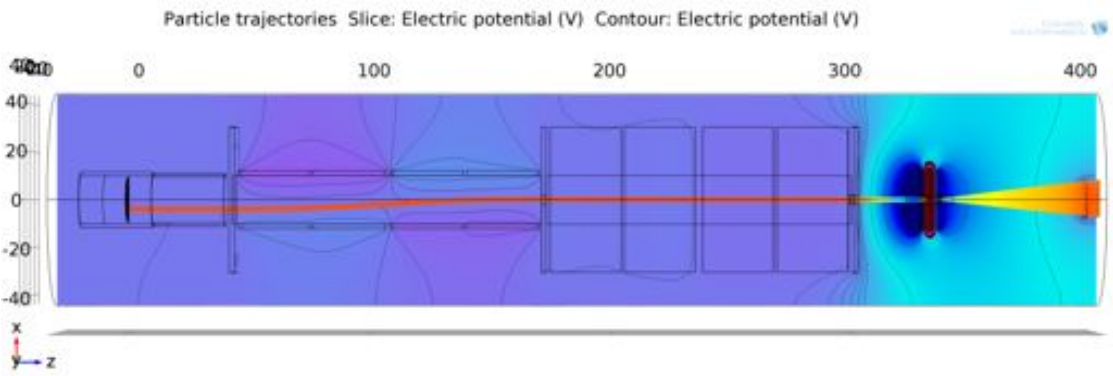

Figure 4.36.: This trajectory plot presents the particle beam pathway through the entire electron optical system including an aperture lensing system (the acceleration part is still missing). The inlet is $(-4, -4)$ and the particle energy is 7 keV. The potential cut plane is a zx-plane with a y-offset of -4 mm. The colour scales are shown in figure 4.37.

setting the selector potentials more precisely. However, this is not realised up to perfection in the simulation due to the large computing time.

4.5. Simulations of the Entire Setup

Up to this point, individual improvements of the four parts of the simulated electron optical system are carried out to achieve a better efficiency of the single parts and therefore a better imaging quality. The next step is to put the parts together and check the functionality of the whole system. In the following figures, this is done without the acceleration part to first take a look on the interaction of the selector and the lensing system.

4.5.1. Basic Simulations with Rhombic Inlet Shapes

Figure 4.36 presents a sideview trajectory plot of the whole simulation. The adjusted selector system is used as well as the aperture lensing system. The particle energy is 7 keV and the electrons are emitted by an adapted particle inlet with an inlet position of $(-4, -4)$. The selector potentials are estimated by equation 4.15 and are adjusted slightly to achieve the proper performance of the realistic selector system. The final values are 330 V, 350 V, 330 V and 340 V for all four selector potentials. The magnification of the lensing system and its distance to the detector are set so that the beam diameter matches the sensor layer surface. The final lensing potentials are -6500 V, $+6500$ V and -3500 V.

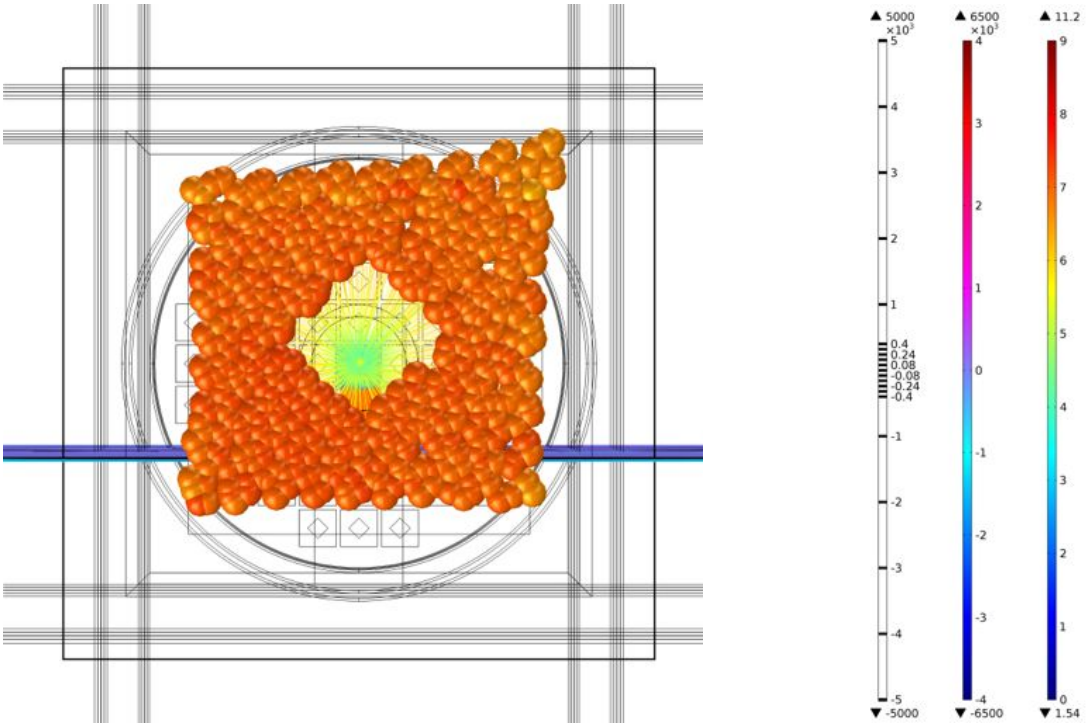

Figure 4.37.: This particle topview corresponds to the simulation presented in´figure 4.36. The position of the projected inlet shape is very close to the plot centre. This confirms the good quality of the selector functionality. Additionally, the edges of the shape are quite sharp indicating a good imaging quality. The upper left tip is explained latter.

The colour scales to the sideview can be found in figure 4.37 on the right. The particle energy is illustrated in a rainbow scale again. The minimum and maximum energy occur in front of the first aperture plate and in the middle of the lensing system respectively. The potential is shown in a so-called disco-colour scale for it is more appropriate to plot the rather small selector potentials all along with the significantly larger lensing potentials.[39] Additionally, the contour lines are also split in two regimes for the strong field gradients and the smaller ones.

In conclusion, the simulation meets the anticipated expectations. The proper deflection of the particle beam onto the optical axis in the selector can be examined by checking the position of the projected inlet shape on the detector chip. Any transversal shift of the particle beam apart from the optical axis is amplified by the magnification effect of the lens resulting in a significant shift of the projection.

[39]Since the lensing potentials are about a factor of 20 larger than the selector potentials, scales with a less pronounced colour gradient have difficulties to illustrate both potential levels in the same plot.

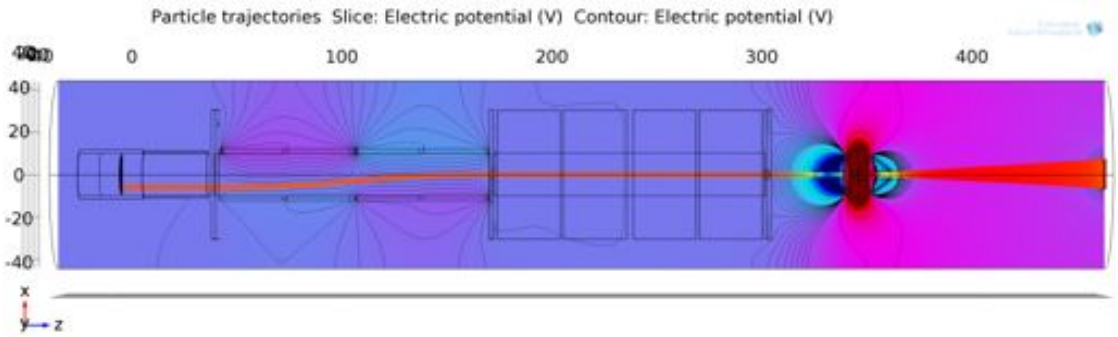

Figure 4.38.: This trajectory plot again shows the particle pathway in the entire simulation but now including an hyperbolic lens system. The inlet is $(-6, -2)$ and the particle energy is 7 keV again. The potential cut plane is a zx-plane with a y-offset of -2 mm. The colour scale are shown in figure 4.39.

The associated trajectory topview is shown in figure 4.37 on the left hand side. The shape is located very close to the centre. Therefore, the selector functionality turned out to be satisfactory.

The projected shape is very similar to the inlet shape shown in figure 4.12. The edges and corners are very straight-lined and sharp – especially in the centre part. As a consequence, the imaging quality is quite good. However, the enlarged tip on the upper right corner raises suspicion. A similar distortion is also found in the case of the hyperbolic lens so that this tip is assumed to be no lensing artefact. A possible explanation for this distortion is given later.

The alternative electron optic simulation including the hyperbolic lens is shown in figure 4.38. Again, the adjusted selector system is used, the particle energy is 7 keV and the electrons are emitted by the adapted particle inlet. However, the inlet position is set to $(-6, -2)$ to prove the functionality with different inlet positions. The final selector potentials are 475 V, 490 V, 155 V and 160 V and the lensing potentials are -6000 V, $+7000$ V and -2000 V here. As in the case of the simulation including the aperture lens, the colour scales can be found in figure 4.39.

There are three differences in the simulation concerning the lens type. On the one hand, the space between lensing system and detector has a positive potential in the case of the hyperbolic lens since the middle electrode is not shielded as efficiently as in the case of the aperture lens. The potential maximum on the optical axis beyond the hyperbolic lens is only about 750 V so that the influence on the fast electrons is not very large. On the other hand, the distance between lens and detector is around a factor 2 larger than in the case of the aperture lens. This is due to the smaller focussing power of the hyperbolic lens which produces less sharp focuses but also less intense imaging aberrations. Finally, the third difference

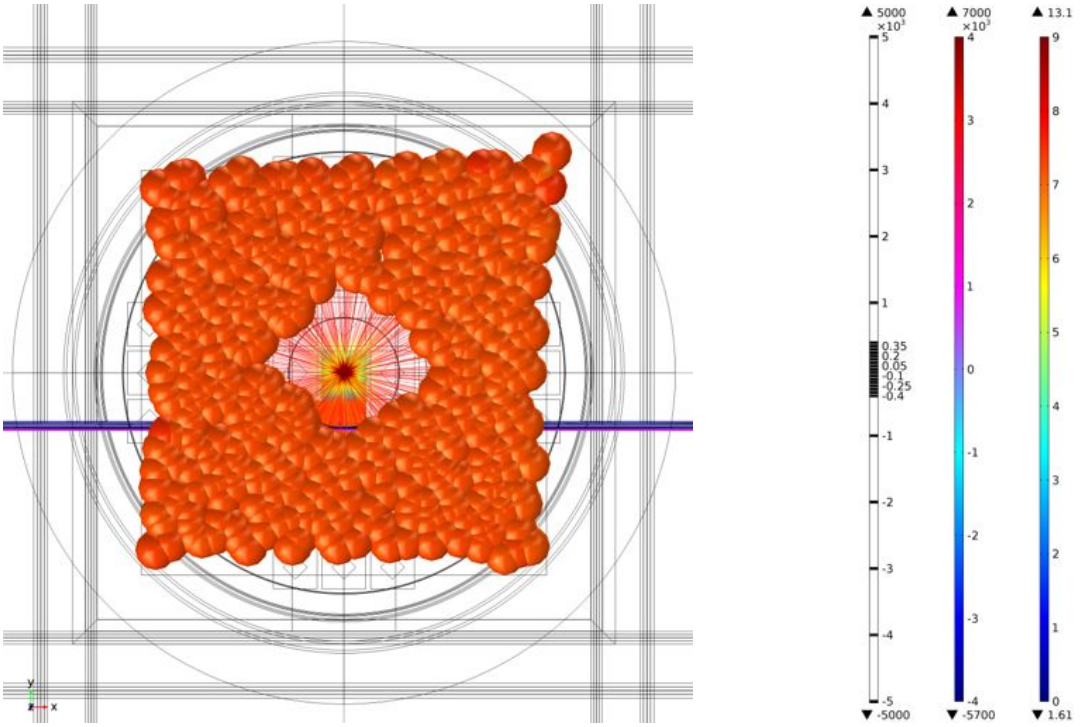

Figure 4.39.: This particle topview is associated with figure 4.38 and confirms the good quality of the selector functionality. Furthermore, the inlet shape can still be recognised easily, however, the edges are less sharp as in the case of the aperture lens. Again, a small tip appears in the upper right corner.

is the minimum energy of the particles inside of the lensing system. The colour scale shows that this energy is 1.63 keV. This value is somewhat higher than in the case of the aperture lens system to meet the strong spherical aberration of the hyperbolic lens, which increases the smaller the particle velocity is inside of the lens system (this observation is already mentioned above).

In this simulation including the hyperbolic lens, the functionality of the electron optics also works well. Additionally, the different location of the particle inlet appears to be no problem for the adjusted selector geometry and potentials. The topview of the projected inlet shape at the level of the detector chip is shown in figure 4.39 on the left hand side. As in the case of the aperture lens system above, the projected shape is very close to the centre and the selector functionality and the imaging quality are both very satisfactory. In contrast to the case of the aperture lens, the edges are a little less straight and the shape seems to be somewhat dented. This is no artefact of the different inlet position but was caused by the different lens type. As a result, the imaging quality of the hyperbolic lens is a little less efficient. However, the upper right tip observed in the aperture lens simulation

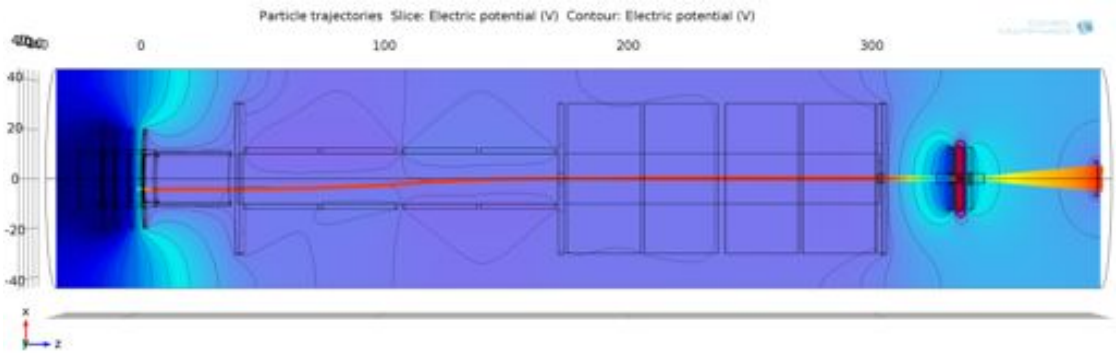

Figure 4.40.: This trajectory plot presents the first simulation of the entire electron optical system including the acceleration part. The inlet shape is based on a simulated $\beta\beta0\nu$-track with an inlet position of $(-4, -4)$. The potential cut plane is a zx-plane with a y-offset of $-4\,\mathrm{mm}$.

is far less obvious as above, although it is still visible here. This might be due to the different field configurations of the two lens types that result in a different focussing impact on particle trajectories less close to the optical axis. In this case, the hyperbolic lens seems to achieve a better imaging quality especially for less symmetric and more complex inlet shapes as one might have to deal with in the case of electron-tracks.

4.5.2. $\beta\beta0\nu$-Simulation

In this section, two new elements were implemented. On the one hand, the inlet shape is changed from the symmetric diamond-like shape used up to now to the simulated $\beta\beta0\nu$-track shown in figure 4.14. This is to examine the imaging quality considering more realistic track-like inlet shapes. On the other hand, the simulation geometry and functionality is completed by finally including the acceleration part so that the particles are released not with 7 kV of energy but with the drift velocity in solid xenon.

Figure 4.40 shows a trajectory and potential sideview of the entire electron optic simulation. The acceleration rings around the PTFE-tube can be seen on the left. The particle are emitted with the saturated drift velocity in solid xenon and accelerated to the kinetic energy of 7 keV. The inlet position is $(-4, -4)$ and the aperture lensing system is used. The colour scales are very similar to the above scales. However, the potential colour range is extended to higher voltages to illustrate the acceleration potentials and less contour lines are shown to avoid too many plot details.

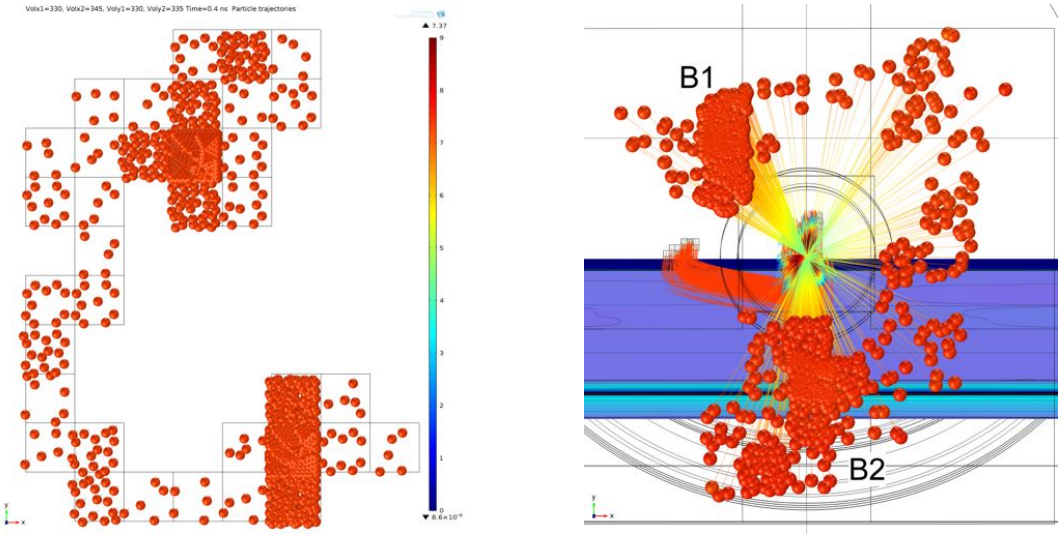

Figure 4.41.: This trajectory topview presents the particles emitted from a $\beta\beta0\nu$-inlet before entering the selector (left) and after being deflected, magnified and projected onto the detector sensor layer (right). The detected shape is inverted due to the focussing of the lensing system. The imaging quality achieved here allows a good recognition of the initial inlet structure.

The associated topview of the simulation can be seen in figure 4.41. The left plot illustrates the inlet shape after 0.3 ns when the particles have just left the acceleration field. The inlet is divided into several small squares that are based on the simulated $\beta\beta0\nu$-track shown in figure 2.7. The side length of each square is 0.2 mm, so that the dimension of the whole track is 2 mm again. The number of particles for the individual inlet squares can be derived from the energy scale of the simulated track since the number of secondary electrons is determined by the deposited energy per pixel.

The right plot shows the projected inlet shape at the detector chip. Due to the focusing effect of the lensing system the inlet shape is inverted.[40] The evaluation of the imaging quality can be done by taking a look on the two Bragg-peaks. The first Bragg-peak (B1) consists of three squares in a row. In the projection, this stripe is clearly recognizable. However, the upper edge point somewhat towards the upper right corner whereas the lower part is slightly shifted. The second Bragg-peak (B2) shows a more complex structure consisting of a strong centre peak surrounded by four diagonally arranged squares with an average electron number. In the projection the single squares can be recognised very well.In conclusion, the imaging quality of more complex inlet structures is quite satisfactory despite minor distortions.

[40]Mathematically spoken, the lens introduces a point reflection around a centre point corresponding to the projection of the optical axis.

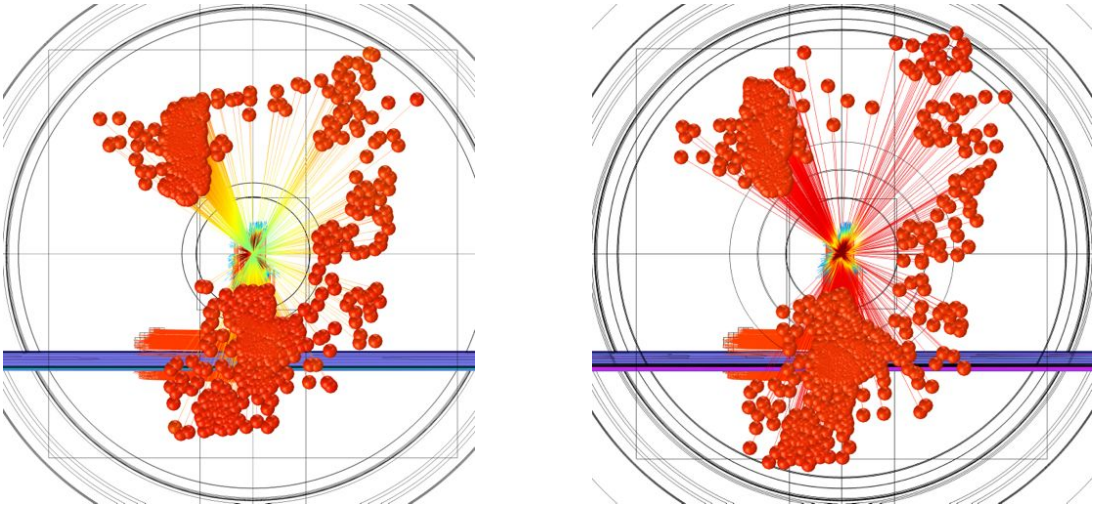

Figure 4.42.: These trajectory topviews present the projected $\beta\beta0\nu$-inlet in the case of a simulation with an aperture lens (left) and a hyperbolic lens (right). The latter plot shows a less proper imaging quality as one can see considering the shape of the Bragg-peaks.

Finally, figure 4.42 shows a comparison of two simulations including the $\beta\beta0\nu$-inlet but with different lens types. The left plot is the same picture of the projected shape as above, the right plot is taken from the very same simulation except that the hyperbolic lens is implemented. It has to be added that the particles within each inlet tile generally are not emitted from the same exact xy-positions since these positions are determined randomly from study to study. Consequently, one has to be careful not to attribute imaging differences to the different lens type which in fact might be caused by shifted inlet positions.

Regarding the imaging quality once again, the Bragg-peaks are much more blurred in the case of the hyperbolic lens. It is quite hard to recognise the square-based structure in the right plot, the $\beta\beta0\nu$-track is subdivided in. For example, it is still possible to tell the centre of lower Bragg-peak (B2) from the lower energetic tiles around it. However, the edges are much more distorted than in the left plot. The rest of the track is quite well-ordered in the case of both lenses. The tip mentioned above seems to become visible again as one can tell by the edges on the top and on the right of the whole structure, which are slightly turned in direction of the upper right corner. This will be explained in the following section.

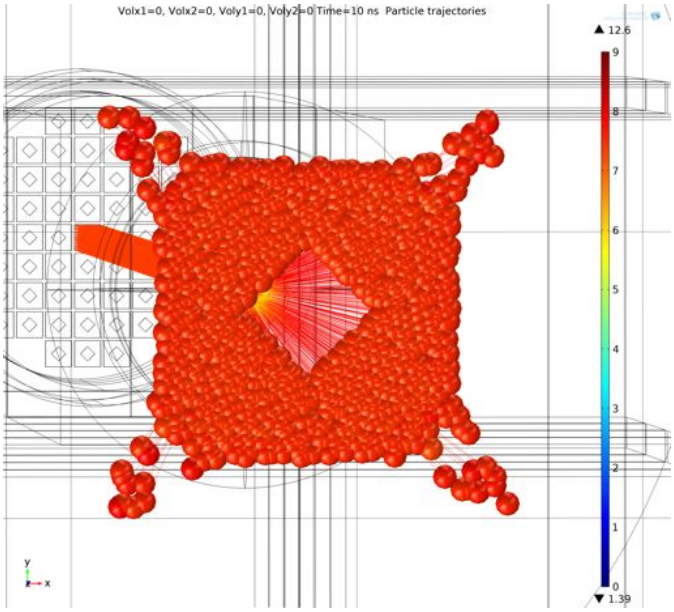

Figure 4.43: The projection of the diamond inlet shape shows obvious signs of the so-called pincushion distortion caused by too low minimum particle energies inside of the lensing system. The inlet position is $(0, 0)$, so no selector potentials are implemented to focus entirely on the imaging errors of the lens. The hyperbolic lens type is used and the lensing potentials are $-6200\,\mathrm{V}$, $+6200\,\mathrm{V}$ and $-2000\,\mathrm{V}$.

4.5.3. Main Imaging Errors

This section takes a closer look on two major imaging errors of the electron optical system – in particular aberration effects of the lensing potentials on the one hand and on the other hand the rhombic distortion of the inlet shape mentioned above.

Figure 4.43 shows one of the most common aberration effects occurred in the simulations of this work: The so-called pincushion distortion. This kind of distortion is caused due to an increase in the deflection strength of electron trajectories with their distance from the optical axis. Regarding the projected image, this results in bowed edges and sharp outer corners. Especially in the case of the hyperbolic lens type, this aberration effect gets quite prominent as soon as the particle energy inside of the lensing system is set to be rather small compared to the particle energy.

To reduce this distortion, the minimum energy inside the lensing system has to be increased by reducing the decelerating potential of the front electrode. However, the potential still has to be strong enough to perform the focussing of the particle beam which results in a trade-off. The final potential values are already implemented in the above simulations (see figure 4.37 or figure 4.39).

The second imaging error is the rhombic distortion, which can be seen in the case of the rectangular diamond-like inlet shape regarding the upper right tip in figure 4.37. A closer look on this topview plot presents a slight tip in the lower left corner as well. Altogether, this can be referred to as rhombic distortion. This imaging error is also found in figure 4.39 and might also explain why the upper and

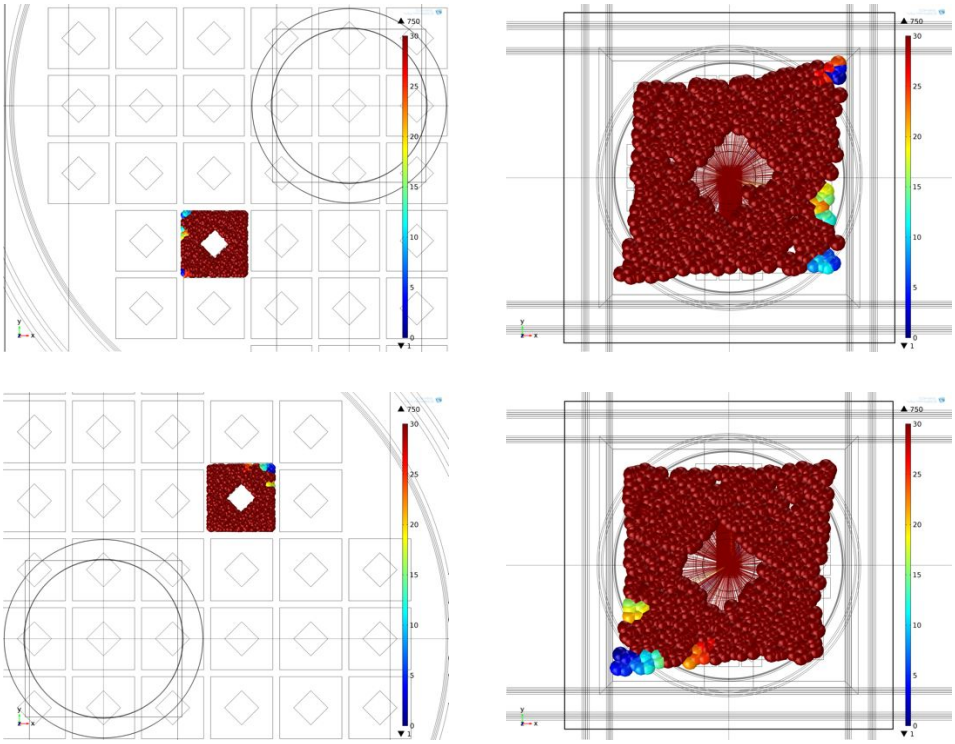

Figure 4.44.: These plots present trajectory topviews at the level of the inlet (left) and of the detector chip (right). The upper inlet position is $(-4, -4)$, the lower one $(+4, +4)$. There is no acceleration part and adapted particle inlet implemented in the simulation so that all particles are emitted with the same energy. The aperture lens type is used. The colour scale illustrates the consecutive number of the single particles to track the specific particles marking the tip back to their initial emission coordinates in the inlet shape.

right edge of the projected $\beta\beta0\nu$-track in figure 4.42 are somewhat turned towards their shared corner.

Apparently, this distortion occurs in multiple cases and circumstances and is no artefact of just one simulation or the specific meshing structure as in the case of figure 4.17. Additionally, the lensing system can be excluded as well, since the rhombus appears with both lensing types. However, as explained above, different lens types might amplify existing distortions differently, which is why the resulting projection on the chip differs with the implemented lens type.

To examine the reason of the rhombic distortion, the acceleration part is turned off as well as the adapted particle inlet so that all particles are emitted with the same energy. The resulting particle topviews in figure 4.44 show two different inlet positions on the left and the corresponding projections on the chip on the right. In the upper plots, the inlet is located at $(-4, -4)$ whereas in the lower plots it

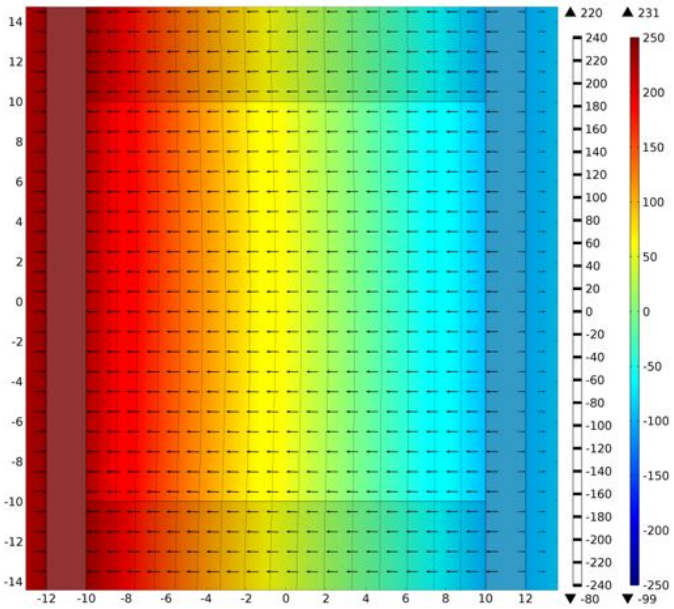

Figure 4.45: This plot shows a potential plot based on a xy-cutplane at the level of the first plate pair of the x-selector. The 0 V-tunnel is shifted to the inlet x-position at +4. The arrows illustrate the strength of the inverted electric field. The middle 20×20 mm are highlighted – a finer mesh size is implemented here.

is $(+4, +4)$. The rhombic distortion is still very obvious which leaves the selector system as the only candidate for the origin of the distortion. The colour scale now indicates the particle index which is the unique consecutive number of each particle in the order of their implementation within the cpt-study. This colour code is used here to track the specific positions of the particles at the upper right corner. Apparently, the particles marking the tip originate from the very part of the inlet shape which has the largest distance to the central optical axis. This assumption is confirmed by further simulations with different inlet positions.

According to these observations, the distortion is created in the selector system especially affecting particles emitted far away from the optical axis. The trajectories of such particles leads them close to the negative potential plates of the selector. Figure 4.45 shows a xy-potential-cutplane located at the level of the first plate pair of the x-selector. The highlighted middle part is created by the additional vacuum domains in the selector system which allows to introduce a finer mesh size in this part. The asymmetric potential surface is due to the adjusted selector. The inlet is at $(+4, +4)$ so that the 0 V-tunnel in green is located at $x = +4$ mm. The field arrows are inverted again. The grey contour lines are the key part of this plot. Apparently, the equipotential lines are not parallel to the plates or to each other – not even in the middle part of the selector plates. Consequently, the electric field consists not only of a x-component inside of the x-selector as it is assumed in the mathematical approach to the selector potentials. This means that the electrons experience a slight deflection into y-direction whilst crossing the electric field of the x-selector.

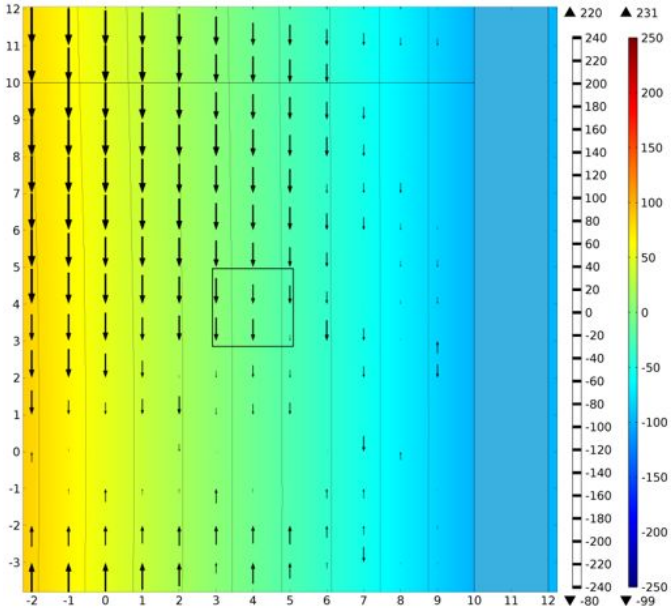

Figure 4.46: This plot shows a zoom into figure 4.45. Only the y-component of the electric field is plotted here. The position of the inlet shape is illustrated by its contour at $(+4, +4)$. Apparently, the y-field varies within the inlet shape causing different deflection strengths among the electrons in negative y-direction.

For a better illustration of this fact, figure 4.46 shows only the inverted y-component of the electric field.[41] The inlet is located at $(+4, +4)$ and its contour is drawn around this position. The plot shows that the y-component of the electrostatic force inside of the x-selector varies within the inlet shape. This means that the single electrons experience a different yet small deflection in y-direction. Furthermore, the y-component of the field gets larger with increasing distance to the negative potential plate. In the case of figure 4.46, this results in a slightly larger deflection in negative y-direction of the left part of the electron beam which consequently is tilted as in a paralellogram.

The very same effect occurs in the y-selector as well. However, it is somewhat smaller here since the particles enter the y-selector at the $x = 0$-plane. This plane can be seen as convergence zone of the transversal field, as one can see at $y = 0$ in figure 4.46 and the transversal field components are quite small.[42] Both sub-selectors cause a paralellogram-like deflection of the inlet shape. As a result, the two neighboured edges of the inlet shape which face the negative potential plates of the two sub-selectors, are deflected less strongly than the other

[41] The length of the arrows corresponds to the field strength. It is plotted logarithmically and a range quotient and a scale factor are introduced for a better visualisation. Therefore, the absolute values of the field strengths are difficult to be specified in a colour scale. Only the difference of the impact of the electric field onto different parts of the inlet shape is of interest so that the absolute values can be left unconsidered.

[42] In the figure, the difference between the y-field component at $y = 0$ and $y = 4$ seems to be rather large. This is mainly due to the logarithmically plotted arrow lengths. In fact, the y-field in the x-selector definitely is large enough to also cause a transversal deflection.

two edges. Both transversal deflections adds up in the shared corner of these two edges and this very corner marks also the specific bunch of electrons emitted with the largest distance to the optical axis. Consequently, the observed tip and hence the rhombic distortion can be explained by transversal deflection effects in the individual sub-selectors. Furthermore, due to the lower influence (not larger) of these transversal field components on the electrons of the tip, it is more truthful to consider the tip as the original position of the inlet shape and to regard the rest of the shape to be distorted instead of the other way round.

Another observation might be explained along this argumentation as well. In the case of an identical x- and y-position of the inlet shape, the potential values of the sub-selector are not equal despite of their identical geometry. This is mentioned for example in the beginning of this section, for example. Considering the small y-field inside of the x-selector, the potentials of the y-selector can be reduced slightly since a little part of the y-deflection is already done. In the other way, the x-deflection in the y-selector is somewhat smaller due to the mentioned convergence zone of the transversal field at $x = 0$. The potentials of the x-selector compensate that difference with a slightly larger field strength.

4.6. CAD drafts of the Setup

The simulations presented presented up to this point have aimed at the principle of the electron optical system and the optimization of the single components. In this section, CAD drafts of a possible, real experimental setup based on the the simulated geometry are shown. The drafts are drawn with Autodesk Inventor 2013. There are two main challenges: On the one hand the construction of a structure to arrange the single electrodes of each electron optical component relative to each other; On the other hand the design of a vacuum vessel for the whole setup has to be performed as well as the implementation of the vessels in the simulation.

4.6.1. Fixation Structure

The single electrodes and potential plates of the four electron optical parts are defined by a certain position, shape and dimensions within the simulations. In reality however, these components need to be attached to a wider fixation structure to connect them to each other. This structure has to keep the single components in place and prevent potential breakdowns. Additionally, it has to be attached to the outer vacuum vessels which will arrange the single parts to form the actual electron optical system.

One example for such a structure is the CAD draft of the lensing system presented in figure 4.47. The view is a so-called three-quarter-view that allows to cut the

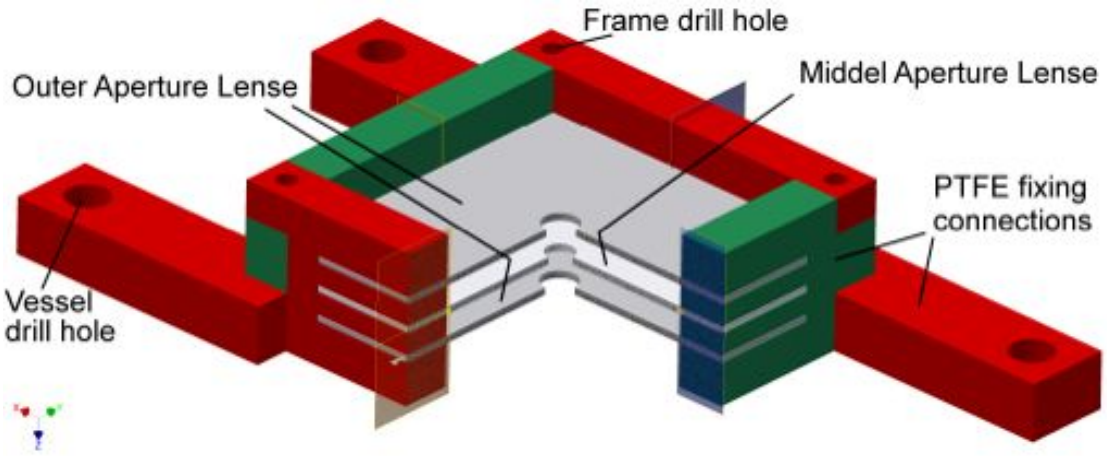

Figure 4.47.: This CAD draft shows the lensing system consisting of three aperture plates enclosed by PTFE frame segments. The segments are equipped with interlocking laps at each side and a drilled hole through these laps to allow a screwed fixation of the single frame segments. The positioning of the aperture plates within the frame is achieved by additional metal noses at each side of the plates and corresponding slots in the frame segments.

draft and to only show three quarters of it in order to provide a better sight on the inside parts. The aperture lens type is drawn here with the lensing plates being marked in grey.[43] The three plates are enclosed by a fixation structure, consisting of four frame segments that are assembled perpendicularly so that each frame segment faces one of the four edge sides of the lensing plates. The frame segments are coloured in red and green to make them distinguishable in the drafts. They are intended to be fabricated out of PTFE for isolation purposes due to the different potentials of the individual aperture plates.

The plates are equipped with noses at each edge with a height of several millimetres. In contrast, each frame segment has three slots with the same dimensions as the plate noses to fix theses noses and hence the aperture plates. In figure 4.47, the outer surface of the noses can be seen pointing out of the slots on the side edges of the frame segments. To connect the frame segments, they are also equipped with noses and slots at their corners. Figure 4.47 for example shows this fixation at the left and right corner, where the green frame segment noses are enclosed by the sidelaps of the red frame segments. At these corners, a hole is drilled right through all frame segments so that they can be fixated with screws to form the final fixation structure enclosing the aperture plates and completing the lensing system.

[43] In contrast to the previous simulations, the inner diameter of the middle lens is smaller than that of the other two aperture plates.

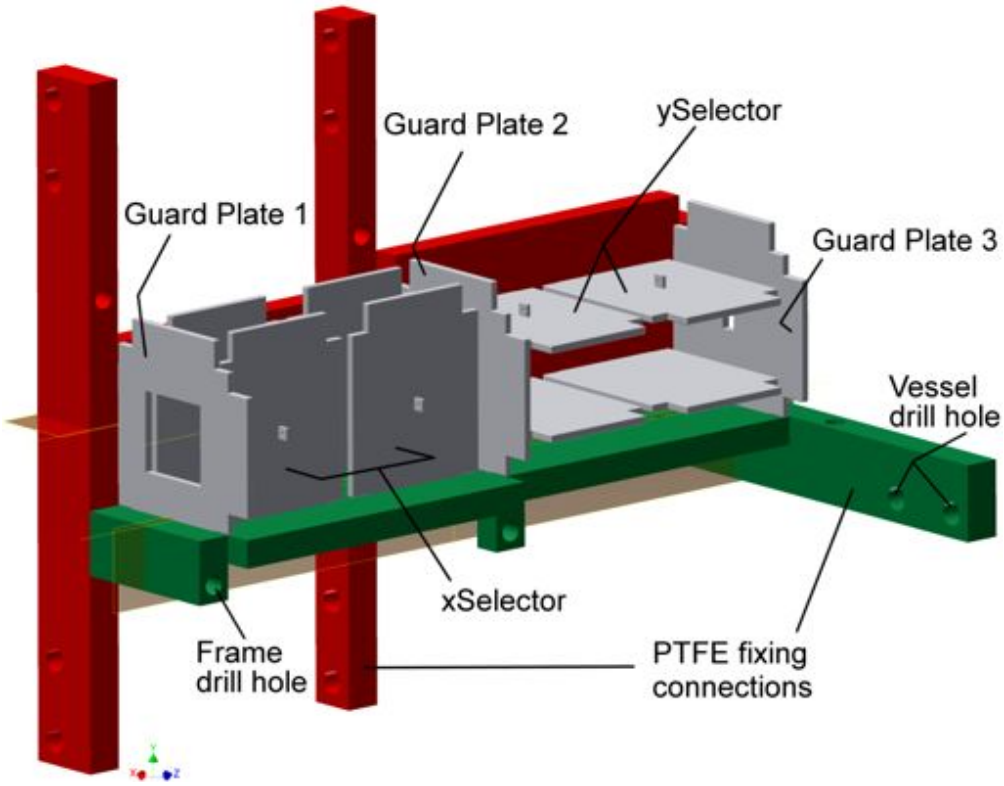

Figure 4.48.: This CAD draft shows the selector system consisting of three guard plates and two times four potential plates, which are enclosed by four PTFE frame segments. Again, there are interlocking laps and drilled holes at each side of the segments and additionally in their middle. All selector plates are equipped with noses to be attached to the corresponding slots in the frame segments. In this draft, one also can see small loops on the side of the potential plates that serve as connecting pins to the high voltage.

Another example is the draft of the selector system shown in figure 4.48. As above, each potential and guard plate is equipped with noses on their sides.[44] There are four frame segments again that are arranged perpendicularly. Nevertheless, the draft only shows two of them to provide a look to the assembly inside of the frame. As one can see, the primitive selector design is drawn here so that there are only two plate pairs per sub-selector.[45]

The potential and guard plates are assembled as presented in figure 4.20. For example, the distance between one guard plate and one potential plate is half of

[44] In contrast to the aperture plates and the selector guard plates, the potential plates have only two noses on two opposing edges.

[45] Their side length is 40 mm in the CAD draft.

the distance K between two potential plates. Besides that, one can see that the rectangular particle window in the third guard plate is much smaller than in the first guard plate. All of the selector plates are equipped with small metal loops for the potential supply. Additionally, there are small holes in the frame segments (which cannot be seen in the draft) that will serve as feedthrough of the power wires to the selector plates. The fixation of the selector plates is done with slots in the frame segments again. There are seven slots for each frame segment: Three crosswise slots for the guard plates and four lengthwise slots for the corresponding sub-selector potential plates. Furthermore, there are drill holes at the ends and in the middle of the single frame segments to connect them by using screws to construct the entire enclosing selector frame.

At last the selector and the lensing system has to be embedded in a vacuum vessel construction. There are two vessels for the selector, one vessel for the lens and a third vessel for the detecting system. The individual vessels have to be connected carefully since the attached electron optic parts need to be aligned at the optical axis very precisely. Figure 4.49 shows the entire CAD draft including the vacuum vessels shown in grey. ISO-K vacuum components are used for the vessels, which are connected via orange centering rings. In reality, these rings are surrounded by rubber belts for the tightening of the vacuum. The electron source (which in the end will be the detector crystal) is connected to the left end but not shown in this draft. At the right end, a CF-vacuum feedthrough is added to extract the signal cables of the Timepix detector to the external data computer. At the cylindrical surfaces of the vessels, many small KF flanges can be seen which will serve as potential feedthrough for the enclosed potential plates.[46]

Inside of the vacuum vessels one can see the selector and lens frame parts in red and green which in turn contain the potential, guard and aperture plates. Again, the draft shows a three quarter view of the entire electron optic and vacuum system so that some plates and frame segments appear to be cut in half in their middle. The fixation of the frame segments to the vessels can be done in two ways which both are based upon steel bridges at the level of the vacuum flanges. In the case of the right end of the selector system, parallel bridges from one side of the flange to the other side can be seen whereas in the case of the lensing vessel, a ring-like jut is applied. Such bridges can be equipped with either drill holes or grub screws. Before connecting the vacuum vessels, the entire selector and the lensing frames are positioned inside of their corresponding vessel parts. All of the frame segments are equipped with vessel drill holes as one can see in figures 4.47 and 4.48. These drill

[46]The flange dimensions used in this draft are the ISO-K 200 standard for the vessels, the KF 16 standard for the voltage feedthrough and the CF 63 standard for the feedthrough of the Timepix signal cable.

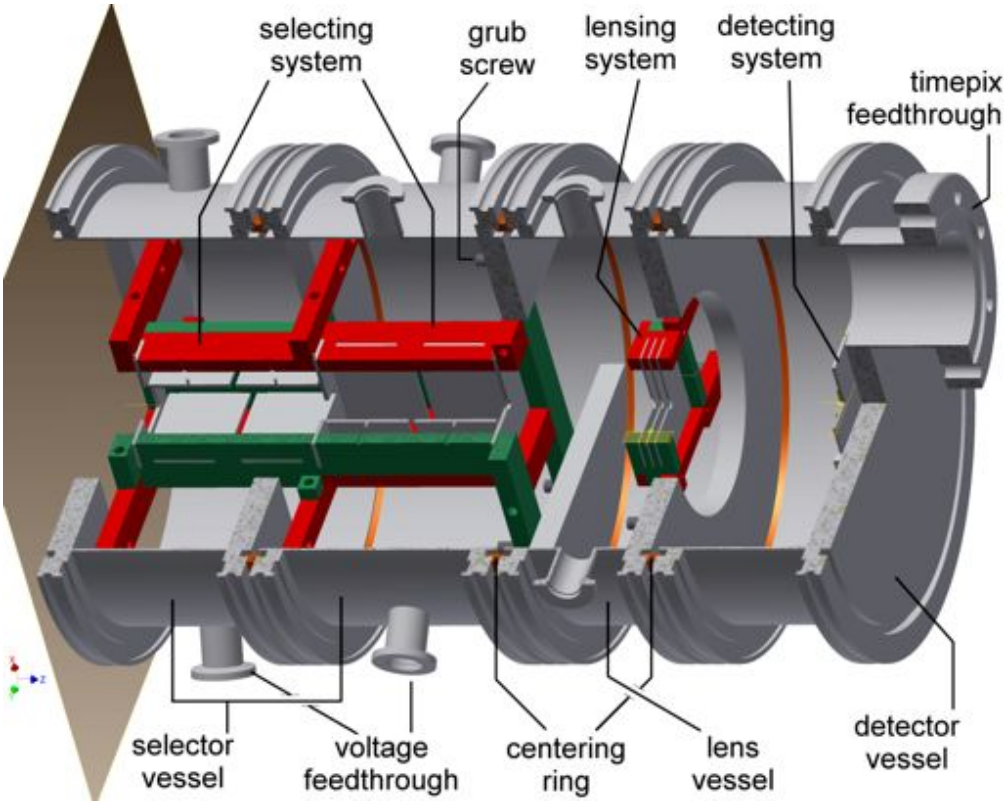

Figure 4.49.: This CAD draft shows the entire electron optical system attached to four surrounding vacuum vessels. These vessels are connected by centering rings and equipped with several flanges for voltage and signal cable feedthroughs. The frames of the electron optic components are fixated via grub screws. All connections need to be done carefully since the potential plates have to be aligned precisely around the optical axis.

holes of the frame segments are aligned with the drill holes of the vacuum vessels or are engaged with the grub screws depending on the type of fixation. Afterwards, the frames can be placed by additional screws in the case of drill holes or by nuts in the case of grub screws. In the CAD drafts of this work, both types are introduced depending on the position of the flange bridges according to the frame segments.

In this way, the selector and lensing system is connected to the vessel parts which afterwards can be connected to establish the whole electron optical system surrounded by a vacuum chamber.

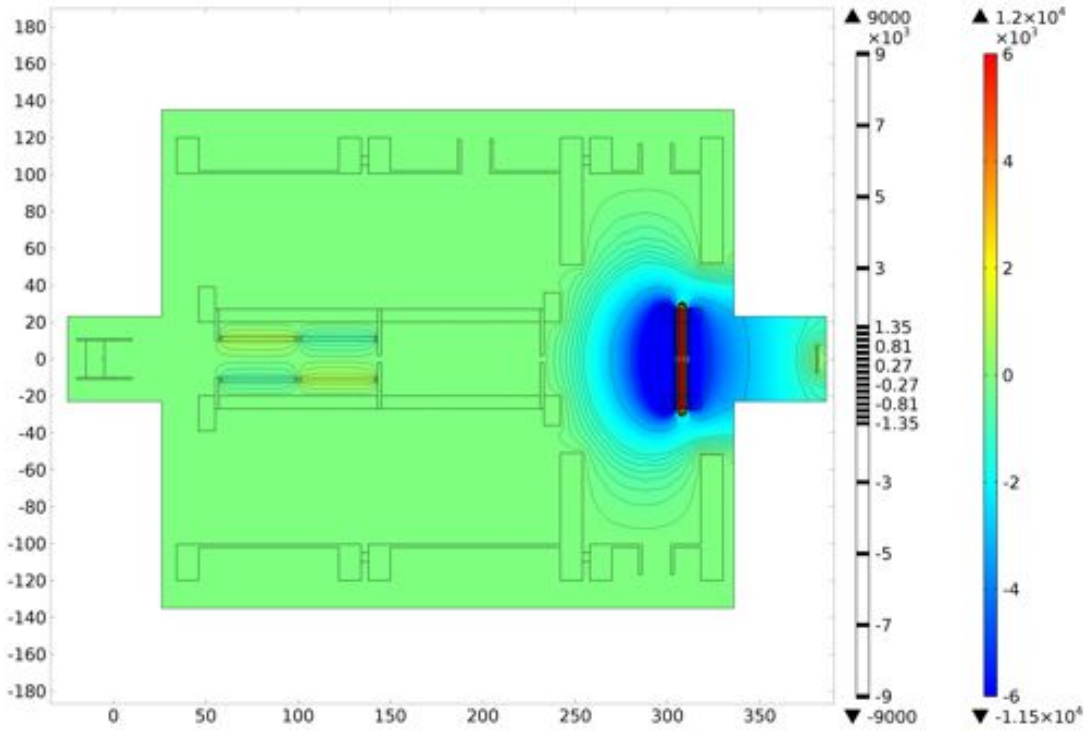

Figure 4.50.: This potential plot shows the simulated CAD design including vacuum vessels and PTFE frame segments. Only the selector and the lensing vessels are presented. The inlet position is $(-4, -4)$. The original selector without adjustment and the aperture lens system is used. The equipotential lines are deformed due to the edges of the grounded vessels and isolating frame segments.

4.6.2. Simulation of Vacuum Vessels

The next step is to re-simulate the entire electron optic including the vacuum vessels presented above. Since vacuum vessels are grounded, they act as potential plates with $V = 0\,\mathrm{V}$. It is advisable to simulate the whole CAD setup in order to check whether there is an influence of the vessel potential onto the functionality of the electron optic or not.

Figure 4.50 shows a potential surface plot of the simulated CAD setup excluding the detector vessel to reduce the computing time. The original particle inlet is used here consisting of a xenon crystal and a particle inlet matrix enclosed by a PTFE tube. The plot presents a cut view through the selector and lensing frame as well as the potential plates of both systems as seen previously. The inlet position is $(-4, -4)$. The preliminary selector design without any adjustments is still used here. The vacuum vessels are simplified to a great extend to avoid a massive increase in computing time. This means that the KF potential feedthrough

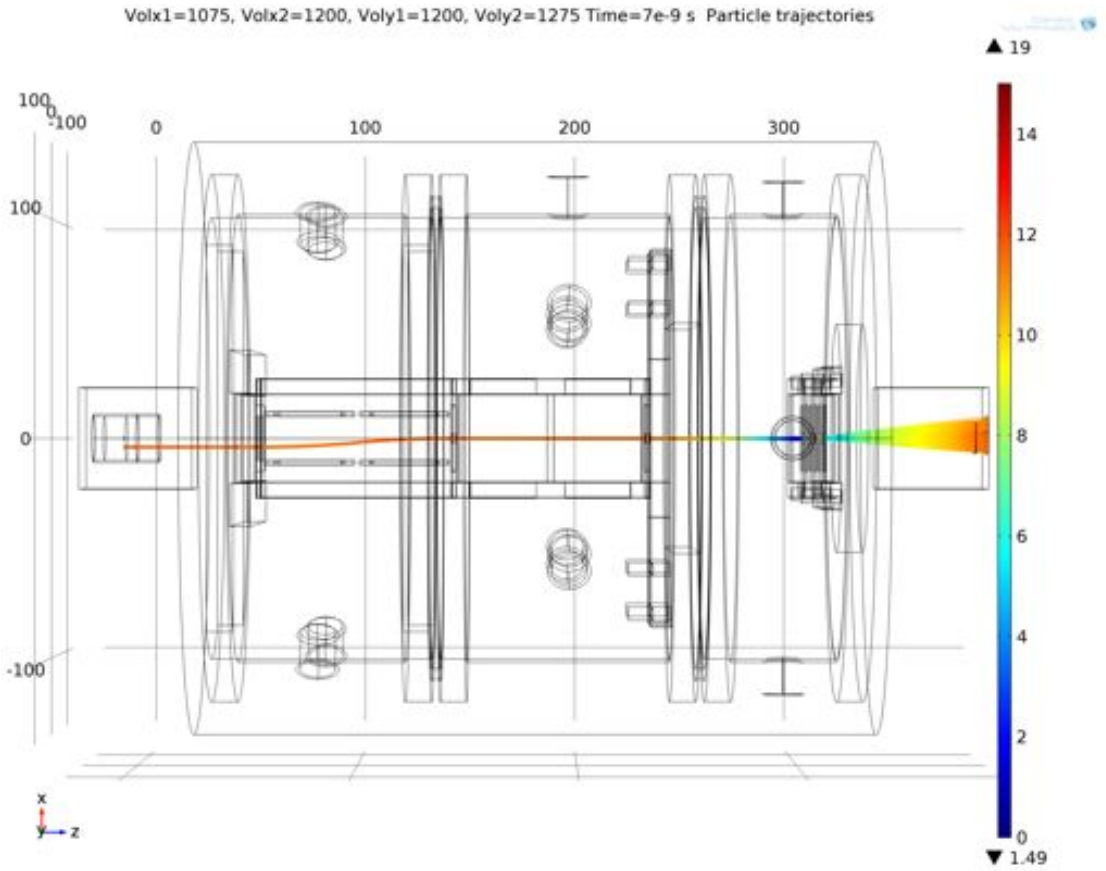

Figure 4.51.: This trajectory plot shows the particle beam based on the simulated CAD design including vacuum vessels and PTFE frame segments. The vacuum vessels are highly simplified to reduce the computing time. The deflection and focussing of the particle beam leads to a satisfying and centred magnification of the inlet shape at the level of the chip.

flanges are approximated by simple tubes and ISO-K flanges by circular rings with the same dimension as the actual flange but without any grooves. The plot also shows the steel bridges of the flanges, which are necessary for the fixation of the electron optical frame segments. The PTFE fixing connections of the frame segments containing the vessel drill holes are located outside of the given cut plane.

The contour line scale is divided in two parts again, to illustrate the strong lensing potentials as well as the rather low selector potentials in the same plot. The vessels and the frame segments are kept at 0 V causing a deformation of the equipotential lines at the edges of the vessels. The most interesting area close to the optical axis looks very similar to the simulations without vacuum vessels so that no major influences of the vessel potentials onto the electron beam are

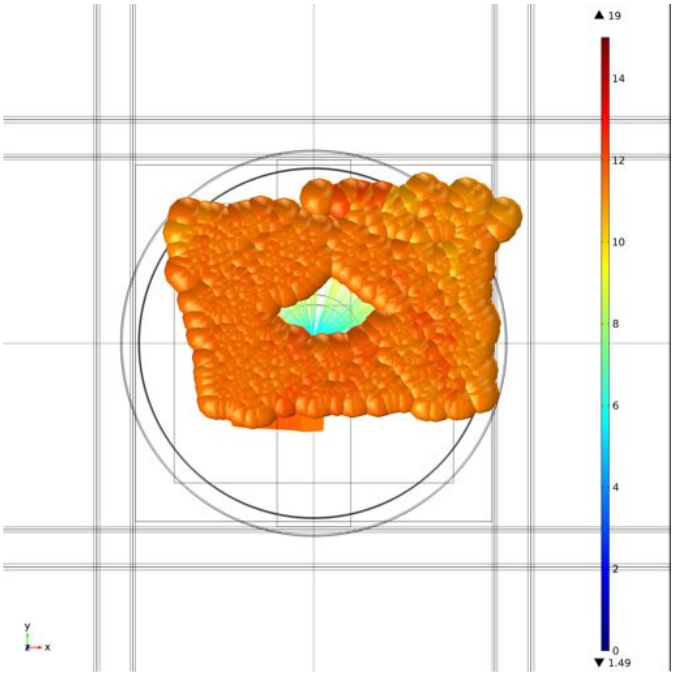

Figure 4.52: Trajectory plot of the magnified inlet shape at the level of the detector in the case of the vacuum vessel simulation. The preliminary selector design without fine-tuning is still implemented here causing a bad image quality compared to the image shape plots presented in section 4.5.

supposed to occur. Consequently, the potentials applied to the selector plates are very similar to earlier simulations without vacuum vessels.

The resulting trajectory plot corresponding to the potential distribution shown above is presented in figure 4.51. The x-selector plates can be seen in a sideview whereas the y-selector plates are shown from the top including their edge noses connecting them to the outer frame segments. At about $z = 230$, the grub screws for the connection of the right end of the selector frame to the vacuum vessel are illustrated. The deflection process in the selector system is quite effective leading to a successful projection of the inlet shape onto the optical axis. The magnified inlet shape at the level of the detector is presented in figure 4.52. The shape is quite distorted since no fine-tuning adjustments to the selector system are already implemented here. In principle however, the deflection of the electron beam in the selector and the focussing in the lens system are quite satisfactory.

As a conclusion, the influence of the vacuum vessels on the electron optics tends to be negligible. Nevertheless, it is important that no metal pieces or connection bridges extend into the area near the optical axis as it is realised in these drafts.

5. First Experiments with Solid Krypton

Contents

5.1. Experimental Goals

Several experiments have to be accomplished on the way to the far-end goal which is to do tracking experiments with a solid xenon sensor and a Timepix detector. The basics about the design and the detection properties of solid xenon and krypton are explained in chapter 3. The first experiments are done with krypton instead of xenon due to its lower costs. A scheme of the principal design is shown in figure 3.1 and the design including the electron optical system is explained in chapter 4. In the simulated setup, electrons are supposed to be extracted from the sensor material, accelerated, deflected and magnified by the electron optical components and finally projected onto a Timepix detector. The acceleration is necessary due to the signal threshold of the Timepix detector: Arriving electrons need to have at least about $6 - 7\,\mathrm{kV}$ to generate enough electron-hole-pairs in the sensor to be detected.

In this chapter, the first test run to grow rare gas solids (RGS) in a vacuum chamber is presented. In contrast to chapter 4, the future goal is to use a Timepix

detector without sensor layer and to use the RGS itself as sensitive volume. The ASIC is to be connected directly to the RGS, which therefore replaces the sensitive volume of the Timepix detector. The charge pulse is supposed to be generated in the same way as if the sensor was applied, which means that the drift movement of the charge carriers in the sensitive volume induce a current in the ASIC electrodes (see also section 3.3). The excellent electron mobility properties of RGS are supposed to allow such tracking applications but it has not been examined so far. Therefore, this experiment is a proof-of-principle experiment, whether a signal readout from solid krypton with a naked Timepix ASIC is possible of not. In this thesis, however, only the growth of a RGS in a vacuum vessel is presented for this is the state of the are achieved so far within this experiment.

5.2. Basic Design and Setup Components

5.2.1. Setup Overview

In order to grow large krypton crystals in a vacuum chamber, the experimental design requires a cooling tip in an evacuated growth chamber and an inlet valve for the krypton gas. As soon as the cooling tip drops below the melting temperature of krypton, a crystal starts to grow as long as there is enough gas inflow. Furthermore, several additional instrumental details are necessary in the actual experiment to fully control the crystal growth. Figure 5.1 shows a scheme of the setup to provide an overview of the basic experimental systems which are described in this section.

Prior to the crystal growth, the chamber has to be evacuated so that a vacuum system is necessary. Otherwise, oxygen and carbohydrates from the air would contaminate the krypton and reduce the possible drift distance of charge carriers in the krypton crystal.[1] The vacuum system consists of the pump and several vessels including the growth chamber.

On the bottom of the vessels, a cooling tip leads inside this chamber. To start the crystallisation process, the cooling tip need to be cooled down to temperatures beyond the melting point of krypton. Such temperatures can be achieved easily by liquid nitrogen cooling since its temperature ($T_{\mathrm{LN}} = 77\,\mathrm{K}$) is far below the melting point of krypton ($T_{\mathrm{sKr}} = 117\,\mathrm{K}$).[2] To connect the inside of the growth chamber thermally to the liquid nitrogen reservoir on the outside, a feedthrough for the cooling tip into the vacuum vessel is required.

To isolate the vacuum vessels from the cooling finger, a thermal isolation between the growth chamber and the rest of the setup is necessary. This is because the cooling tip is the only component that is supposed to be cooled down whereas all

[1] See the impurity part in RGS in section 3.2.
[2] See table A.1.

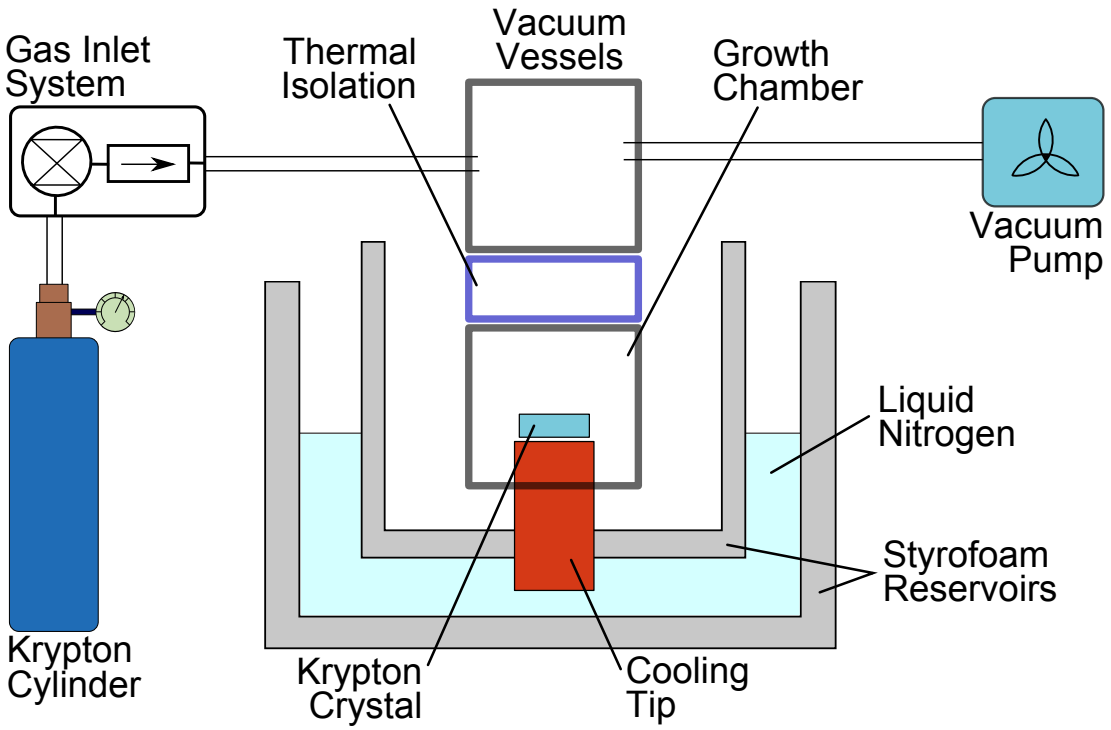

Figure 5.1.: Basic overview of the experimental setup. A small Styrofoam container is located inside of a bigger reservoir that contains liquid nitrogen. A cooling tip applied at the bottom of the growth chamber vacuum vessel passes through the inner reservoir and hence, it is thermally linked to the nitrogen outside. The growth chamber is thermally isolated from the rest of the vacuum system. A vacuum pump is connected as well as the inlet valve of the krypton cylinder. The krypton freezing is supposed to start at the cooling tip.

other vacuum vessels should remain at higher temperatures so that the crystal growth solely is maintained by the cooling tip. Otherwise the crystal growth would be triggered from every side of the growth chamber and the resulting crystal would be rather inhomogeneous.

The krypton required for the RGS is taken from a high pressurise gas cylinder with up to 80 bar. However, the vacuum vessels resist only small pressures exceeding 1 bar since they are designed for vacuum pressures. Consequently, a gas inlet system is necessary to regulate the gas inflow and pressure in the vacuum system including the growth chamber. Beforehand this system has to be evacuated as well to avoid any major contamination of the krypton.

Figure 5.2 presents a picture of the entire setup. On the right, the Styrofoam containers can be seen acts as liquid nitrogen reservoir. Inside, a second container houses the growth chamber. This vacuum system also includes a cross tube, whcih

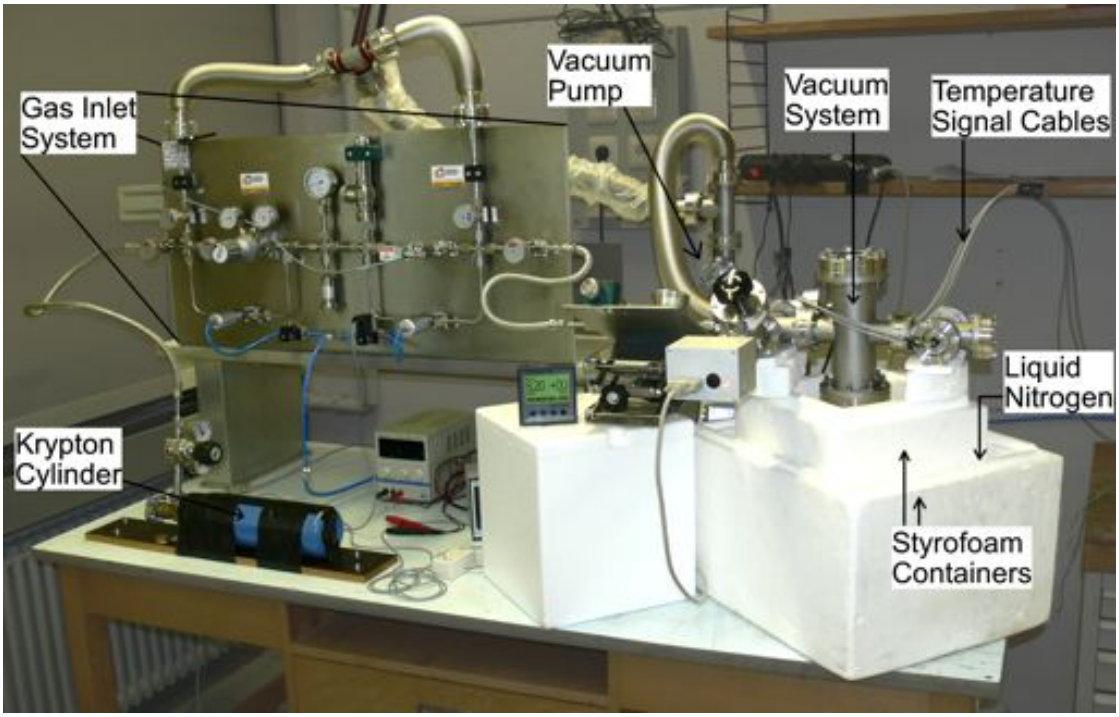

Figure 5.2.: This picture presents the entire experimental setup consisting of the vacuum system including the growth chamber, the cooling system realised by Styrofoam containers filled with liquid nitrogen and the gas inlet system that connects the high pressure krypton cylinder with the vacuum system.

can be seen above of the Styrofoam containers. A feedthrough to several resistance temperature detectors (RTD) inside the chamber can be seen on its right and at its left, the vacuum gauge is attached as well as the inlet system and the vacuum pump is located behind the containers. The gas inlet system is placed left to the vacuum system. It connects the cross tube with the krypton cylinder at the bottom. To evacuate the gas inlet system, it is connected to the vacuum pump on its top as well. In the following, the individual components of the setup are explained in detail.

5.2.2. Vacuum System

The vacuum system is presented in figure 5.3 with the big cross tube as its centre piece. On the bottom, the cross tube, which is located inside of the inner Styrofoam container, is attached to the growth chamber. On the top of the cross tube a vacuum glass allows a direct view inside the growth chamber. The cross tube integrates several connection flanges, e.g. the feedthrough flange on its right for

the RTDs cables. Other feedthrough flanges will serve as readout connection of the Timepix detector in future. Left of the cross tube, the vacuum pump is connected at the back and to the vacuum gauge at the front.[3] The vacuum pump in this experiment consists of a turbo-molecular pump and a dry compressing backing pump with an attainable ultimate pressure range of 10^{-7} mbar.[4] At the far left, the gas inlet connection acts as intermediate part between the vacuum system and the gas inlet system. It contains a safety relieve valve, which is triggered, if the pressure in the vacuum system exceeds 3 bar for safety reasons and to avoid damage of the vacuum chamber.

One important comment has to be made concerning the functionality of the vacuum gauge. In figure 5.3, the krypton pressure in the growth chamber is set to be 1 bar whereas the vacuum gauge displays a pressure of $6.2 \cdot 10^{+0}$ mbar. The reason for this discrepancy is the pressure measurement method of the gauge – the so-called Pirani-principle. Pirani-gauges determine the vacuum pressure based on the thermal conductivity of the medium inside of the vacuum vessels, which is pressure-dependent. However, the thermal conductivity also depends on the molecular mass of the atmosphere inside of the vacuum vessel. Pirani-gauges are usually calibrated for nitrogen-based environments (i.e. air). The molecular mass of krypton atoms is about three times higher than that of nitrogen so that wrong values for the pressure in the growth chamber are measured by the Pirani-gauge.

Figure 5.4 shows a conversion plot for different gases for a specific Pirani-gauge.[5] The measured pressure is assigned to the x-axis and the real pressure to the y-axis. The N_2-line is the only straight curve within the plot indicating that the corresponding Pirani-gauge is calibrated for air-environments. Depending on the molecular or atomic mass, the real pressure tends to be smaller or – as in the case of krypton – larger than the measured pressure. After the krypton entered the growth chamber, the pressure measured is $6.2 \cdot 10^{+0}$ mbar $\approx 6 \cdot 10^{+2}$ Pa. According to figure 5.4, this value has no corresponding real pressure in the case of krypton. The reason for that is the poor performance of Pirani-gauges as soon as they are exposed to pressures of the order of 10^{+2} mbar and above. Consequently, the real pressure is quite close to 1 atm as expected. According to the conversion plot, a good estimation of the real pressure is possible especially for $p \sim \mathcal{O}(10^{-1}\,\text{mbar})$ and below.

[3] The display shows the pressure inside of the vacuum system in mbar.

[4] The vacuum pump used in the setup was the turbomolecular pump system TURBOLAB 80 from œrlikon. The maximum pumping speed is 60 l/s.

[5] Such conversion plots differ slightly depending of the specific Pirani-gauge used for pressure measurements. However, the discrepancy is rather small and since no conversion plots including krypton are available for the used Pirani-gauge, this plot is used to explain the problem.

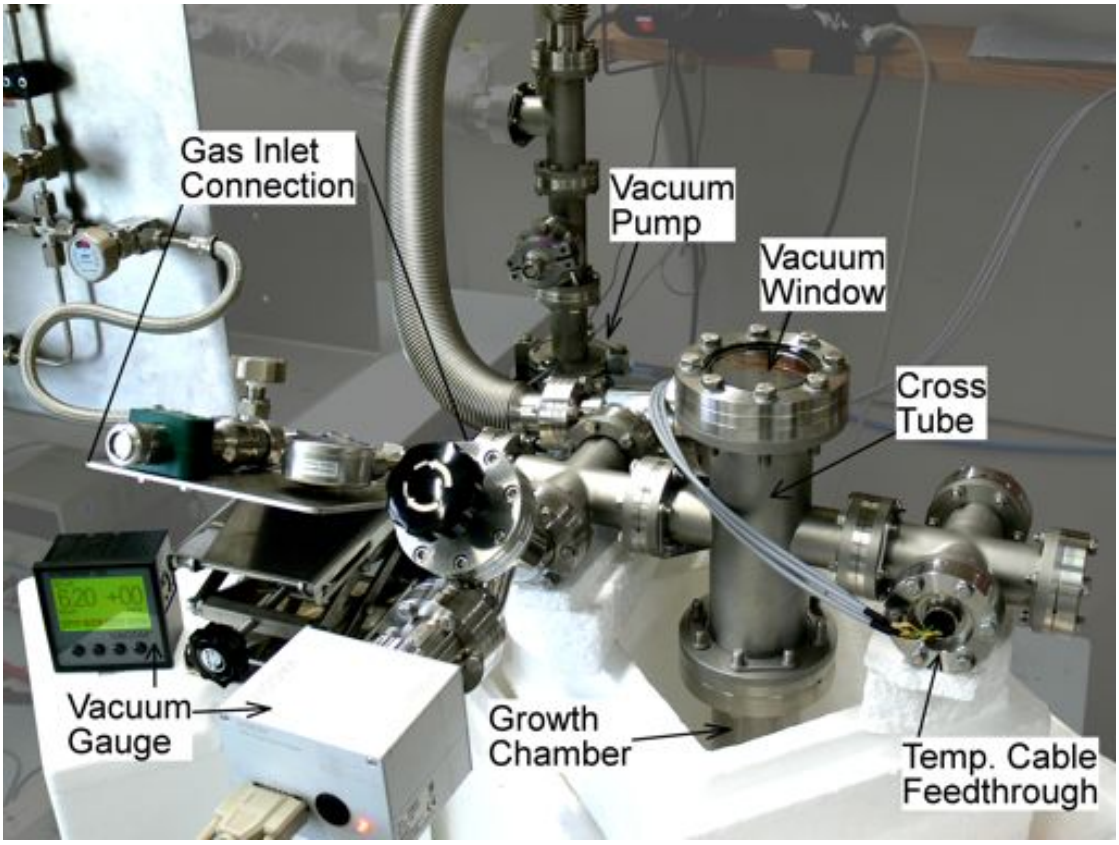

Figure 5.3.: This picture shows the vacuum components of the experimental setup. It consists of the growth chamber inside the Styrofoam container, the feedthrough flange for the RTD cables, the vacuum pump, the vacuum gauge and the connection to the gas inlet system. The components are joint together by the cross tube in the middle. Additionally, a vacuum window allows to take pictures of the growing procedure inside the chamber.

5.2.3. Growth Chamber, Cooling System and Thermal Isolation

In order to freeze krypton crystals, a cooling system is required which achieves temperatures below the freezing point of krypton (116.6 K at 1 mbar; See table A.1). The simplest way for such a system is to use liquid nitrogen (LN) with a temperature of about 77 K.

There are two basic challenges, the cooling system has to face. On the one hand, the LN-reservoir outside of the vacuum system has to be thermally linked to the inside of the growth chamber without affecting the tightness of the vacuum containment. This is achieved by using a cooling finger with one end dipped in LN whereas the other end is linked to a vacuum feedthrough. For this, a mechanical connection between the cooling finger and the vacuum vessels is required. This

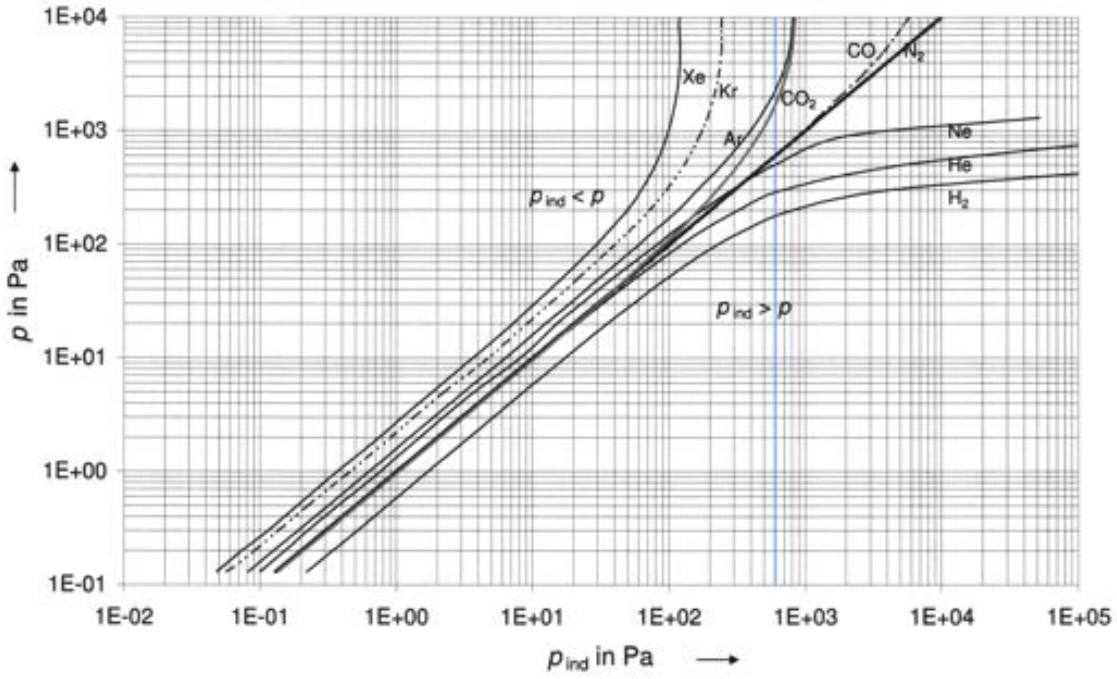

Figure 5.4.: The vacuum pressure measured by Pirani-gauges depends on the composition of the atmosphere inside of the vacuum vessel. This plot allows to convert the measured pressure ρ_{ind} into the actual pressure ρ in the vessel. The value displayed in figure 5.3 is highlighted in blue. This figure is taken from [39].

leads to the second challenge: The LN is not supposed to only cool down the entire vacuum system for several reasons. First, the vacuum system is quite large and a huge amount of LN would be required to cool down all of the vessels. Secondly, the tightness of CF-flanged is affected under cryogenic conditions. And thirdly, the krypton freezing is triggered by the coldest spot which should be the cooling finger. Otherwise, the crystal growth is initiated from all vessel walls causing undesirably inhomogeneities in the crystal structure. To avoid this a thermal isolation between the cooling finger feedthrough and the rest of the vacuum system is required. A vacuum tube can be a proper isolation if its thermal conductivity $\dot{Q}$ is quite small. The conductivity can be calculated by following formula:

$$\dot{Q} = A \cdot \lambda \cdot \frac{\Delta T}{l} \quad . \tag{5.1}$$

In this case, a heat-conducting bar with a cross-section area A and length l is considered. A temperature gradient ΔT is developed due to two separated heat reservoirs at both ends of the bar. $\dot{Q}$ depends on the conductivity parameter λ which in turn depends on the given material. To establish a good thermal isolation,

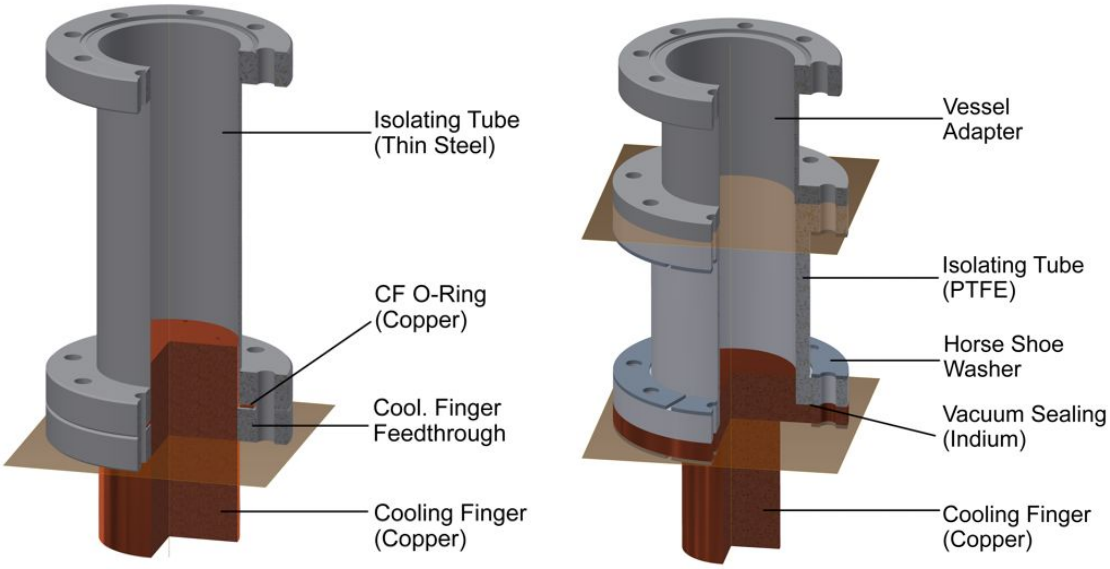

(a) Cooling finger feedthrough and thin steel tube as thermal isolation

(b) Copper flange and PTFE thermal isolation tube

Figure 5.5.: This figure shows two CAD drafts of different growth chamber designs. The structural connection of the copper cooling finger and the vacuum vessel above differs as well as the thermal isolation to the rest of the vacuum system. The left design was used for the experiments presented in this work.

either A has to be small or l has to be large or a material with a small thermal conductivity can be used.

In conclusion, the cooling finger and the thermal isolation part connected to the finger can be seen as the actual growth chamber for the RGS, the crystal growth is initiated solely from the cooling finger and the thermal isolation acts as boundary surface to the crystal. A possible experimental solution is presented in figure 5.5a. At the bottom, one can see the cooling finger. It is fabricated with copper due to its higher thermal conductivity (λ) so that the vacuum-side of the finger can be cooled down quickly to initiate the crystal growth at first. The copper finger is soldered firmly into a vacuum steel flange. A vacuum proof soldering seam was used. The thermal isolation consists of a common CF-vacuum steel tube with a wall thickness of only 500 µm instead of the common thickness of 1.8 mm. By doing so, the cross-section area A is reduced by a factor of about 3.7 and so is the thermal conductivity according to equation 5.1.

An alternative design of the growth chamber is shown in the CAD-draft in figure 5.5b. The thermal isolation is achieved by a PTFE tube due to its small λ which is about a factor of 150 to 200 smaller than in the case of steel. The inner

diameter of both PTFE tube and thin steel tube is 66 mm and the thickness of the PTFE tube is 7 mm in this draft. The softness of PTFE prevents a smaller wall thickness as in the first design. These values yield a ratio of about 14.7 for the cross-section areas of both tubes. Consequently, the thermal conductivity of the PTFE tube is still $10 - 14$ times smaller than that of the steel tube. As shown in figure 5.5b, the cooling finger is designed as a vacuum flange itself since no soldered seals are possible with PTFE. The vacuum tightening is done with indium – a very soft metal that can be pressed together between two flanges and fills up microscopic irregularities of the opposing flange surfaces.[6] Vacuum tests with this design were successful and a vacuum of $\mathcal{O}10^{-4}$ mbar could be achieved easily. However, the experiment failed entirely as soon as liquid nitrogen is filled in the Styrofoam container and reached the cooling finger. As a consequence, the indium sealing hardens causing a failure of the vacuum tightness and a massive increase of the vacuum pressure can be measured. This alternative setup design was abandoned due to these leakage problems.

The cooling system is realised based with regard to the experimental growth chamber design shown in figure 5.5a. The final setup is presented in figure 5.6. Beneath the big cross tube one can see the thermal isolation tube. It is connected to the cooling finger feedthrough on its bottom, which encloses the copper finger. The finger is stuck into a hole in the inner Styrofoam container. This entire part is located in a second bigger outer Styrofoam container filled with liquid nitrogen. The slit between the copper finger and the hole in the inner container is tightened with plasticine so that the liquid nitrogen can reach the end of the finger but not the vacuum components inside of the inner container. In this way, only the copper finger is cooled down but not the other vessels and the crystal growth solely happens on top of the cooling finger inside of the growth chamber.

5.2.4. Detector Module and Temperature Monitoring

In order to extract a secondary electron signal out of a RGS to be detected with a naked Timepix-ASIC, a drifting field is necessary to accelerate the electrons towards the signal readout plane. The field is realised by a potential between the ASIC (on ground) and a cathode grid where a high voltage up to a few kV can be applied. The area of the ASIC is rather small compared to the diameter of the growth chamber so that the cathode can be fabricated relatively large. As a consequence, the sensitive volume observed by the Timepix-ASIC is supposed

[6] The PTFE and copper flange are pressed together by common steel screws as in any other vacuum flange connections. Steel is a very hard material compared to PTFE so that horse shoe washers have to be used at the PTFE-side of each flange to prevent the steel screws from piercing into the soft PTFE flange.

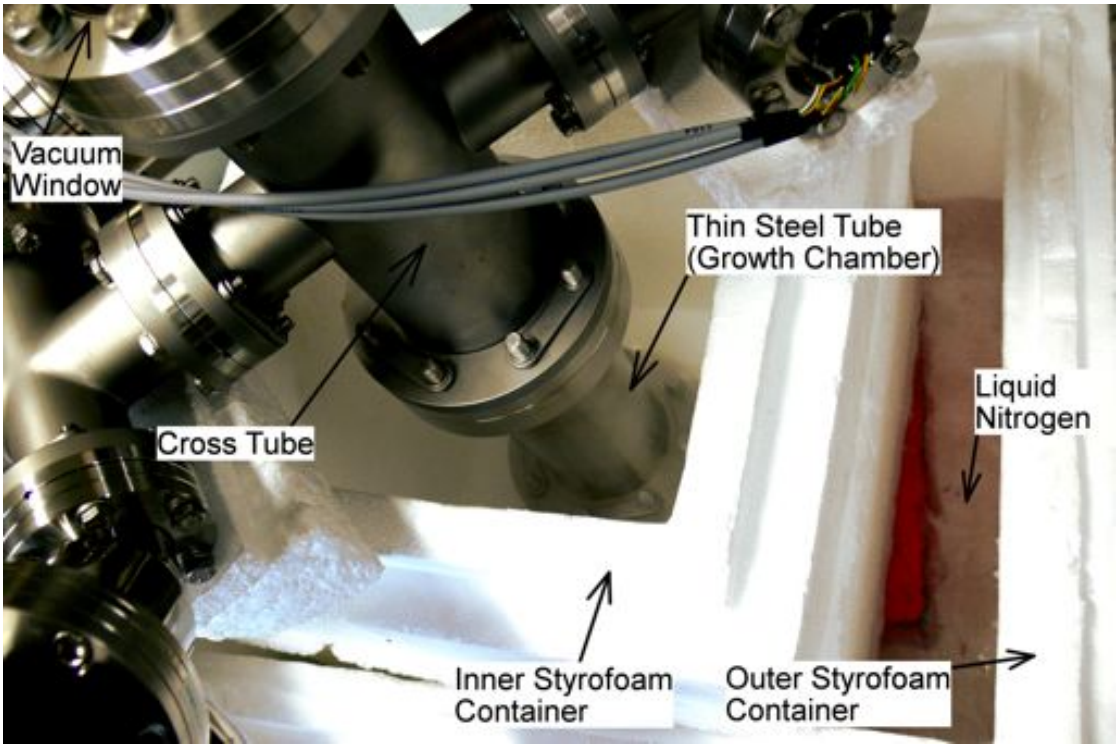

Figure 5.6.: This picture shows the thin steel thermal isolation tube, which is a part of the growth chamber. The copper finger beneath the thin steel tube is inserted in a hole in the inner Styrofoam container which in turn is located inside of the outer Styrofoam reservoir. By adding liquid nitrogen to the outer reservoir the copper finger can be cooled down.

to present a sufficiently homogeneous electric field to perform a proof-of-principle experiment for a signal readout from solid krypton with a naked Timepix ASIC.

Figure 5.7 shows a CAD draft of the detector module fixed on top of the cooling finger. It consists of a PTFE frame (in white) and the cathode which is screwed immediately above the bottom of the PTFE frame. The cathode is designed as a grid so that the crystal can grow right through the grid meshes. The major detector volume is eventually established above the cathode grid between the PTFE walls. The PTFE frame has four notches at its top where the Timepix detector can be fixated. The crystal should be grown up to the Timepix ASIC to act as sensor material. Two additional smaller notches at the right side of the PTFE frame allow to attach RTDs in order to measure the vertical temperature gradient in the growth chamber and and in this way the crystal growth process should be monitored. One additional detector is attached directly to the copper surface in order to measure the temperature of the cooling finger. The RTDs used in this

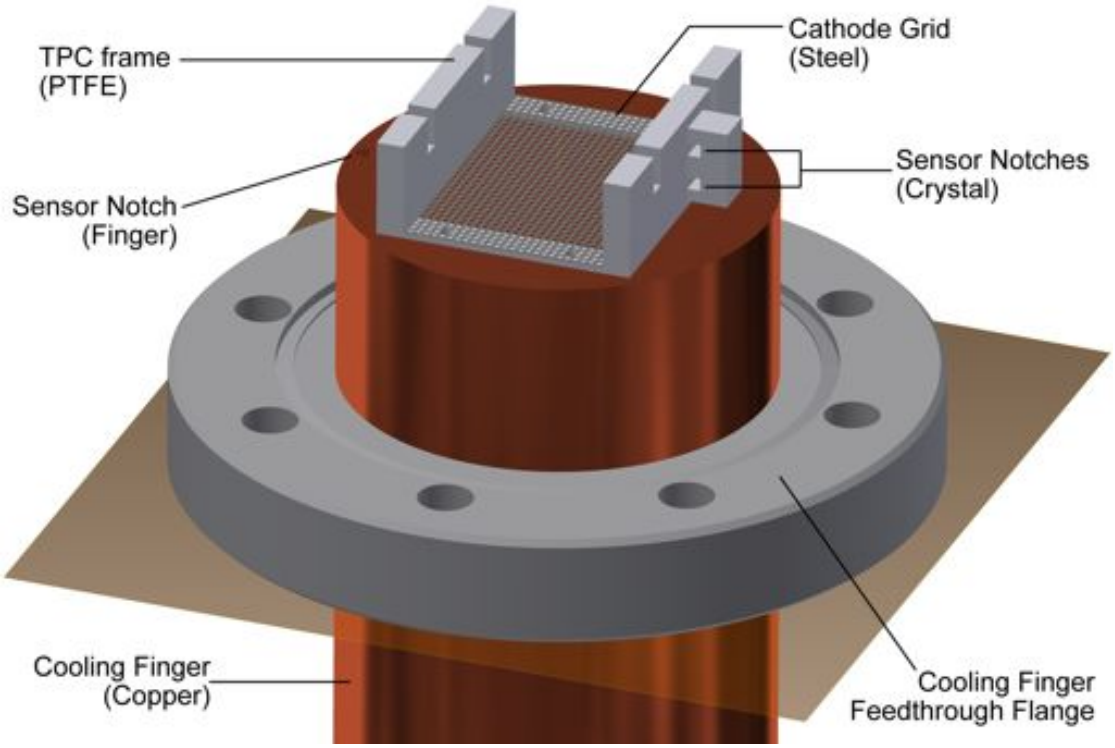

Figure 5.7.: This figure shows a CAD draft of the TPC module on top of the cooling finger. The PTFE frame holds the cathode grid at the bottom and the Timepix detector with the help of the top notches in place. The crystal grows up from the copper surface through the cathode meshes and further upwards to the Timepix-ASIC. Two RTDs with vertical distance allow to measure the position of the crystal surface throughout the growing process.

experiment are PT-100 sensors from Honeywell. They are connected to the vacuum feedthrough shown in figure 5.3.

5.2.5. Gas Inlet System

The gas inlet system regulates the krypton inflow to the growth chamber. This is necessary for several reasons. At first, common gas cylinders are high-pressurised (80 bar in this experiment). However, the vacuum system is designed for negative pressures and the gas inlet system needs to regulate the pressure down to 1 bar. The second reason is that if the crystal should be grown by vapour deposition, the mass flow into the chamber depends on the gas inflow. The homogeneity of the crystal and hence the lattice quality might be improved by reducing the growth velocity. The third reason is that a gas inlet system would allow to regain the used gas as soon as the crystal is sublimated. This will be very important in the case of

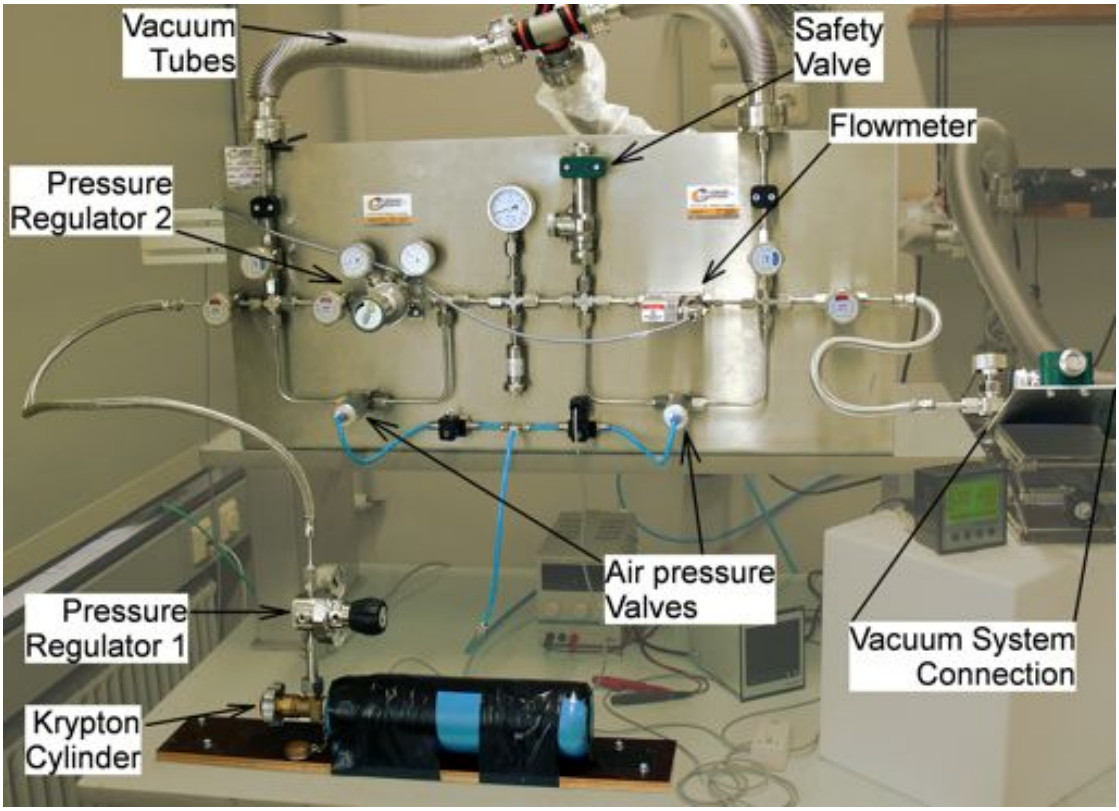

Figure 5.8.: This picture shows the gas inlet system consisting of the krypton cylinder, two separate pressure regulators to decrease the cylinder gas pressure, a safety valve to protect the vacuum system from overpressure and a flowmeter to regulate the gas inflow to the growth chamber. The top tubes are connected to the vacuum pump to evacuate the inlet system before krypton enters. The system is attached to the vacuum system via a connector board on the right. Bypasses with air pressure valves allow to regain the gas from the growth chamber back to a collection cylinder.

xenon since this rare gas is far more expensive than krypton. In this experiment, no gas re-flow to the bottle was performed yet.

A photography of the gas inlet system is presented in figure 5.8. The krypton cylinder bottle on the bottom is attached to the first pressure regulation instrument. It decreases the krypton pressure from the high-pressure side, which is the cylinder at 80 bar, to the low-pressure side, which is set to be about 10 bar in the subsequent tube. The second regulation instrument at the left side of the steel plate decreases the pressure from 10 bar, which is now the high-pressure side, to about 1 bar. This final pressure value is well suitable for vacuum vessels. Right to the second pressure

regulator, the flowmeter can be seen. This instrument allows to regulate the gas inflow to the vacuum system and therefore to limit the crystal growth velocity.

At this point, some smaller components have to be mentioned, as well. Firstly, a safety valve is attached between the second pressure regulator and the flowmeter releasing at an overpressure of 5 bar to protect the flowmeter and hence the vacuum system. Secondly, both pressure regulator and flowmeter are equipped with bypasses below controlled by air pressure valves. In this manner, both components can be short-circuited to enable a gas regain from the crystal in the growth chamber backwards to a collection cylinder. Thirdly, vacuum tubes are installed at the top of the gas inlet system to evacuate this system in order to avoid major contaminations of the krypton gas while passing it. At last, the gas inlet system is attached to the vacuum system via a connection board, which also can be seen in figures 5.8 and 5.3. This connection board is also equipped with an additional safety valve to protect the vacuum system from overpressure.

5.3. First Crystal Growth Test

The first step to test the setup was a to grow a RGS inside the growth chamber. This is achieved by filling the vacuum vessels with krypton and cooling down the copper finger with liquid nitrogen. The RGS was grown out of the liquid phase of krypton by steadily decreasing the temperature inside of the growth chamber. This section explains the single steps of the experiment chronologically. The setup is used as shown in figure 5.2.

Pumping

Prior to the actual experiment, the vacuum system as well as the gas inlet system were evacuated to avoid contaminations of the krypton. The final vacuum pressure achieved in the growth chamber was 2×10^{-5} mbar. The purification level of the krypton gas used in this experiment was 10 ppm according to the manufacturer and refers to one impurity atom for every 10^5 Kr-atoms.[7] This value corresponds to a vacuum pressure better than 10 mbar, if the contamination of krypton by the remaining atmosphere is supposed to be lower than the intrinsic impurity of the krypton and the growth chamber pressure is 1 bar after the gas inlet. Consequently, the vacuum is sufficiently good for this experiment and the predominant krypton contamination is the intrinsic impurity.

The pipes of the gas inlet system are smaller in diameter than the vacuum system tubes so that they are able to resist overpressure. As a consequence, the gas flux and such the pumping power is reduced significantly in the gas inlet system.

[7]Specification sheet: `http://produkte.linde-gase.de/db_neu/krypton_5.0.pdf`

The vacuum pressure in this system is not measured in this experiment but was measured previously to be about one order of magnitude higher than that of the vacuum system which still is a suitable value compared to the krypton pureness.

Before the krypton gas enters the vacuum system, the vacuum pump needs to be decoupled from the growth chamber to protect the turbo-molecular pump. This was done at a pressure of $2 \cdot 10^{-5}$ mbar. Afterwards, the chamber is filled with krypton at about 1 mbar. The picture shown in figure 5.3 represents this stadium of the experiment.

Gas Inlet

After the decoupling of the pump, the krypton was allowed to enter the gas inlet system and the growth chamber. The cylinder overpressure was reduced in two steps as shown in figure 5.8. The flowmeter was bypassed since only the pure crystal growth process was examined and the second pressure regulator is the last step on the krypton's way to the growth chamber. The pressure in the single pressure domains is stabilised very quickly based on the settings of the regulator valves. The krypton pressure in the growth chamber was maintained at 1 atm.

This stabilised pre-freezing situation is shown in figure 5.3. As already mentioned, the vacuum gauge functionality is gas dependent. This is why only $6.2 \cdot 10^{+00}$ mbar is displayed albeit the second pressure regulator of the gas inlet system is set to establish about 1 bar at its low-pressure side.

Cooling and Freezing

Having the growth chamber evacuated and the krypton inlet regulated, the cooling process was started. As illustrated in figure 5.6, this was done by filling the outer Styrofoam container with liquid nitrogen which gets in contact with the bottom of the copper finger. The cooling process was observed by three RTDs in the growth chamber: One on top of the copper finger and two at different heights on one side of the detector-module to gain information about the level of the krypton phase transition zones.

The corresponding temperature plot in figure 5.9 shows the temperature of all three RTDs throughout the cooling process.[8] The red curve corresponds to the RTD on top of the copper finger, the green curve to the lower RTD of the detector module and the blue curve to the upper RTD. The melting and boiling points of krypton are indicated by horizontal dotted lines at 116.6 K and 120.9 K, respectively (see table A.1). The temperature plot can be divided into several domains, which are explained in the following.

1: All RTDs are at room temperature, here. The cooling process was started by adding liquid nitrogen to the outer Styrofoam reservoir causing a dramatic

[8] In this case, the temperature detector readout frequency was 2 Hz.

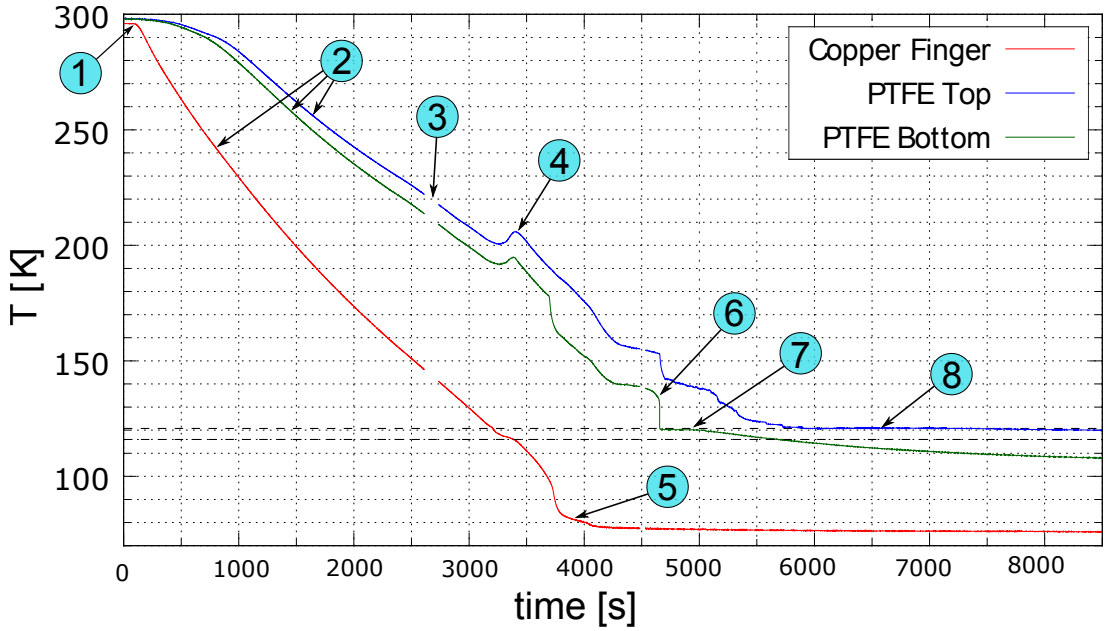

Figure 5.9.: This plot shows the temperature (in Kelvin) of the three RTDs located at different heights at the side of the detector-module and on top of the copper finger itself over the elapsed time (in seconds) during the entire cooling and freezing process. The melting and boiling temperatures of krypton are indicated by two horizontal dotted lines.

temperature drop of the copper finger since it is in direct contact to the nitrogen. Due to the good thermal isolation property of PTFE, the module-temperatures dropped far more smoothly.

2: The continuous cooling process caused a stronger temperature decrease in the case of the copper finger compared to the detector-module. All curves are not straight lines since the heat exchange and the thermal conductivity depend on the decreasing temperature difference of both involved thermal reservoirs.

3: The measurement was interrupted here due to read out problems. The time gap to the second measurement was estimated based on an extrapolation of continuous temperature curves to about 250 s.

4: After about 50 min, the temperature of the copper finger dropped beyond the boiling point of krypton and shortly afterwards beyond the melting point. As a consequence, the condensation and freezing of krypton was triggered at the surface of the cooling finger. At the same time, evaporation and

melting energy was released. This led to a small plateau of the copper finger temperature due to this additional energy input and to an increase in temperature in the detector-module, which still was at the gaseous level.

5: The cooling finger reached the temperature of liquid nitrogen. In the meantime, heat was still drawn constantly out of the growth chamber causing the crystal to grow slowly upwards while cooling down. The density of solid krypton is about 750 times higher than the density of the gaseous state (see table A.1). As a consequence, the krypton volume in the growth chamber decreased massively throughout the freezing process. This had to be compensated by an inflow from the gas inlet system so that the pressure of the krypton cylinder dropped steadily.

6: At this point, the gaseous-liquid phase transition level arrived at the lower RTD at the detector-module and the green temperature plot shows a sudden drop. This drop is assumed to be caused by evaporation energy released into the growth chamber throughout the crystal growth. Consequently, the gaseous krypton layer directly above the gaseous-liquid phase transition zone was heated up slightly so that the temperature dropped suddenly as soon as the actual transition level reached the RTD. This might also caused the thermal plateau directly before the sudden drop. Furthermore, the thermal conductivity of krypton in the liquid phase is much higher compared to its gaseous phase so that any heat load from the RTDs was compensated very quickly.

7: After the sudden drop, the green curve presents a small plateau as well which is caused by released evaporation energy at the level of the lower module-RTD. However, such a plateau cannot be seen at temperatures around the freezing point despite the melting energy is 5.5 times higher than the evaporation energy. It is assumed that the whole melting energy released at the liquid-solid transition level is carried away too quickly due to the much better thermal conductivity of the solid phase. In this case, no temperature plateau could be developed. All values for the thermal conductivity of krypton at different physical states can be found in table A.1.

8: At last, the gaseous-liquid transition level reached the upper module-RTD and a plateau is developed as in the case of the lower RTD. However, the large plateau length compared to the one of the green curve and the missing temperature drop at its start cannot be explained here.

The temperature curves allowed only a limited monitoring of the crystal growth. A different way to follow this process is the direct observation via the vacuum glass.

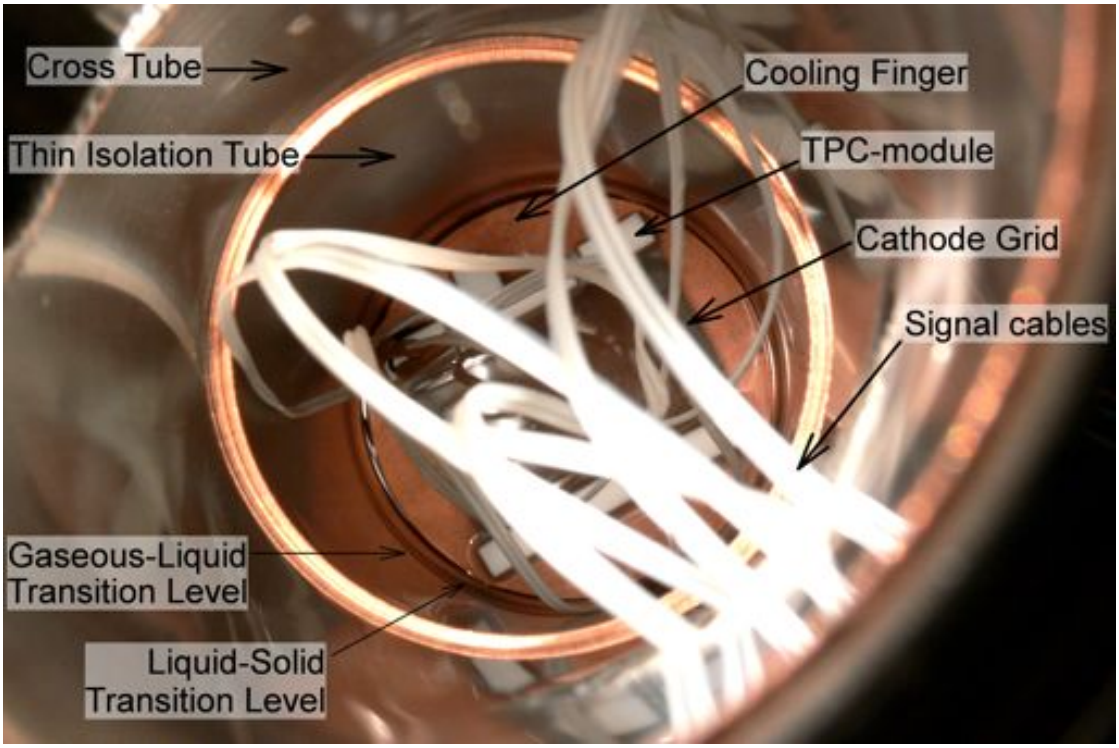

Figure 5.10.: This picture shows the inside of the growth chamber with a liquid and solid krypton phase which can be recognised by the transition level lines at the side of the thermal isolation tube and the reflections of the krypton surface.

Figure 5.10 shows a picture of the inside of the growth chamber during the crystal growth. The inner side of the cross tube and the thin isolation tube can be seen as well as the surface of the copper finger, the white detector-module and the cathode grid. The RTD cables are pulled through one of the side holes in the cross tube.

The light reflection above the cathode grid showed that there is a layer of liquefied or frozen krypton. Additionally, these reflections shiver if the vacuum vessels are slightly shaken. Dark circular lines at the inner tube walls slightly above the copper finger surface indicate the height of the krypton phase transition levels. There are two dark circles with just a small vertical distance between each other which are assumed to correspond to the gaseous-liquid transition level at the top and the liquid-solid level at the bottom. The height of the crystal is approximately 2 cm.

This value is consistent with the calculated height based on the pressure difference in the krypton cylinder. The cylinder was filled with 200 l krypton at 80 bar. At the end of the crystal growth, the remaining pressure was 60 bar and 50 l krypton were used to freeze the RGS. Considering the krypton densities presented in table A.1

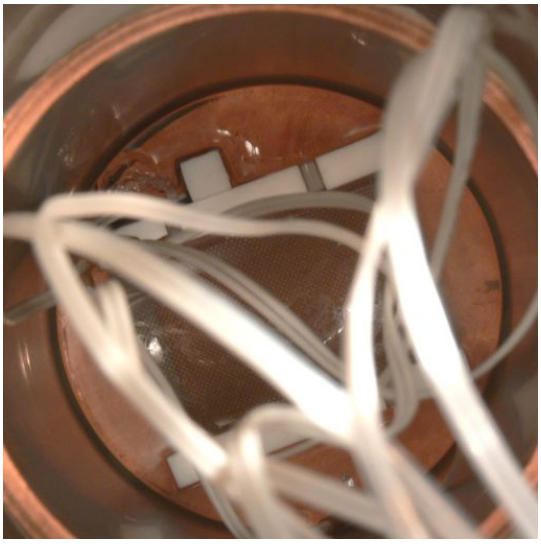

(a) Equalization-point after disappearance of the liquid phase

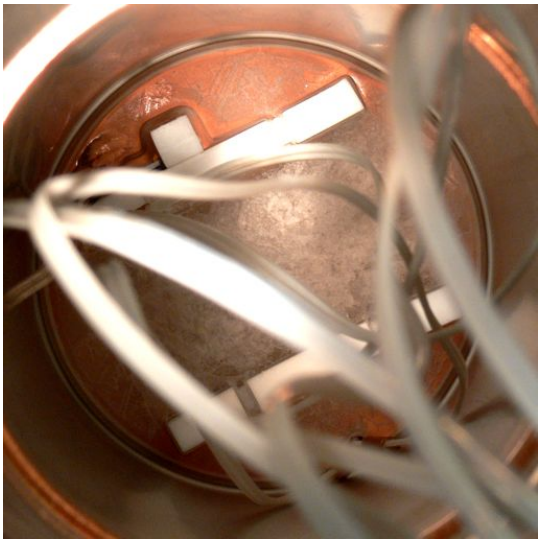

(b) Broken crystal surface after quick freezing of the isolation tube

Figure 5.11.: These pictures show the growth chamber after the decoupling of the gas inlet system with ongoing cooling process. The liquid phase is vanished and the krypton gas pressure corresponds to the vapour pressure of solid krypton. **(a)** shows a pure solid krypton phase far beyond its melting point. **(b)** shows the broken crystal surface after additional cooling of the growth chamber walls.

as well as the inner diameter of the growth chamber $d_{\mathrm{GC}} = 66\,\mathrm{mm}$, this volume corresponds to a crystal height of about 1.9 cm – consistent to the direct observation.

Decoupling of the Krypton Cylinder

The krypton cylinder was closed about 4.5 hr after the start of the experiment and 3.5 hr after the RGS started to grow in order to cut off the continuous krypton inflow. By doing so, the krypton gas remained in the vacuum system continued to condense on top of the cold liquid krypton surface and the pressure in the growth chamber dropped below 1 bar. This process stopped as soon as the condensation rate and the low-temperature evaporation rate of the RGS were equalised. After this equalization-point had been reached, the gas pressure in the vacuum vessels stagnated. The liquid krypton phase froze out entirely since no more krypton condensation maintained the liquid phase. In the meantime, the temperature of the RGS continued to decrease due to the cooled copper finger.

A picture of this experimental state is presented in figure 5.11a. The krypton is entirely frozen so that no liquid phase can be seen. There are no shiny reflections

at the sides of the isolation tube and no phase transition circles on the walls. Additionally, no shivering of the reflections could be seen if the vacuum system was shaken slightly. A second case is shown in figure 5.11b. Here, liquid nitrogen had been filled in the inner Styrofoam container as well so that the isolation tube and such the crystal inside got cooled down very quickly. Due to the high tensions in the crystal, its surface broke up and consequently, the crystal is opaque and can be recognised easily.[9]

Throughout the freeze-out of the liquid phase, the krypton pressure measured by the Pirani-gauge dropped significantly. This can be explained by the vapour pressure correlation. The evaporation rate of any crystal is strongly temperature-dependent and such is the equalization-point of evaporation and condensation rate mentioned above. This dependency is described by the so-called vapour pressure curve presented in figure 5.12. It shows the pressure of a specific gas above its condensed phase over temperature. The curve separates the different phase domains depending on the specific pressure and temperature. The lower right domain in the plot indicates the gaseous phase and the upper left domain the solid phase.[10]

As a consequence, if the pressure p and the temperature T of a specific system are measured, the actual phase state can be determined by the location of the given (p, T)-values in the plot. Furthermore, if a dual-phase system is examined as in this case, temperature and pressure are correlated if the mentioned equalization-point is reached. This correlation corresponds to the phase transition line in figure 5.12. Vapour pressure curves generally are determined by empirical data. However, it is possible to fit the following equations to the measured (p, T)-data points as done in [41]:

$$\text{solid krypton}: \quad \log_{10}(p(\text{mm})) = 7.70741 - 575.267 \cdot T^{-1} \tag{5.2}$$

$$\text{liquid krypton}: \quad \log_{10}(p(\text{mm})) = 6.96880 - 489.70 \cdot T^{-1} \tag{5.3}$$

Considering again the krypton crystal, equation 5.2 correlates the temperature T of the krypton RGS with the vapour pressure p of the gaseous krypton phase above the solid. In reality, there is a temperature gradient in the krypton crystal. At its bottom, the temperature is about 77 K, which is the final temperature of the copper finger. At its top, the temperature is somewhat higher and this is the actual temperature relevant for the determination of the vapour pressure.

At a certain point of the experiment, the values given by RTDs start to be unreliable with strong sudden jumps and temperatures far beyond the boiling point although they were still stuck in the crystal. Hence, the actual temperature of the

[9] It is not wrong to call the white surface krypton-snow.

[10] The liquid domain is missing in the plot. In fact, the triple point of krypton is at about 116 K and 730 mbar. This point marks the begin of the solid-liquid transition line that leads upwards turning the plotted line into the liquid-gaseous transition line at a temperature above 116 K.

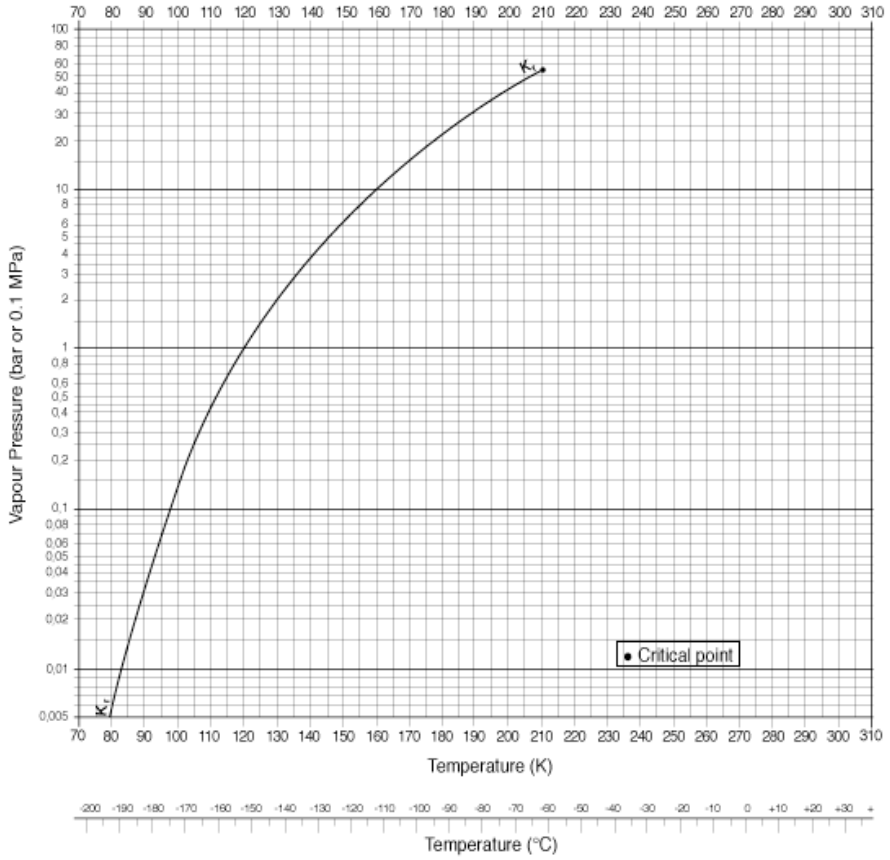

Figure 5.12.: This plot shows the vapour pressure curve of krypton. Below the curve, temperature and pressure cause krypton to be gaseous. It also describes the possible (p, T)-values of any equalization-point so that the curve correlates the pressure p of gaseous krypton above a crystal at temperature T. This plot is taken from [40].

crystal (surface) was obtained by the vapour pressure curve instead of the RTDs based on the pressure given by the Pirani-gauge. The results for the two cases shown in figure 5.11 are presented in table 5.1.

At the left, the pressure values measured by the Pirani-gauge and the actual krypton pressure obtained with the Pirani-conversion plot in figure 5.4 are shown. The upper pressure was measured in the case of the smooth crystal surface after the liquid phase was frozen and the lower pressure was obtained after the shock freezing of the RGS (see figure 5.11). The temperature correlated to the krypton pressure was obtained in three different ways. At first by using the vapour pressure

Pressure [mbar]		Temperature [K]		
Pirani	Kr-gas	Vap. pres.	Table in [41]	Equation 5.2
2.2	40	92	92.31	92.35
6.4×10^{-1}	1.8	< 80	< 83.28	75.92

Table 5.1.: This table presents the pressure values measured by the Pirani-gauge, the converted real pressure of the krypton gas and the corresponding temperature of the solid-gaseous transition being determined in three different ways.

curve shown in figure 5.12, secondly by an interpolation of the measurement values presented in [41][11] and thirdly by a direct calculation using equation 5.2.[12]

The last reliable actual temperature measurement can be seen at the right end in figure 5.9 for the upper RTD with a value of about 107 K. The krypton cylinder was closed after this measurement and the liquid phase has been frozen completely so that the temperature should be somewhere between 107 K and 77 K. Considering the temperature gradient after the RTDs failed, it can be assumed that the temperature has dropped below 100 K so that the temperature values in the case of the smooth crystal surface (upper row in table 5.1) are quite realistic.

In the case of the shock freeze-out (lower row), the temperature should be about 77 K. The vapour pressure curve and the data table stopped at higher values and exact values could only obtained by equation 5.2. The value given in the table is somewhat smaller than the temperature of liquid nitrogen. The reason for that is mainly the inaccuracy of the Pirani-gauge and possible reading errors considering the Pirani-conversion plot so that 75.92 K is also quite reliable.

Crystal Boiling

At last, the liquid nitrogen in the Styrofoam was removed to slowly rewarm the copper finger and the vacuum vessels to room temperature. As soon as the temperature in the growth chamber exceeds the melting point of krypton the crystal begins to boil or to sublimate. The process is shown in figure 5.13.

Before the boiling point is reached, it is very important to open the vacuum system due to the enormous increase of the krypton density associated with the solid-gaseous transition. As mentioned above, the density ratio is about 750 so that the vacuum system is likely to burst due to the massive internal pressure. In

[11] See table 2 on page 1465.

[12] Note that this equation is a fit of the same data in table 2 in [41] which stops at 83.28 K so that any calculation of temperatures smaller than this value actually represents an extrapolation.

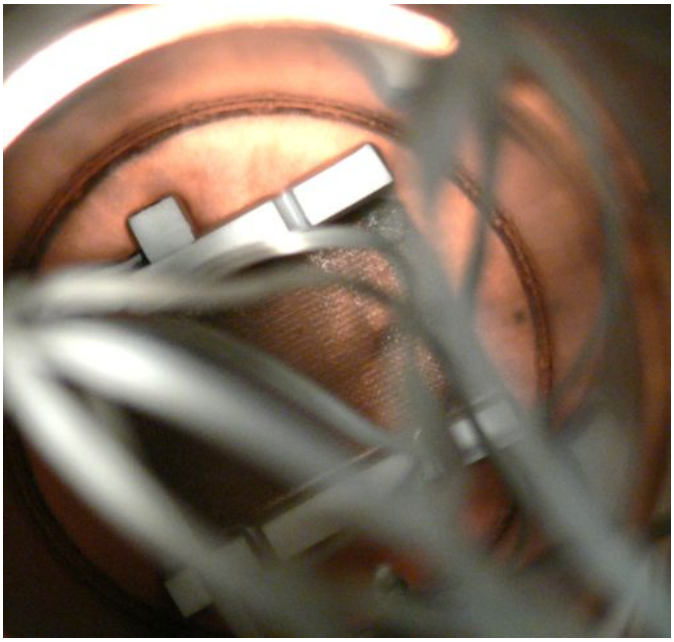

Figure 5.13: This picture shows a boiling krypton crystal after the liquid nitrogen cooling is stopped and the temperature inside of the growth chamber exceeds the boiling point. For example, the rolling boil is visible at the right end of the cathode grid.

future experiments, the gas can be recollected by using the gas inlet bypasses and a very cold collection bottle at the location of the krypton cylinder.

6. Conclusions and Outlook

As presented in chapter 5, it is possible to grow krypton crystals with a thickness at the cm-scale in a vacuum containment and to evacuate the growth chamber down to a certain temperature-dependent pressure. Several challenges as the regulation of the gas inflow and the thermal isolation of the growth chamber from the rest of the vacuum system have been overcome.

The next steps of this early experimental stage is to introduce the naked Timepix-ASIC to the detector-module and to grow a krypton crystal up to the ASIC electrodes. This is to examine, if solid krypton can be used to replace the Timepix sensor layer and to attack actual tracking experiments of fast particles interacting with the RGS sensor material. At the same time, it is important to construct a better way to monitor the crystal growing process i.e. the observation of the location of the phase transition levels. This would be the first particle tracking experiment using rare gas solids as sensor material.

Afterwards, the whole experiment has to be repeated with solid xenon instead of krypton to prove that xenon can be used as a sensor material as well. Additionally, the usage of the flowmeter instrument mentioned along with the gas inlet system in section 5.2 could be used to examine different lattice qualities under varying crystal growth rates. For that, however, a new setup design is necessary to allow X-rays to cross the growth chamber without getting absorbed by its walls. By doing so, basic crystallographic examinations can be performed to gain knowledge about the best growing parameters for the growth of high quality crystals serving as a sensitive volume for a RGS based particle detector.

In future, tracking experiments of $\beta\beta x\nu$-decays would require the signal mass to be scaled up significantly which means to produce larger crystals. In order to achieve that, a massive improvement of the rare gas pureness is necessary to reduce radioactive contaminations of the detector and to improve the secondary electron lifetime. Chapter 4 shows that an electron optical system provides the possibility to observe a larger crystal surface with only one or few pixel detectors. As presented there, a selector system allows to pick out a specific part of the crystal surface and to extract a secondary electron signal from the covered crystal volume beneath. Afterwards, an electron lensing system can be used to magnify the track in order to achieve a better spatial resolution. This system showed a good imaging efficiency in simulation but of course has to be examined under actual experimental conditions.

With all these things accomplished and realised in experimental setups, the last challenge is the careful separation of background from the tracks detected in the RGS sensor material. The main background signals are the single beta decay from radio impurities and the intrinsic double beta decay of the decay material. This intrinsic background only can be separated by a superb energy resolution to spot the small $\beta\beta0\nu$-tip in the broad $\beta\beta$-spectrum at the Q-value. One step towards that goal might be to cover a larger surface with pixelated detectors to improve the energy statistics of the evaluated events. Besides that, a larger sensor layer would further improve the spatial resolution. A possibility to scale up the sensor layer is to use stacks of several Timepix detectors.

There are several ideas, to reduce the single beta background. At the one hand, the radio pureness of all detector components has to be increased to reduce the general beta-rate in the growth chamber. On the other hand, it is useful to optimise the data processing to achieve a better efficiency of the separation of single beta and double beta events. Thirdly, new designs of the Timepix detector are able to measure both energy and time of arrival of each pixel simultaneously. This would be a big step forward in the experimental concept e.g. to achieve 3D reconstruction techniques with energy resolution. Last but not least, the search for ^{136}Ba nuclei – the product nucleus of $\beta\beta$-decays of ^{136}Xe – would allow to achieve an excellent separation efficiency of single beta decays since the presence of such barium atoms can only be explained by some kind of $\beta\beta$-activity. However, such techniques are very sophisticated and have to be examined very precisely before being applied in $\beta\beta0\nu$-experiments.

In conclusion, only the first small steps have been accomplished at this experiment. Future upgrades will push it further until, hopefully, the next look at the the world beyond the Standard Model can be taken.

A. Addendum

A.1. Thermal Property Tables of Krypton and Xenon

Table A.1 presents the thermodynamic properties of krypton – more exactly the boiling and melting point T_b and T_m, the temperature and pressure of the triple point (TP), the density ρ and the thermal conductivity λ of all three phases as well as the heat of fusion, vaporization and sublimation. In the case of the density and the thermal conductivity, it is important to consider the temperature-dependence of the corresponding values. The sources of the measured values are referenced in the right column.

Table A.2 presents the same thermodynamic properties as above for xenon. Most of the differences between the values for xenon and krypton are essentially due to the differences of the molecular masses and the atomic radii and hence the intensity of the van der Waals interaction, the atomic weight or the lattice constants.

Quantity	State	Value	Source
Temp. Points	T_b	120.9 K	[52], tab. 3
		119.74 K	at 1 atm [20], tab. 2.1
	T_m	116.6 K	[52], tab. 3
Triple Point	T_T	115.8 K	[45], tab. I
	p_T	729.8 mbar	[45], tab. I
Density ρ	gaseous	$3.749\,\mathrm{kg\,m^{-3}}$	at 1 bar, 0° [49]
		$3.696\,\mathrm{kg\,m^{-3}}$	at 273 K, 1 atm [20], tab 2.1
	liquid	$2451\,\mathrm{kg\,m^{-3}}$	at TP [49], tab 3
		$2413\,\mathrm{kg\,m^{-3}}$	at T_b [20], tab. 2.1
	solid	$2826\,\mathrm{kg\,m^{-3}}$	at TP [49], tab 3
		$\gtrsim 2800\,\mathrm{kg\,m^{-3}}$	[20], fig. 2.1
		$2804\,\mathrm{kg\,m^{-3}}$	at 115 K [50], tab. X
		$2942\,\mathrm{kg\,m^{-3}}$	at 77 K (interpol.) [50], tab. X
Thermal Conductivity λ	gaseous	$8.74\,\mathrm{mW\,K^{-1}m^{-1}}$	at 101.32 kPa, 0°C [49], tab 3
		$8.78\,\mathrm{mW\,K^{-1}m^{-1}}$	at 273 K, 1 bar [20], tab. 2.1
	liquid	$88.3\,\mathrm{mW\,K^{-1}m^{-1}}$	at T_b [49], tab 3
		$90\,\mathrm{mW\,K^{-1}m^{-1}}$	at T_b [20], tab. 2.1
	solid	$235\,\mathrm{mW\,K^{-1}m^{-1}}$	at 115 K (cal.) [54]
		$351\,\mathrm{mW\,K^{-1}m^{-1}}$	at 77 K (cal.) [54]
		$338\,\mathrm{mW\,K^{-1}m^{-1}}$	at 77 K (cal.) [51]
Heat of phase transition	fusion	$1.64\,\mathrm{kJ\,mol^{-1}}$	at ~ 115.9 K [41]
		$1.64\,\mathrm{kJ\,mol^{-1}}$	at T_T [20], tab. 2.1
	vapor.	$9.05\,\mathrm{kJ\,mol^{-1}}$	at T_b [41]
		$9.03\,\mathrm{kJ\,mol^{-1}}$	at T_b [20], tab. 2.1
	sublim.	$10.79\,\mathrm{kJ\,mol^{-1}}$	at T_T [45], tab. IX

Table A.1.: Overview of some thermodynamic properties of krypton considering its usage as detector medium under cryogenic conditions. The values given in the table are obtained from the references presented in the right column, calculated from specific given formulas there or interpolated from data tables.

Quantity	State	Value	Source
Temp. Points	T_b	166 K	[52], tab. 3
		165.03 K	norm. [52], tab. 1
	T_m	161.3 K	[52], tab. 3
Triple Point	T_T	161.4 K	[45], tab. I
	p_T	816.1 mbar	[45], tab. I
Density ρ	gaseous	$5.897\,\mathrm{kg\,m^{-3}}$	at 1 bar, 0° [49]
		$5.897\,\mathrm{kg\,m^{-3}}$	at 273 K, 1 atm [20], tab 2.1
	liquid	$3084\,\mathrm{kg\,m^{-3}}$	at TP [49], tab 3
		$3100\,\mathrm{kg\,m^{-3}}$	at T_b [20], tab. 2.1
	solid	$3540\,\mathrm{kg\,m^{-3}}$	at TP [49], tab 3
		$\gtrsim 3600\,\mathrm{kg\,m^{-3}}$	[20], fig. 2.1
		$3407\,\mathrm{kg\,m^{-3}}$	at 160 K [50], tab. XI
		$3649\,\mathrm{kg\,m^{-3}}$	at 77 K (interpol.) [50], tab. X
Thermal Conductivity λ	gaseous	$5.06\,\mathrm{mW\,K^{-1}m^{-1}}$	at 101.32 kPa, 0°C [49], tab 3
		$5.192\,\mathrm{mW\,K^{-1}m^{-1}}$	at 273 K, 1 bar [20], tab. 2.1
	liquid	$73.2\,\mathrm{mW\,K^{-1}m^{-1}}$	[49], tab 3
		$71\,\mathrm{mW\,K^{-1}m^{-1}}$	at T_b [20], tab. 2.1
	solid	$461\,\mathrm{mW\,K^{-1}m^{-1}}$	at 77 K (cal.) [51]
Heat of phase transition	fusion	$2.315\,\mathrm{kJ\,mol^{-1}}$	at ~ 115.9 K [53]
		$2.30\,\mathrm{kJ\,mol^{-1}}$	at T_T [20], tab. 2.1
	vapor.	$12.52\,\mathrm{kJ\,mol^{-1}}$	at 165.066 K [44]
		$12.64\,\mathrm{kJ\,mol^{-1}}$	at T_b [20], tab. 2.1
	sublim.	$15.04\,\mathrm{kJ\,mol^{-1}}$	at T_T [45], tab. IX

Table A.2.: Overview of some thermodynamic properties of xenon considering its usage as detector medium under cryogenic conditions. The values given in the table are obtained from the references presented in the right column, calculated from specific given formulas there or interpolated from data tables.

A.2. Inlet Shape Plots of Different Geometries of the Electron Optical Components

A.2.1. Different Selector Plate Length L

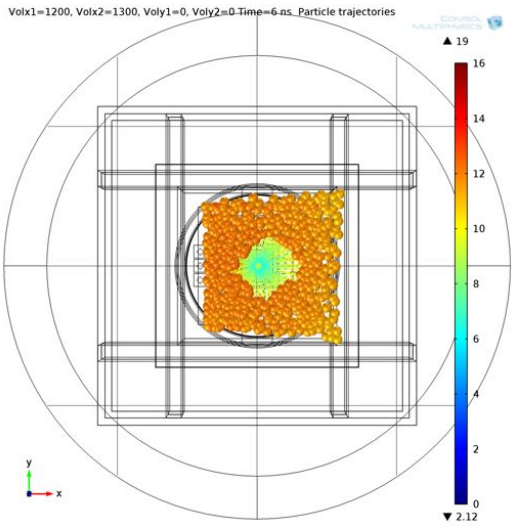

(a) $L = 40\,\mathrm{mm}$

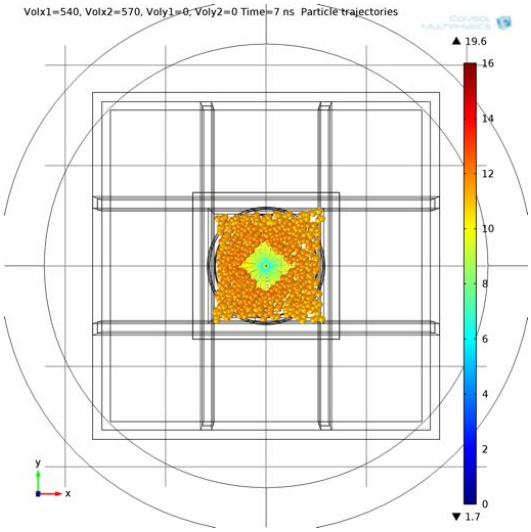

(c) $L = 60\,\mathrm{mm}$

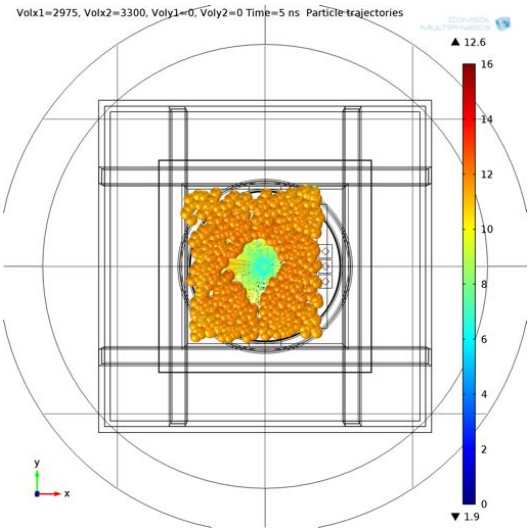

(b) $L = 25\,\mathrm{mm}$

Figure A.1.: These xy-trajectory plots present several images of the magnified inlet shape at the level of the detector if the plate length of the selector potential plates is varied. The shorter the plates the higher are the corresponding deflection potentials causing an increased distortion of the rhombus. Other aberrations are due to the unadjusted selector geometry in contrast.

A.2.2. Different Aperture Diameters d

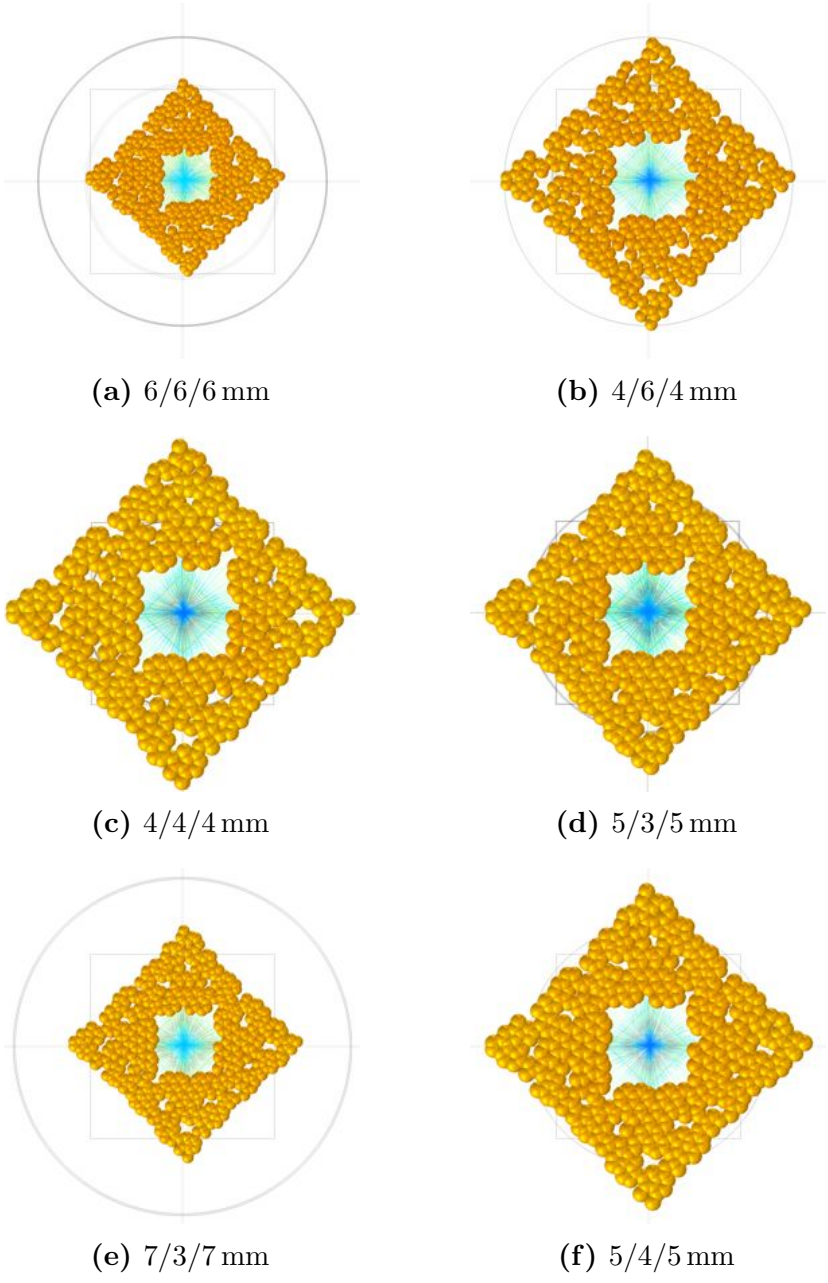

(a) 6/6/6 mm **(b)** 4/6/4 mm

(c) 4/4/4 mm **(d)** 5/3/5 mm

(e) 7/3/7 mm **(f)** 5/4/5 mm

Figure A.2.: These xy-trajectory plots present several images of the magnified inlet shape at the level of the detector if the diameters of the aperture pinholes are varied. The notation is $d_1/d_M/d_3$ referring to the first, middle and third aperture plate. The simulations are done with the diameter configuration in subfigure (f).

A.2.3. Different Lensing Potentials U

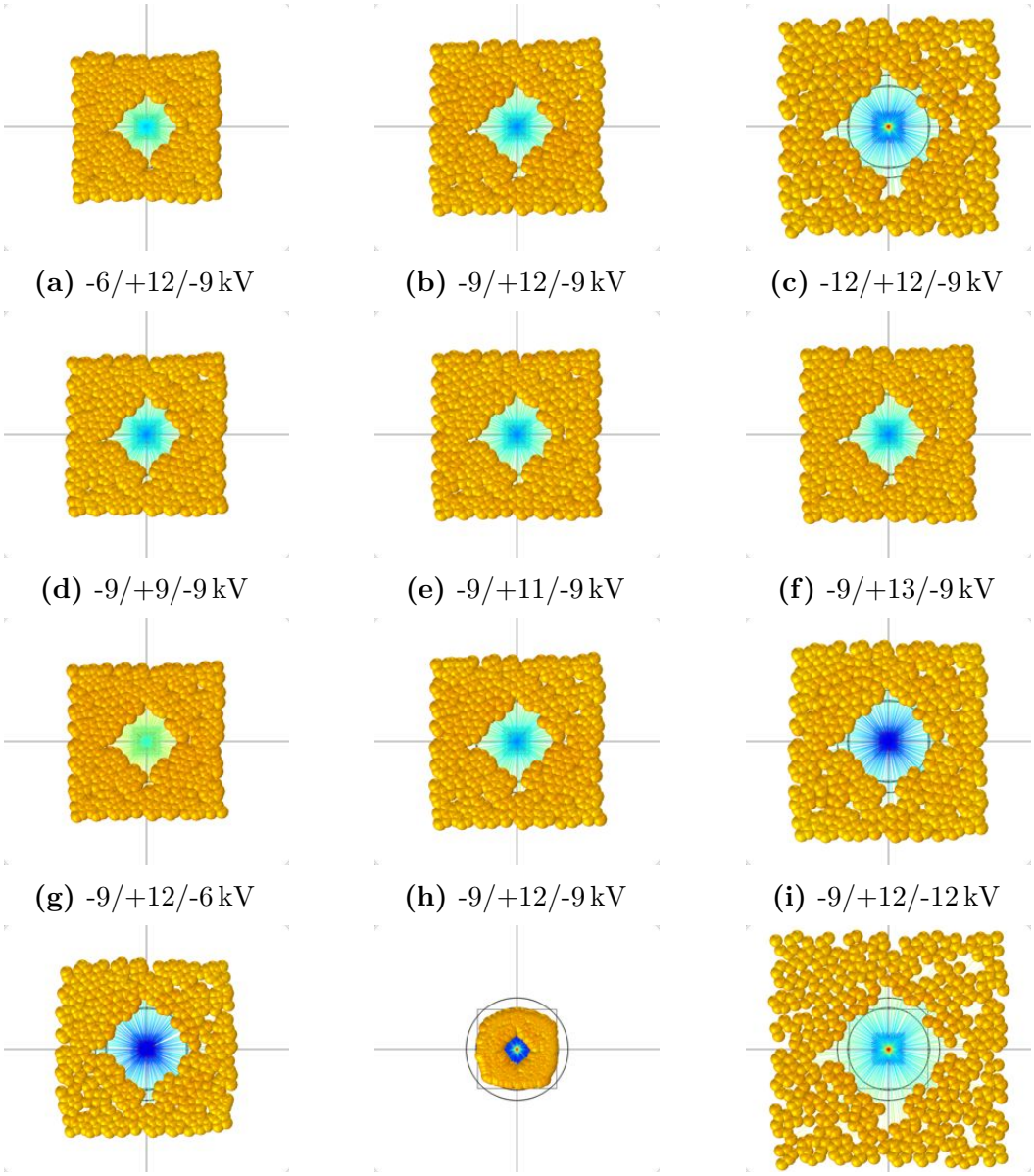

(a) -6/+12/-9 kV **(b)** -9/+12/-9 kV **(c)** -12/+12/-9 kV

(d) -9/+9/-9 kV **(e)** -9/+11/-9 kV **(f)** -9/+13/-9 kV

(g) -9/+12/-6 kV **(h)** -9/+12/-9 kV **(i)** -9/+12/-12 kV

(j) -10/+12/-12 kV **(k)** -12/+12/-12 kV **(l)** -12/+12/-8 kV

Figure A.3.: These xy-trajectory plots present several images of the magnified inlet shape at the level of the detector if the potentials of the aperture plates are varied. The particle velocity is about $12.1 - 12.2\,\mathrm{keV}$. The notation is $U_1/U_M/U_3$ referring to the first, middle and third aperture plate. The potential configurations in the simulations are based on the best result shown in subfigure (l).

B. List of Figures

C. List of Tables

D. List of Abbreviations

ASIC	Application-Specific Integrated Circuit
$\beta\beta$	double-beta-decay
$\beta\beta0\nu$	neutrinoless-double-beta-decay
CAD	Computer Aided Design
CF	ConFlat (vacuum standard)
C.L.	Confidence Level
cpt	charged particle tracing
CRT	Cathode Ray Tube
DAC	Digital-Analogue-Converter
es	electrostatic
fcc	face centred cubic
FEM	Finite Element Method
ISO-K	International Organization for Standardization - K (vacuum standard)
KF	Klein Flange (vacuum standard)
LN	Liquid Nitrogen
MIP	Minimal Ionising Particle
o.a.	optical axis
PTFE	Polytetrafluoroethylene
RGS	Rare Gas Solid
RHC	Right Handed Current
PMT	Photomultiplier Tube
RTD	Resistance Temperature Detector
sat.	saturation
SM	Standard Model
THL	Threshold Level
ToA	Time of Arrival
ToT	Time over Threshold
(V-A)	vector – axial vector (-theory)
WIMP	weak interaction massive particle

Bibliography

[1] E. Segrè. *From X-rays to Quarks - Modern Physicists and Their Discoveries*. W. H. Freeman & Company, New York, (1980).

[2] J. J. Gómez-Cadenas et. al. The search for neutrinoless double beta decay. *Riv. Nuovo Cim.*, **35**:29, (2012).

[3] N. Schmitz. *Neutrinophysik (german)*. Teubner, Stuttgart, (1997).

[4] H. V. Klapdor-Kleingrothaus, A. Dietz, H. L. Harney, I. V. Krivosheina. Evidence for neutrinoless double beta decay. *Modern Physics Letters A*, **16**:2409, (2001).

[5] C. E. Aalset et. al. Comment on "Evidence for Neutrinoless Double Beta Decay". *Modern Physics Letters A*, **17**:1475, (2002).

[6] A. Gando et. al. Limit on neutrinoless $\beta\beta$ decay of ^{136}Xe from the first phase of kamland-zen and comparison with the positive claim in ^{76}Ge. *Physical Review Letters*, **110**:062502, (2013).

[7] J. J. Gómez-Cadenas et. al. Sense and sensitivity of double beta decay experiments. *Journal of Cosmology and Astroparticle Physics*, **2011**(06):007, (2011).

[8] T. Michel et. al. The potential of hybrid pixel detectors in the search for the neutrinoless double-beta decay of ^{116}Cd. *Advances in High Energy Physics*, **2013**:105318, (2013).

[9] L. S. Miller, S. Howe, W. E. Spear. Charge transport in solid and liquid ar, kr, and xe. *Physical Review*, **166**:871, (1968).

[10] E. M. Gushchin, A. A. Kruglov, I. M. Obodovskii. Emission of "hot" electrons from liquid and solid argon and xenon. *Sov. Phys. JETP*, **55**:860, (1982).

[11] E. Gullikson, B. L. Henke. X-ray-induced secondary-electron emission from solid xenon. *Physical Review B - Condensed Matter*, **39**:1, (1989).

[12] R. A. Baragiola, M. Shi, R. A. Vidal, C. A. Dukes. Fast proton-induced electron emission from rare-gas solids and electrostatic charging effects. *Physical Review B*, **58**:13212, (1998).

[13] H. V. Klapdor-Kleingrothaus, K. Zuber. *Teilchenastrophysik (german)*. Teubner, Stuttgart, (1997).

[14] J ,B. Albert et. al. Search for majorana neutrinos with the first two years of exo-200 data. *Nature Article*, **510**:229, (2014).

[15] M. Filipenko et. al. Characterization of the energy resolution and the tracking capabilities of a hybrid pixel detector with cdte-sensor layer for a possible use in a neutrinoless double beta decay experiment. *European Physical Journal C*, **2013**:73:2374, (2013).

[16] L. Rossi. *Pixel Detectors*. Springer, Berlin, (2006).

[17] T. Takahashi, S. Konno, T. Doke. The average energies, w, required to form an ion pair in liquefied rare gases. *J. Phys. C: Solid State Phys.*, **7**:230, (1974).

[18] T. Takahashi et. al. Average energy expended per ion pair in liquid xenon. *Physical Review A*, **12**:1771, (1975).

[19] T. Doke et. al. Estimation of fano factors in liquid argon, krypton, xenon and xenon-doped liquid argon. *Nuclear Instruments and Methods*, **134**:353, (1976).

[20] E. Aprile et. al. *Noble Gas Detectors*. Wiley-VCH, Weinheim, (2006).

[21] W. E. Spear, P. G. le Comber. *Rare Gas Solids Vol. II*, chapter 18, page 1119. Academic Press, London, (1977).

[22] O. Hachenberg, W. Brauer. *Advances in Electronics and Electron Physics*, page 413. Academic Press, New York, (1959).

[23] M. L. Klein, T. R. Koehler. *Rare Gas Solids Vol. I*, chapter 6, page 301. Academic Press, London, (1976).

[24] E. M. Gushchin et. al. Electron emission from condensed noble gases. *Sov. Phys. JETP*, **49**:856, (1979).

[25] E. M. Gushchin, A. A. Kruglov, I. M. Obodovskii. Electron dynamics in condensed argon and xenon. *Sov. Phys. JETP*, **55**:650, (1982).

[26] S. H. Howe, P. G. le Comber, W. E. Spear. Hole transport in solid xenon. *Solid State Communications*, **9**:65, (1971).

[27] E. Aprile, K. L. Giboni, C. Rubbia. Drifting electrons over large distances in liquid argon-methane mixtures. *Nuclear Instruments and Methods in Physics Research A*, **253**:273, (1987).

[28] N. Schwentner, E.-E. Koch, J. Jortner. Electronic excitations in condensed rare gases. *Springer Tracks in Modern Physics*, **107**, (1985). Springer, Berlin.

[29] N. Schwentner et. al. Photoemission from rare-gas soldis: Electron energy distributions from the valence bands. *Physical Review Letters*, **34**:528, (1975).

[30] N. Rey Whetten, A. B. Laponsky. Energy distribution of secondary electrons from mgo single crystals. *Physical Review*, **107**:1521, (1957).

[31] Mykhaylo Filipenko. Experimental investigation of pixelated semiconductor photodetectors with cdte sensor material for the search for the neutrinoless double beta decay. Master's thesis, Friedrich-Alexander Universität Erlangen-Nürnberg, (2011).

[32] E. Brüche. Experimentelle elektronenoptik und ihre anwendung (german). *Zeitschrift für technische Physik*, **17**:588, (1936).

[33] V. K. Zworykin. On electron optics. *Journal of the Optical Society of America*, **215**:535, (1933).

[34] P. Dahl. *Introduction to Electron and Ion Optics*. Academic Press, New York, (1973).

[35] O. Scherzer. Die aufgaben der theoretischen elektronenoptik (german). *Zeitschrift für technische Physik*, **17**:593, (1936).

[36] A. Recknagel. Elektronenspiegel und elektronenlinse (german). *Zeitschrift für technische Physik*, **17**:643, (1936).

[37] H. Busch. *Beiträge zur Elektronenoptik (german)*. Verlag von Johann Ambrosius Barth, Leipzig, (1936).

[38] K.Diels. Die 8 bildfehler dritter ordnung magnetischer elektronenlinsen (german). *Zeitschrift für technische Physik*, **18**:65, (1937).

[39] K. Jousten. On the gas species dependence of pirani vacuum gauges. *Journal of Vacuum Science & Technology A*, **26**:352, (2008).

[40] airliquide.com. http://encyclopedia.airliquide.com/Encyclopedia.asp?GasID=40, Visited: 04.08.2014, Last Update: 2013.

[41] R. H. Beaumont, H. Chihara, J. A. Morrison. Thermodynamic properties of krypton. vibrational and other properties of solid argon and solid krypton. *Proc. Phys. Soc.*, **78**:1462, (1961).

[42] D. N. Batchelder. *Rare Gas Solids Vol. II*, chapter 14, page 883. Academic Press, London, (1977).

[43] W. Blum, W. Riegler, L. Rolandi. *Particle Detection with Drift Chambers*. Springer, Berlin, (2008).

[44] H. H. Chen, C. C. Lim, R. A. Aziz. The enthalpy of vaporization and internal energy of liquid argon, krypton, and xenon determined from vapor pressures. *J. Chem. Thermodynamics*, **7**:191, (1975).

[45] R. K. Crawford. *Rare Gas Solids Vol. II*, chapter 11, page 663. Academic Press, London, (1977).

[46] S. C. Fain Jr., M. D. Chinn, R. D. Diehl. Commensurate-incommensurate transition of solid krypton monolayers on graphite. *Physical Review B*, **21**:4170, (1980).

[47] D. Green. *The Physics of Particle Detectors*. Cambridge University Press, Cambridge, (2000).

[48] E. Gullikson. Hot electron diffusion lengths in the rare-gas solids. *Physical Review B*, **37**:7904, (1988).

[49] S.-C. Hwang, W. R. Weltmer. *Kirk-Othmer Encyclopedia of Chemical Technology*, page 1. Wiley, 4 edition, (1995).

[50] P. Korpiun, E. Lüscher. *Rare Gas Solids Vol. II*, chapter 12, page 729. Academic Press, London, (1977).

[51] I. N. Krupskii, V. G. Manzhely. Multiphonon interactions and the thermal conductivity of crystalline argon, krypton, and xenon (translated from russian). *Soviet Physics JETP*, **28**:1097, (1969).

[52] G. J. Schrobilgen. *Encyclopedia of Physical Science and Technology*, page 449. Academic Press, 3 edition, (2003).

[53] L. A. Schwalbe et. al. Thermodynamic consistency of vapor pressure and calorimetric data for argon, krypton, and xenon. *Journal of Chemical Physics*, **66**:4493, (1977).

[54] G. K. White, S. B. Woods. Thermal conductivity of the solidified inert gases: Argon, neon and kryptont. *Philosophical Magazine*, **3:32**:785, (1958).

[55] Y. Zhang, J. R. G. Evans, S. Yang. Corrected values for boiling points and enthalpies of vaporization of elements in handbooks. *J. Chem. Eng. Data*, **56**:328, (2011).

Acknowledgements

I would like to pass my thanks to the following persons, who helped me in many different ways in my life, in my academic carrier and throughout the process of this thesis:

- **Gisela Anton** for her excellent support, academic supervision and practical advice ever since my first experimental lecture and for giving me the possibility to join the lecturing team in *Particle Physics* and to contribute to the exciting research at her working group.
- **Mykhaylo Filipenko** for all his guidance and assistance in all aspects of this thesis as well as his coolness if faced epic experimental failures, his affinity to hop products and the amazing ants in his pants.
- **My parents** for their never-ending support and back-up especially in the last six years of my studies.
- **Meinen Großeltern** für ihren Optimismus und ihre immerwährende Unterstützung.
- **Thilo Michel** for him being a great supervisor lending his ear in every occasion, his intuitive problem solving manner and his all-time sunny attitude.
- **Thomas Gleixner** for his support in any matter including the worst segmentation errors and all problems concerning pixel detectors as well as his good sense of humour.
- **The Radiation and Detector Physics Group** for their support in many ways concerning multiple problems of different sizes and issues that occurred during my thesis.
- **Thorsten Kühn** for his technical and practical skills and assistance in every possible way – not least the re-unlocking of our desk drawers.
- **Jutta Dziwis** for all the patience with me messing up each and every business trip proposal.

- **Anastasia Bask**, **Maximilian Müller** and **Leif Stolberg** for the nice atmosphere in our office.
- **Patrick Hufschmidt**, **Ako Jamil** and **Tobias Ziegler** for suffering from all the loud music from our laboratory.
- **Uli Katz** for his versatility concerning examination regulations, his support in university-political matters and his famous open door.
- **Matthias Weißer** and **Timur Ishakov** for giving me the great possibility to gain a small insight in completely different interesting research fields.
- The guys from **testbeam 22 - DESY** for doing the same and giving us a great stay in Hamburg.
- **Mara Heinrichs** for literally everything.
- **Rike Berg**, **Robinson Perić** and **Jacqueline Catalano** for reading all the mess of 140 pages.
- All my **beloved friends** for a great time in Erlangen, all of the wonderful moments we spent and their patience during the last couple of months.
- All the funny people of the **student board** making my time at the university to the best and active time of my life.
- **Izzy** – my magnificent spider plant implanted at my first day at this working group for spending the last 72 weeks with me.

Statutory Declaration

I declare that I have developed and written the enclosed Master Thesis completely by myself, and have not used sources or means without declaration in the text. Any thoughts from others or literal quotations are clearly marked. The Master Thesis was not used in the same or in a similar version to achieve an academic grading or is being published elsewhere.

Erlangen, 22nd September 2014